PL-TR-94-2212

MODELING AND POST MISSION DATA ANALYSIS

V. A. Davis
M. J. Mandell

Maxwell Laboratories, Inc.
S-Cubed Division
P. O. Box 1620
La Jolla, California 92038-1620

8 June 1994

Scientific Report No. 1

Approved for public release; distribution unlimited

PHILLIPS LABORATORY
Directorate of Geophysics
AIR FORCE MATERIEL COMMAND
HANSCOM AIR FORCE BASE, MA 01731-3010

DTIC QUALITY INSPECTED 3

19950613 109

This technical report has been reviewed and is approved for publication.

DONALD A. GUIDICE
Contract Manager

DAVID A. HARDY
Branch Chief

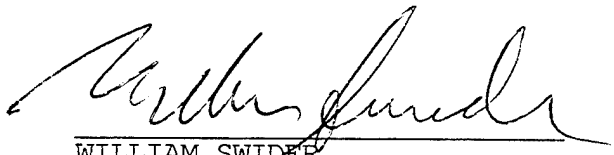

WILLIAM SWIDER
Deputy Division Director

This report has been reviewed by the ESC Public Affairs Office (PA) and is releasable to the National Technical Information Service (NTIS).

Qualified requestors may obtain additional copies from the Defense Technical Information Center (DTIC). All others should apply to the National Technical Information Service (NTIS).

If you address has changed, or if you wish to be removed from the mailing list, or if the addressee is no longer employed by your organization, please notify PL/TSI, 29 Randolph Road, Hanscom AFB, MA 01731-3010. This will assist us in maintaining a current mailing list.

Do not return copies of this report unless contractual obligations or notices on a specific document requires that it be returned.

REPORT DOCUMENTATION PAGE

Form Approved
OMB No. 0704-0188

Public reporting burden for this collection of information is estimated to average 1 hour per response, including the time for reviewing instructions, searching existing data sources, gathering and maintaining the data needed, and completing and reviewing the collection of information. Send comments regarding this burden estimate or any other aspect of this collection of information, including suggestions for reducing this burden, to Washington Headquarters Services, Directorate for Information Operations and Reports, 1215 Jefferson Davis Highway, Suite 1204, Arlington, VA 22202-4302, and to the Office of Management and Budget, Paperwork Reduction Project (0704-0188), Washington, DC 20503.

1. AGENCY USE ONLY (Leave blank)	2. REPORT DATE	3. REPORT TYPE AND DATES COVERED
	8 June 1994	Scientific No. 1

4. TITLE AND SUBTITLE
Modeling and Post Mission Data Analysis

5. FUNDING NUMBERS
PE 63410F
PR 2822 TA GC WU SC

Contract F19628-93-C-0050

6. AUTHOR(S)
V. A. Davis
M. J. Mandell

7. PERFORMING ORGANIZATION NAME(S) AND ADDRESS(ES)
Maxwell Laboratories
S-Cubed Division
P.O. Box 1620
La Jolla, CA 92038-1620

8. PERFORMING ORGANIZATION REPORT NUMBER

9. SPONSORING/MONITORING AGENCY NAME(S) AND ADDRESS(ES)
Phillips Laboratory
29 Randolph Road
Hanscom AFB, MA 01731-3010
Contract Manager: Donald Guidice/GPS

10. SPONSORING/MONITORING AGENCY REPORT NUMBER
PL-TR-94-2212

11. SUPPLEMENTARY NOTES

12a. DISTRIBUTION/AVAILABILITY STATEMENT
Approved for public release; distribution unlimited

12b. DISTRIBUTION CODE

13. ABSTRACT *(Maximum 200 words)*

This report described work performed during the first year of a contract to do analysis in support of three Phillips Laboratory flight experiments.
The PASP Plus effort is an examination of the interactions of the PASP Plus spacecraft and test solar cells with the low-energy plasma environment. This report describes calculations done to assist in determinations of the PASP Plus floating potential.
The SPREE effort is the use of comparisons with flight data to examine, improve, and validate sheath and electron collection models and to examine some of the interactions that determine the spectrum of the incident ions. This report describes research on ionization of shuttle thruster effluent by an electron beam.
The CHAWS effort is the development and validation of models of the spacecraft wake, including the currents to the various detectors of the CHAWS wake-side sensor on the Wake Shield Facility. This report describes two and three dimensional calculations of the wake environment and current collected by the CHAWS wake-side detectors for a range of flight conditions. A screen dipole model that reproduces some of the qualitative features of the three-dimensional calculations is also described.

14. SUBJECT TERMS	15. NUMBER OF PAGES
Photovoltaic Array Space Power Plus Diagnostics (PASP Plus), Shuttle Potential and Return Electron Experiment (SPREE), Charging Hazards and Wake Studies (CHAWS), solar array parasitic current collection, Tethered Satellite System (TSS-1), electrodynamic tethers, spacecraft charging, Wake Shield Facility (WSF), spacecraft wakes	114
	16. PRICE CODE

17. SECURITY CLASSIFICATION OF REPORT	18. SECURITY CLASSIFICATION OF THIS PAGE	19. SECURITY CLASSIFICATION OF ABSTRACT	20. LIMITATION OF ABSTRACT
Unclassified	Unclassified	Unclassified	SAR

TABLE OF CONTENTS

TABLE OF CONTENTS (cont.)

1. INTRODUCTION

This contract involves research in support of three Phillips Laboratory flight experiments, PASP Plus, SPREE, and CHAWS.

PASP PLUS

The objective of the PASP Plus analysis portion of this contract is to examine the interactions of the PASP Plus spacecraft and test solar cells with the low-energy plasma environment. Using calculational and experimental data, we are developing validated models of the parasitic current collection by the test arrays. Using calculations and experimental data, we will analyze the strengths and weaknesses of solar array arcing models.

The primary contributors to this portion of the contract were Dr. Victoria A. Davis and Ms. Barbara Gardner.

We gathered information on the PASP Plus arrays including a site visit to Orbital Sciences Corporation.

We identified the major physical interactions that will control the collection of parasitic current from the space plasma environment during the flight. The equilibrium potential of the insulating surfaces exposed to the plasma depends on geometric shielding from the plasma, barrier shielding from the plasma, and the orientation of the surface with respect to the ram. Barrier formation may play a role at the lower biases, particularly for module 3. Barrier formation occurs at higher biases under laboratory conditions than under space conditions. Snapover plays a major role in determining the current collected.

Using the Gilbert code, we are examining in detail the current collection properties of a single interconnect or solar-cell gap. We are developing a formula that gives the current collected as a function of the plasma and electrical parameters. The calculational technique has been automated. We are adjusting our computational algorithms to

include some additional effects that examination of the experimental results suggest are important.

We modified the solar array module of the EPSAT computer code for use by this project. The current to a solar array is now computed by adding together the current to all the interconnects, gaps, and edges of the solar cells. Information on the environment is used by the formula the computes the current to each interconnect, gap, or edge.

We examined the PASP Plus floating potential. In order to determine the floating potential, we need to characterize the electron collection of the biased test solar array, the electron collection of the power solar array, and the ion collection of the spacecraft body. The ion collection of the spacecraft body was characterized using the NASCAP/LEO computer code. Chapter 2 describes this work.

We are modeling the experiment panels of PASP Plus to look for any interference of sheaths and the range of plasma and electrical parameters at which interference might affect the experiment results.

We modified the EPSAT electron density model so that it can model the 1000 km to 2000 km regime that IRI-86 does not properly model. Chapter 3 describes this extension.

SPREE

The objective of the SPREE analysis portion of this contract is to use comparisons with flight data to examine, improve, and validate sheath and electron collection models and to examine some of the interactions that determine the spectrum of the incident ions.

The primary contributors to this portion of the contract were Dr. Gary A. Jongeward and Dr. Ira Katz.

We developed a module of EPSAT that examines effluent ionization for shuttle thrusters. We defined 860 lb thrusters and computed the ionization due to the interaction of the electron beam and the thruster effluent. We added a module that computes the density of ions created by effluent ionization as a function of position. We

developed a detector module that computes the flux of ions created by effluent ionization to the detector. Chapter 4 describes this work.

We revised and submitted a paper prepared under a previous contract. This paper has been published ("Observations of Ionosphere Heating in the TSS-1 Subsatellite Presheath", Journal of Geophysical Research, Vol. 99, No. A5, May 1994, p. 8961.)

CHAWS

The objective of the CHAWS analysis portion of this contract is to develop and validate models of the spacecraft wake, including the currents to the various detectors of the CHAWS wake side sensor on the Wake Shield Facility.

The primary contributors to this portion of the contract were Dr. Victoria A. Davis and Dr. Myron M. Mandell.

We used our two-dimensional computational tools to compute the current to a probe behind a disk in the geometry used in the Hanscom laboratory tank. Chapter 5 describes this work.

We used our two-dimensional computational tools to estimate the relative importance of the thermal and electrostatic effects for the flight experiment. Chapter 6 describes this work.

We used DynaPAC to compute the current collected by the CHAWS wake side detectors for a range of flight conditions. We developed a scheme for interpolating to additional conditions. We examined the effect on current collection of the high voltage screen and grounded current collection plate design. Chapter 7 describes this work.

We developed a screen dipole model that reproduces some of the qualitative features of the three-dimensional calculations. Chapter 8 describes this model.

We developed two new modules for the EPSAT computer code. The Wake Studies module explores the density and current to a detector in the ambient plasma or behind a disk in the neutral approximation. Chapter 9 describes this module.

The new CHAWS Current Module gives the current to the wake side probe as computed by the DynaPAC and POLAR computer codes. Chapter 10 describes this module.

The geomagnetic coordinates were added to the Magnetic Field at a Point screen of EPSAT. Chapter 11 describes the implementation.

The EPSAT floating potential model was modified to include the effect of the variation in the v x B potential across an object. Chapter 12 describes this implementation. Two new subscreens to the floating potential screen were added. One shows the minimum and maximum potentials at the corners of each object. The other allows the user to display the "surface" potential on the entire system.

We used the measurements of the secondary emission yield of stainless steel made at Hanscom as a basis for a formula for the secondary emission as a function of incident particle energy and species. Chapter 13 describes this work.

2. ION COLLECTION BY THE APEX SPACECRAFT

We would like to know the floating potential of the APEX spacecraft when the electron gun is not operating in order to determine under what circumstances the electron gun is needed. The floating potential is the potential at which the net current to an object is zero. One significant current to the APEX spacecraft is the ion current to the spacecraft. Calculations to characterize the ion current are described here.

We used the three-dimensional NASCAP/LEO computer code to examine the ion collection of the APEX spacecraft. We used the PATRAN model shown in Figure 1, which was supplied by R. Chock of NASA/LeRC. The body is the primary ion current collection surface. The backs of the solar arrays, the backs of the experiment panels, and the fronts of the experiment panels are all defined to be insulating materials with negative surface potentials a few times the electron temperature. The power solar arrays are defined to be material SOLA, which is a partially conductive material specifically designed to model solar arrays. A section of the experiment panel is defined as a conductor, which will be set at a positive potential in order to determine if the potential of the test arrays will have any effect on the ion current collected at a specific ground potential.

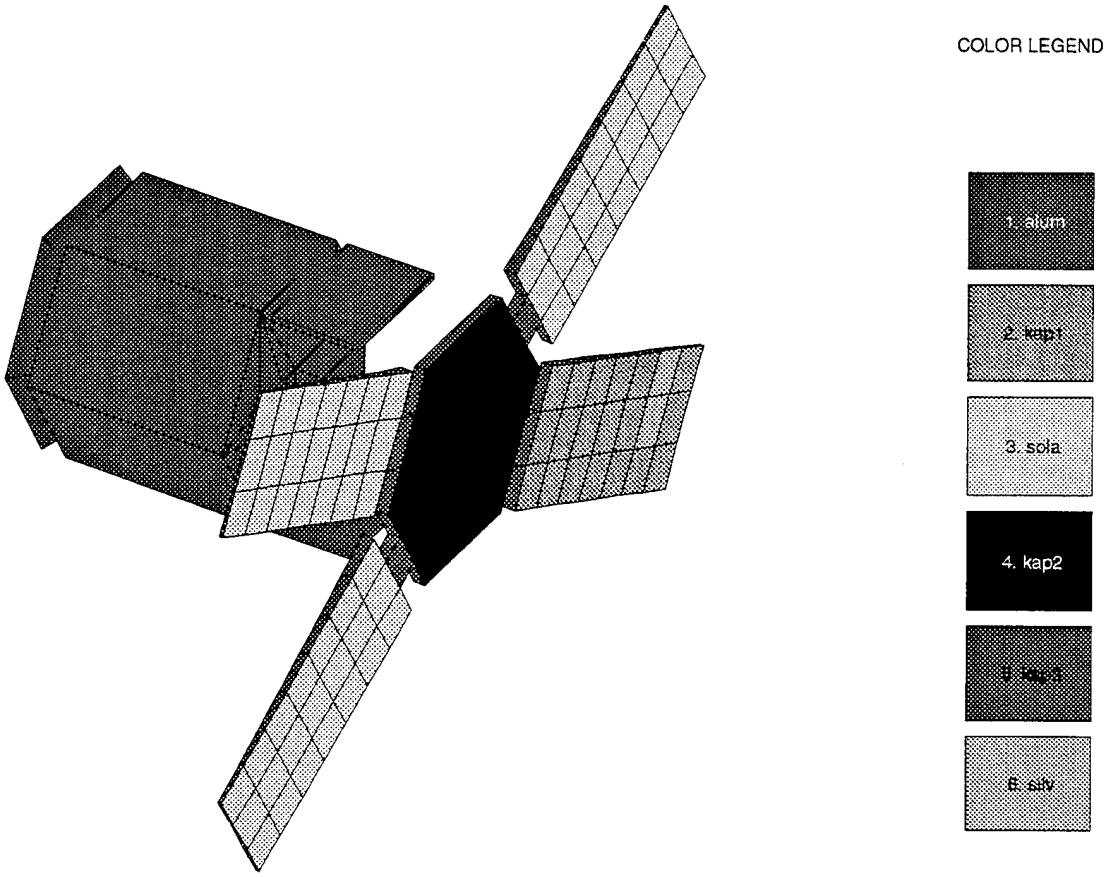

Figure 1. PATRAN model of the APEX Spacecraft

A series of calculations were done with different plasma conditions and potentials. Contours from a typical calculation are shown in Figure 2. In this calculation the plasma is atomic oxygen with a density of 10^{11} m^{-3} and a temperature of 0.1 eV. The spacecraft is moving at 7800 m/s in the +X direction. The spacecraft ground is at –40 V; the power arrays are at +32 V with respect to spacecraft ground; and the test array is at +50 V with respect to spacecraft ground. The sheath potential is –3.9 V. From Figure 2a it can be seen that even though the body is in the wake of the solar arrays, much of the sheath is exposed to the ram and collects current. From the series of calculations, this appears to be true in general.

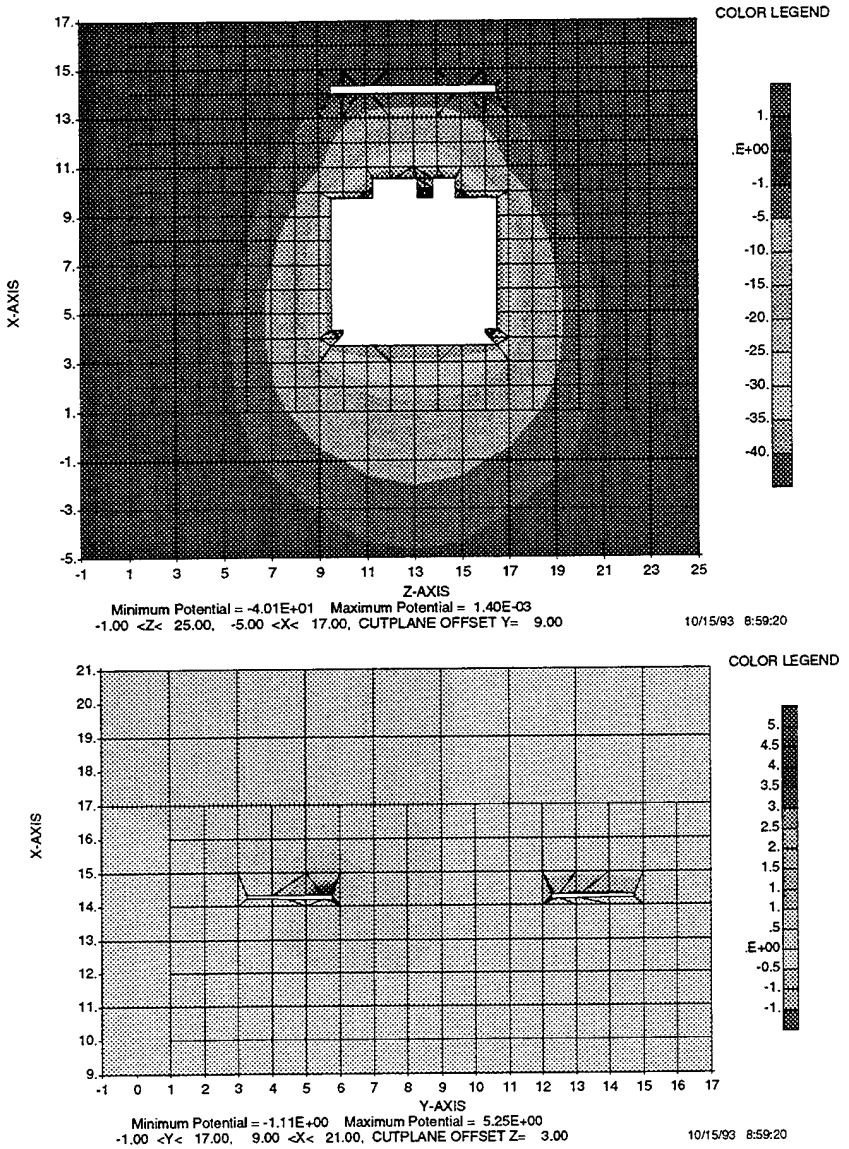

Figure 2. Potential contours about the APEX spacecraft. (a) shows the potentials in a plane through the center of the spacecraft. The outline of the body is in white. (b) shows the potentials in a plane perpendicular to the plane of (a) that passes through the experiment panel and a solar array. The object is white.

Figure 3 shows the current collected for all the calculations. The current is scaled by the ion thermal current for the convenience of plotting only. The primary variable that controls the current collected is the plasma density, through its effect on the sheath size and the current available.

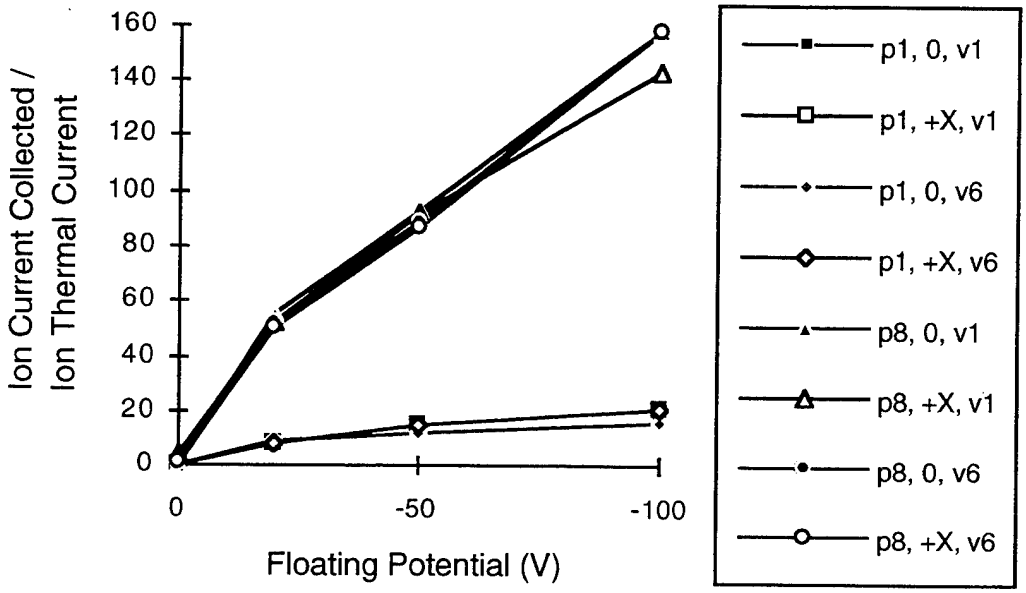

Figure 3. Current collected for the calculations done. The scaling by ion thermal current is for plotting convenience. The plasma for the p1 cases is 10^{12} m^{-2}, 0.05 eV, O^+, 1.4 x 10^{-4} A m^{-2}. The plasma for the p8 cases is 10^9 m^{-2}, 0.2 eV, H^+, 7.0 x 10^{-8} A m^{-2}. For the 0 cases, the spacecraft is not moving. For the +X cases, the spacecraft velocity is 7800 m/s in the +X direction. In the v1 cases, both the power array and test array are at 0 V. For the v6 cases, The power array is at +32 V and the test array is at +400 V with respect to spacecraft ground.

At the higher density, the current is enhanced by up to 30 percent due to ram effects. More current enters the sheath because the ions are moving faster than the thermal velocity. However, particles that enter the sheath of a moving spacecraft may miss the spacecraft and not contribute current. At the lower density, these two effects cancel each other and the current is independent of the velocity (for the velocities examined).

The current collected is independent of the potential on the power array and the test array. Therefore they can be ignored in estimates of the current collected by the body.

We have characterized ion current collection by the APEX spacecraft. The next step is to create an EPSAT model of the APEX spacecraft that has the same current collection properties. Within EPSAT the ion collection of APEX can be combined with the electron collection of the power arrays and the electron collection of the test arrays to determine the floating potential. Preliminary estimates indicate that the floating potential will remain below 100 V even without the electron emitter.

3. MODIFICATION TO EPSAT PLASMA DENSITY MODEL

In the altitude range from 1000 to 2000 km, EPSAT can use either of two methods to compute the plasma density. The IRI86 model can be used even though there are questions regarding its applicability. If IRI86/Al'pert is chosen, an alternative model for the density is used in this range.

The alternative model is from Ya. L. Al'pert, *The near-Earth and interplanetary plasma, Vol 1., General properties and fundamental theory*, Cambridge University Press, Cambridge, Great Britian, 1983 page 22.

$$N(z) = N_o \frac{z_o}{z} \exp\left\{ \frac{g_o M_o z_o}{2kT_o} \left[\frac{1}{1+(R_o/z)} - \frac{1}{1+(R_o/z_o)} + \ln \frac{1+(R_o/z)}{1+(R_o/z_o)} \right] \right\}$$

where R_o is the earth's mean radius, z_o is 1000 km, N_o is the density at 1000 km, M_o is the ion mass, g_o is the acceleration of gravity, T_o is the temperature in Kelvin, and k is Boltzmann's constant.

At altitudes above 1000 km, the above formula is used for the plasma density with the following input values.

R_o 6371 km

z_o 1000 km

N_o IRI86 plasma density at specified conditions at 1000 km

M_o $(0.9 * 1 + 0.1 * 4)\ 1.67 \times 10^{-27}\ \text{kg} = 2.17 \times 10^{-27}\ \text{kg}$

g_o $9.807 \times 10^{-3}\ \text{km/sec}^2 * \left(\frac{R_o}{R_o + z}\right)^2$

kT_o 1.16×10^4 * IRI86 electron temperature in eV at specified conditions at specified location

The IRI86 values for the temperatures and the relative ion densities are used for all altitudes.

4. BEAM IONIZATION AND DETECTOR MODULES IN EPSAT

Beam Ionization and Detector Modules in EPSAT

The following discussion amplifies the viewgraphs that follow.

Viewgraph 1:

We defined a shuttle model for EPSAT for studies of electron beam escape and impingement, ionization, and contamination. To simulate the beam ionization of thruster effluents and flash evaporator operations, five nozzles were defined using the EPSAT model. Three nozzles represent the 860 lb bi-propellant thruster and two represent the flash evaporator.

Viewgraph 2:

The flash evaporators are located on the underside of the shuttle and directed to each side to attain zero thrust to the shuttle. Presently, we do not know the precise flow rates and mach characteristics. We are working to obtain these from Rocketdyne.

Viewgraph 3:

We placed three thrusters in positions determined from early shuttle diagrams. These positions need verifying. The nozzle characteristics were chosen to match the bi-propellant nozzle simulations of Y. C. Doo and D. A. Nelson, "Direct Monte Carlo Simulation of Small Bipropellant Engine Plumes" AD-A177 079 (1987). The EPSAT nozzle was scaled up from the one described in this paper.

Viewgraph 4:

We defined a 1 keV, 100 mA beam to model the FPEG. The figures show two different orientations with respect to the magnetic field. In one case the beam intersects the orbitor and in the other it escapes. The ionization rate is shown as

the color of the beam line. The magnetic field, orbit, and electron beam models in EPSAT will be used for precise electron beam propagation calculations, which can be compared with data points.

Viewgraph 5:

The neutral densities as a function of position can be computed using existing capabilities.

Viewgraph 6:

We added a model of the ionization of the effluent cloud by the beam. Presently the ionization rate uses the energy dependent cross section of nitrogen. Other cross sections can be easily substituted.

We added a model of the expansion of the ionized neutrals. For this preliminary work, the model assumes that the ions expand in the radial barometric potential. Other models of the expansion can be easily substituted.

We created a detector module that uses the ion expansion model's results to compute the flux to a detector. The user specifies the acceptance angle, the direction of the detector, the position of the detector, and the energys. The module outputs the density and differential flux of each of the species.

Viewgraph 7:

In the plots of the beam, the color indicates the ionization rate.

The density computed by the expansion model can be displayed.

After some confirmation and perhaps upgrading of the ionization and expansion models, these new capabilities can be used to study the effect of the beam ionization on SPREE measurements.

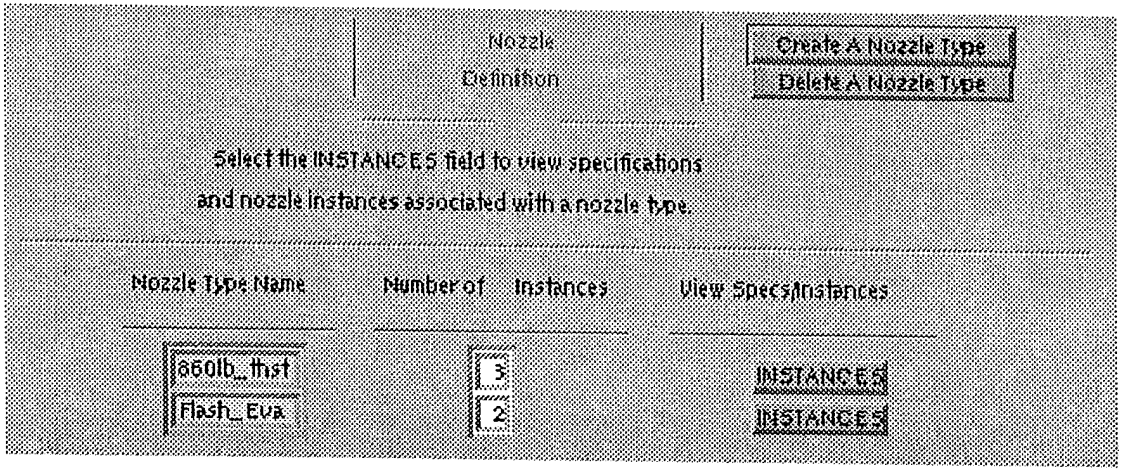
Nozzle
Definition
Create A Nozzle Type
Delete A Nozzle Type
Select the INSTANCES field to view specifications
and nozzle instances associated with a nozzle type.
Nozzle Type Name
Number of Instances
View Specs/Instances
860lb_thst
Flash_Eva
3
2
INSTANCES
INSTANCES

Flash Evaporator Definition

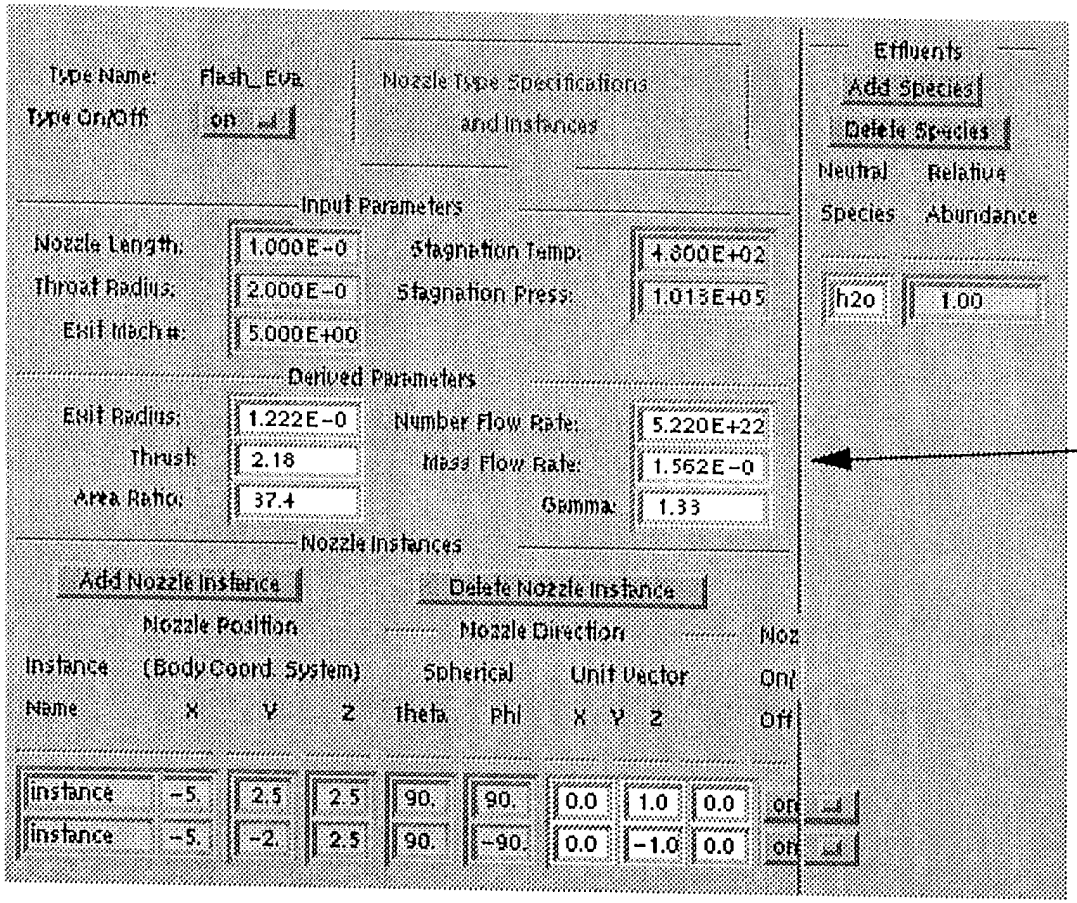

Thruster Definition
Three ~860 lb Bi-Propellant Engines

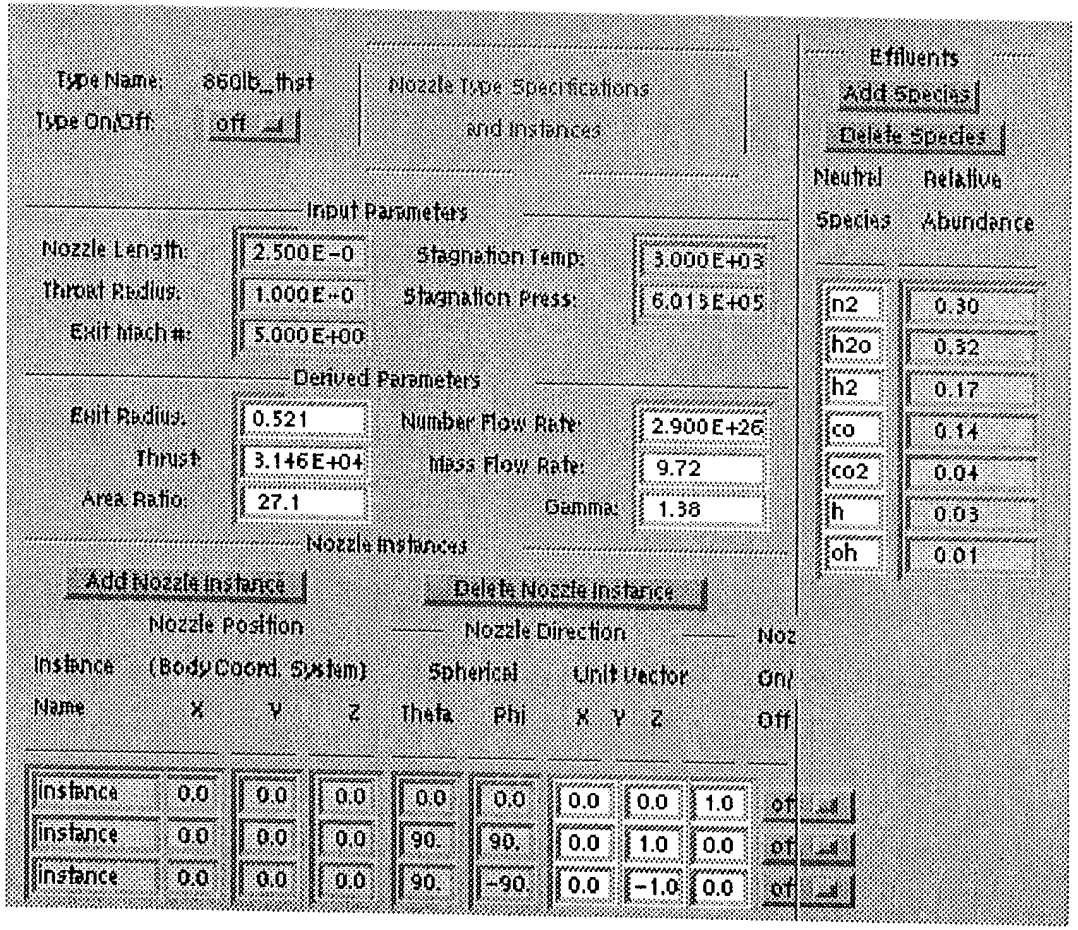

FPEG SImulation
1KeV, 100mA Beam

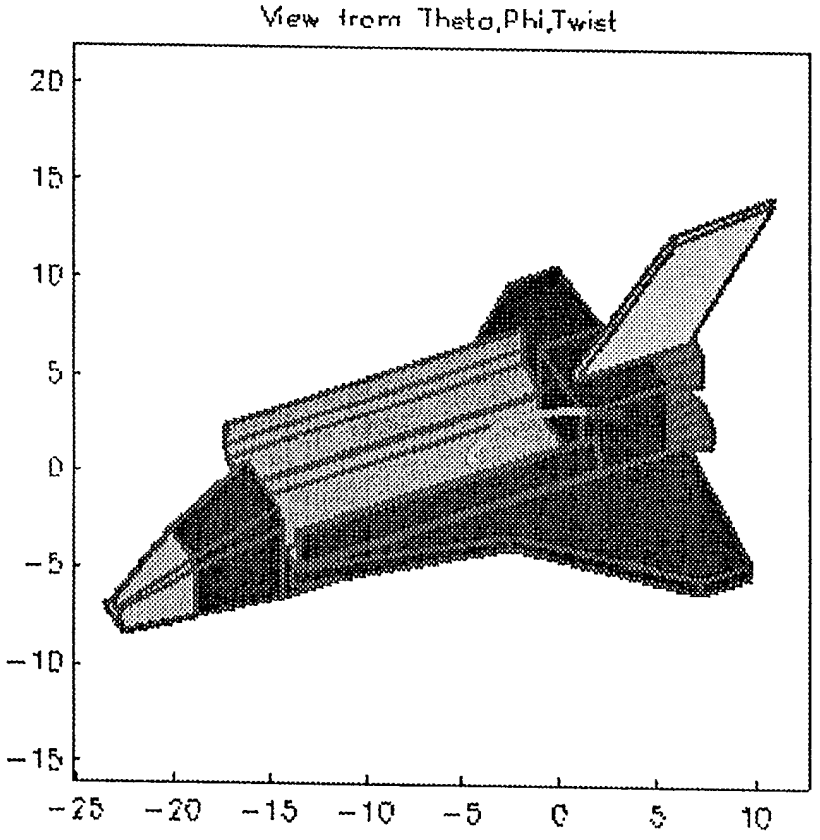

Beam Intersects Orbiter

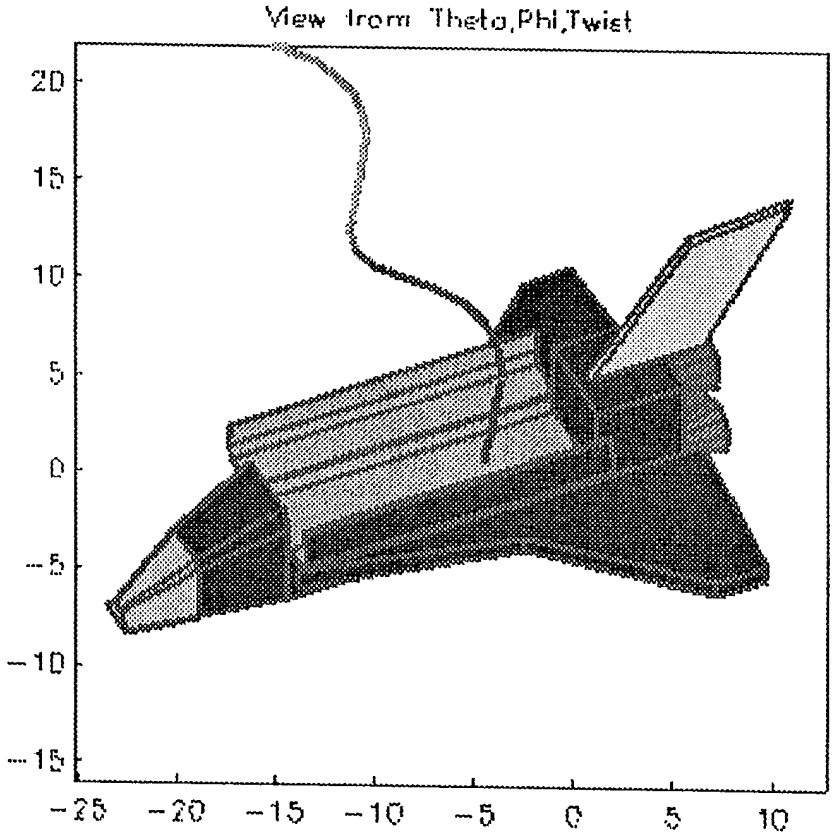

Beam Escapes Orbiter

Effluent Cloud From Three 860 lb Thrusters

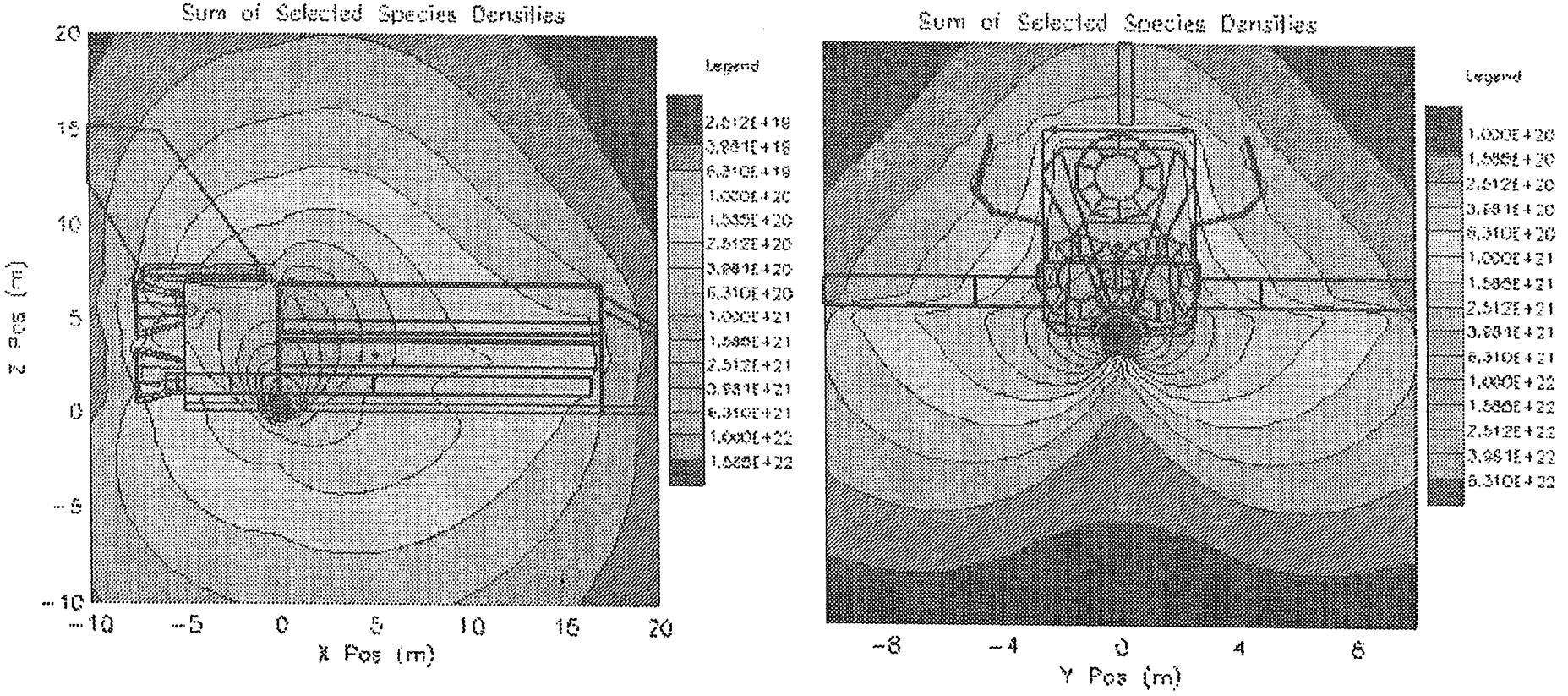

Water contribution only, Shadowing Neglected

Flux Of Ionized Neutrals To A Detector

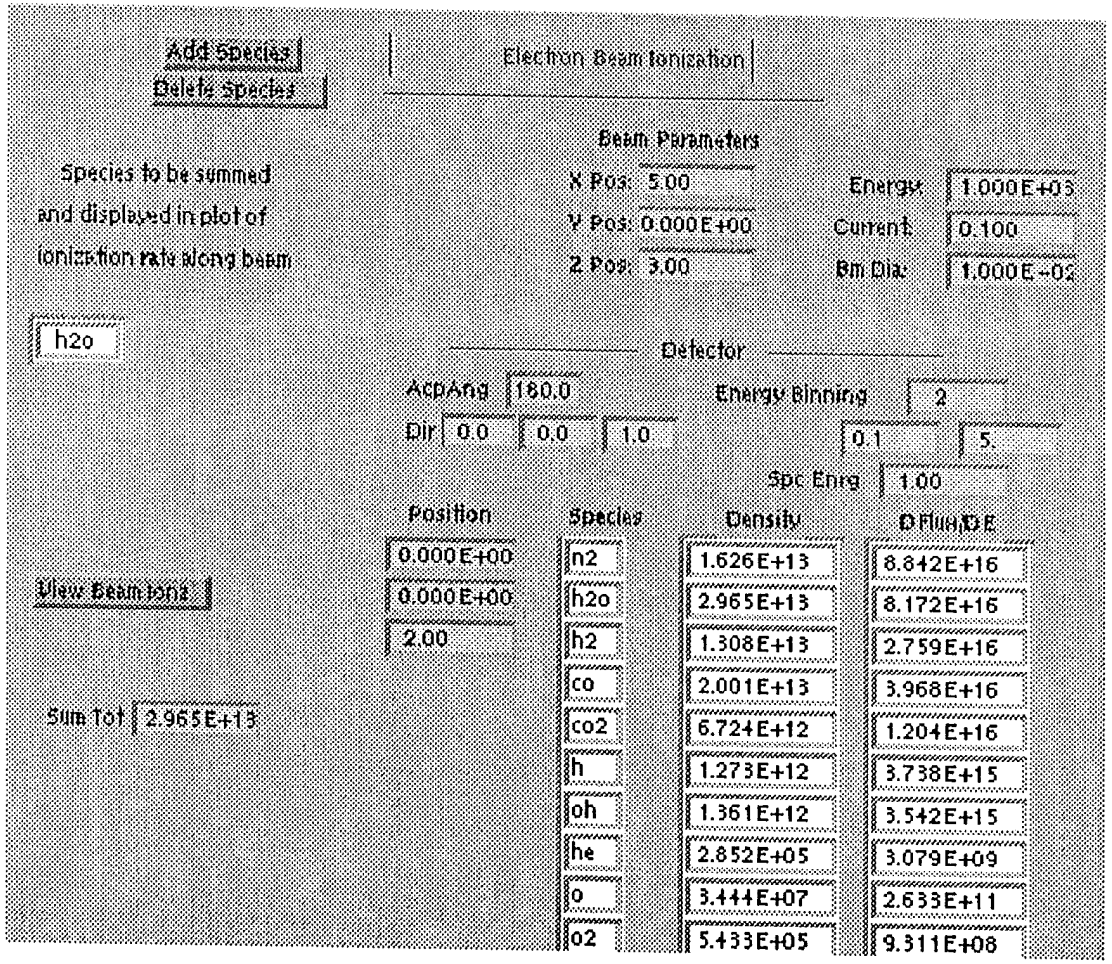

- Model assumes ionized neutrals expand in radial barometric potential
- Ionization rates use energy dependent cross-section (currently for nitrogen)
- All results preliminary!

Ionization Of Water Neutrals Along Electron Beam

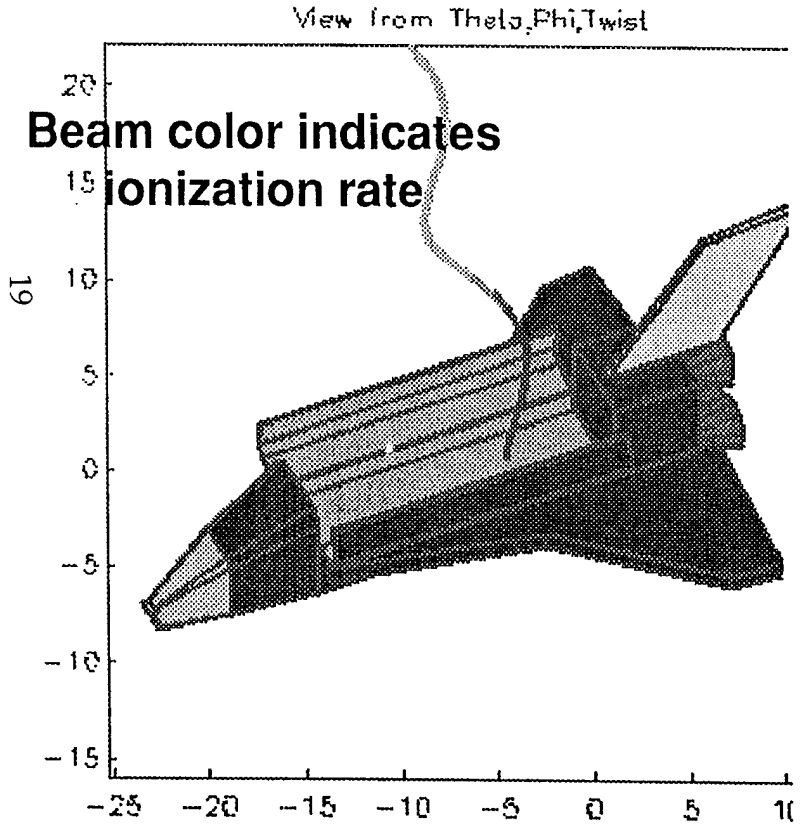

Three 860 lb thrusters firing

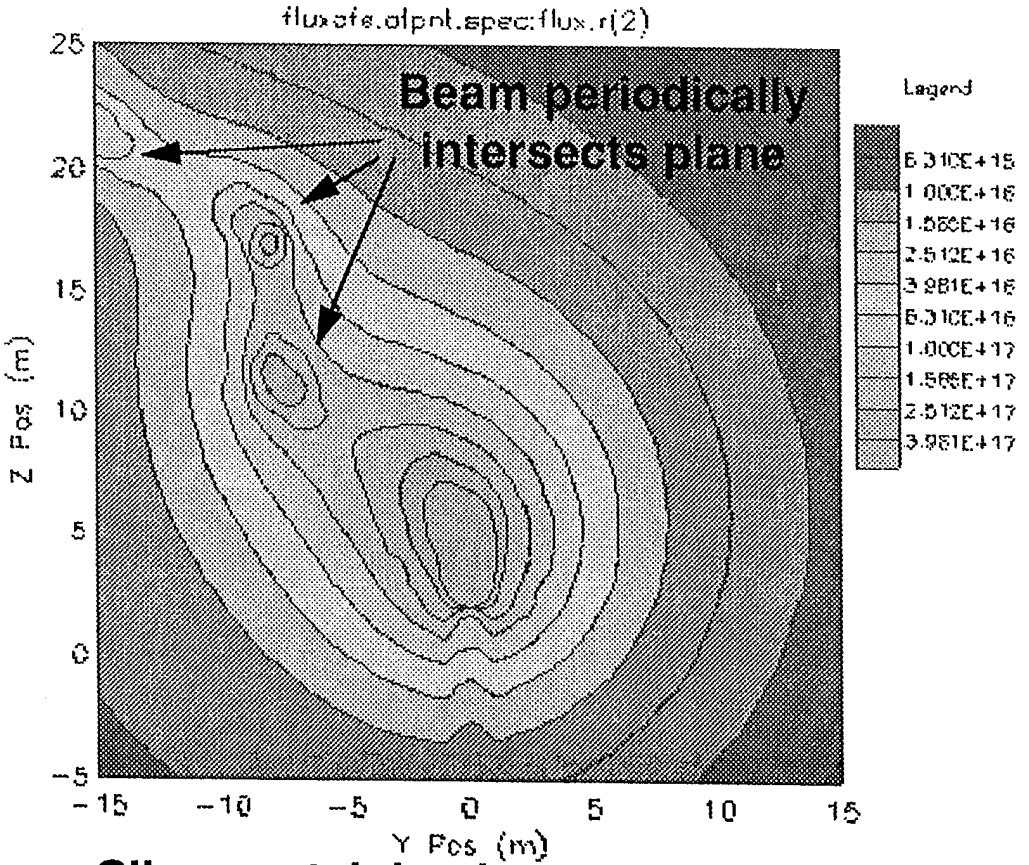

Slice containing beam & magnetic field

5. MODELING OF THE CHAWS LABORATORY EXPERIMENT

We did some calculations to model the CHAWS lab experiment. The motivation for the calculations was to establish how well we are able to model the experiment and make any modeling improvements necessary. With the partial validation by comparison with the laboratory experiments, we will have more confidence in our modeling of the flight experiment. The conditions in the laboratory are different from those in space.

We found it difficult to obtain converged answers. The collected current is sensitive to small changes in the potentials.

We computed the collected current for a sphere with radius 0.75 cm at 1 cm, 3 cm, 5 cm, 7 cm, and 9 cm behind the center of a 7.5 cm radius disk. Primarily we assumed that the ions were incident normal to the disk. We did a few calculations in which the divergence of the incident beam was included. The current collected in these calculations was way below that measured.

Poisson's equation was solved with the ion density determined from tracking ions and an electron density of $n_e(\phi) = n_o e^{\phi/\theta}$ for negative potentials. The n_o value was 3.3×10^{13} m^{-3} and the θ value was 2.5 eV. The disk was at 2.5 V. Two energies of Argon ions were introduced at the grid boundary. The dominate component had a current density of 0.0994 Am^{-2} and an energy of 90 eV associated with the forward motion. The other component had a current density of 0.0044 Am^{-2} and an energy of 18 eV associated with the forward motion. The inclusion of the low-energy component seen in the laboratory helped stabilize the numeric fluctuations. The grid used for the 5 cm case is shown in Figure 4.

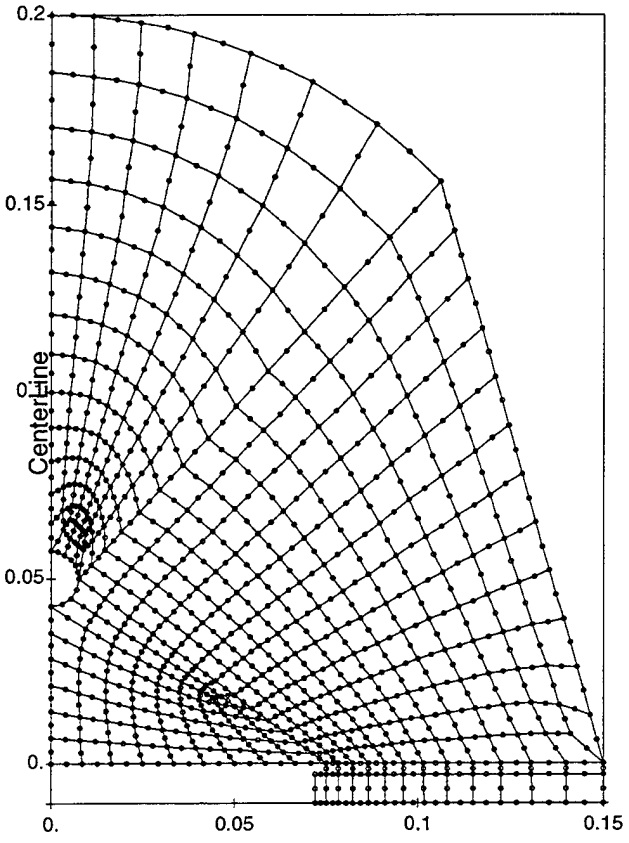

Figure 4. Computational Grid for the 5 cm case.

Potentials contours and a typical set of trajectories for the 5 cm case with the sphere at 6000 V is shown in Figure 5. The corresponding charge densities are shown in Figure 6. The charge density is noisy, however several features can be seen. The white area is where the charge density is off the scale. Since the tracked macroparticles have no angular momentum, an unphysical amount of charge focuses on the axis. The sharpest real feature is the density gradient along the trajectory of the first high energy ion. There is also a density gradient at the edge of the wake. The large area of lower charge density at the top of the grid appears to be real and is in all the calculations. Smooth potentials are obtained because the potential is dependent on the charge density over an area, so local fluctuations are integrated out.

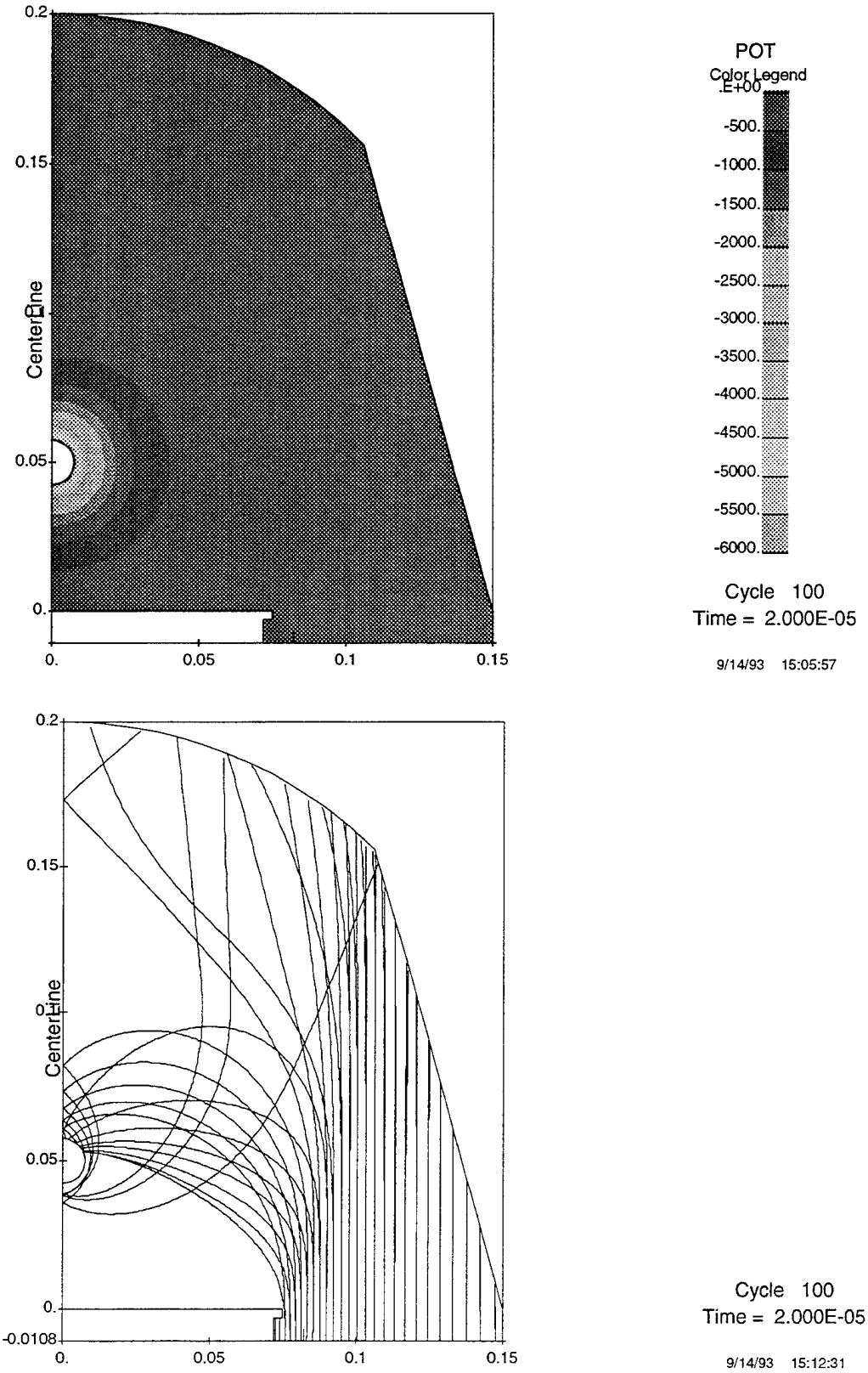

Figure 5. Potential contours and a few ion trajectories for the 5 cm, 6000 V case.

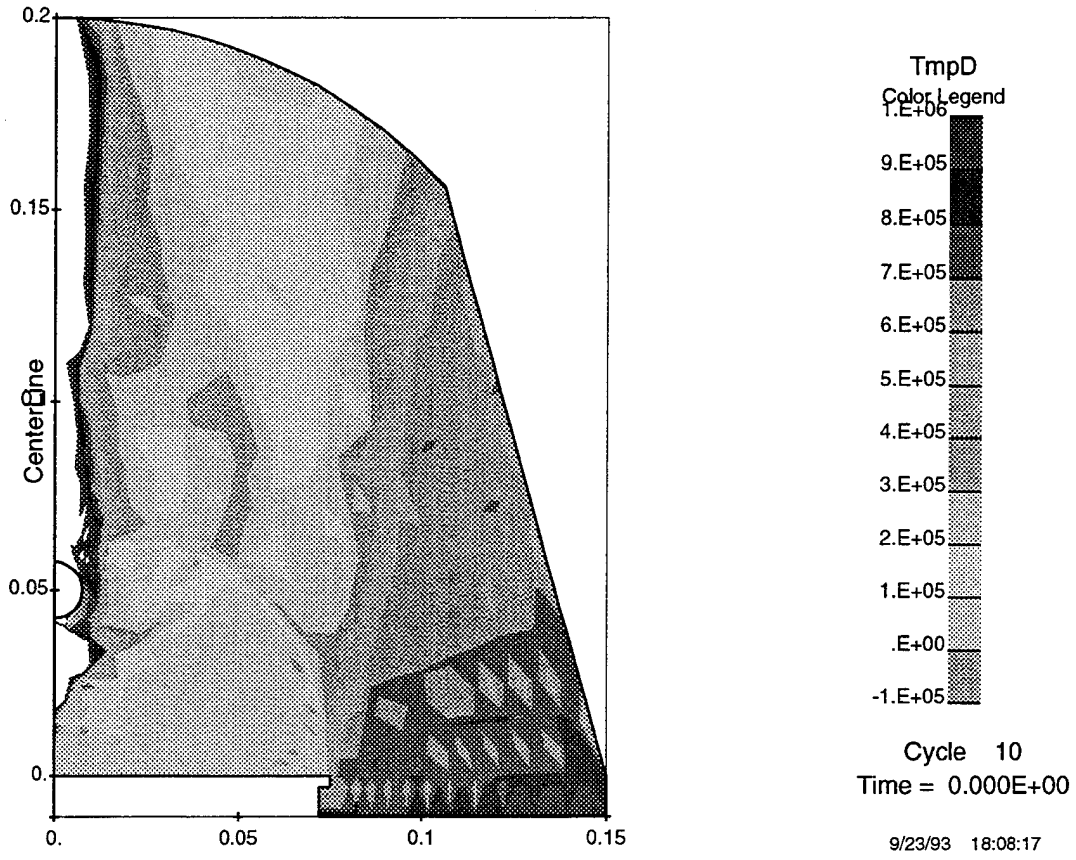

Figure 6. Charge density of ions consistent with the potentials shown in Figure 2.

One of the complications of the calculations is that the potential is screened by the tracked ions. Ions that just miss the sphere circle the sphere, contributing charge density and screening out the potential. Slight errors in the solution are amplified. It is difficult to reach a convergent answer. A range of initial directions or energies stabilizes the problem.

The computations were done in two different fashions, traditional PIC (particle-in-cell) and full trajectory. For this two dimensional problem, neither approach was superior. In the PIC calculations, at each time step, a set of ions were emitted at the boundary, all of the ions tracked, and the potential was recomputed. In the full trajectory calculations, the ions were tracked until they were collected or left the grid between potential solutions. At each cycle of the full trajectory calculations, the newly computed potentials and densities are blended with the previous values. The best blend ratios appeared to be 50% of the old potential and 95% of the old densities.

The collection current as a function of applied potential for the five locations is shown in Figure 7 for the two solution methods.

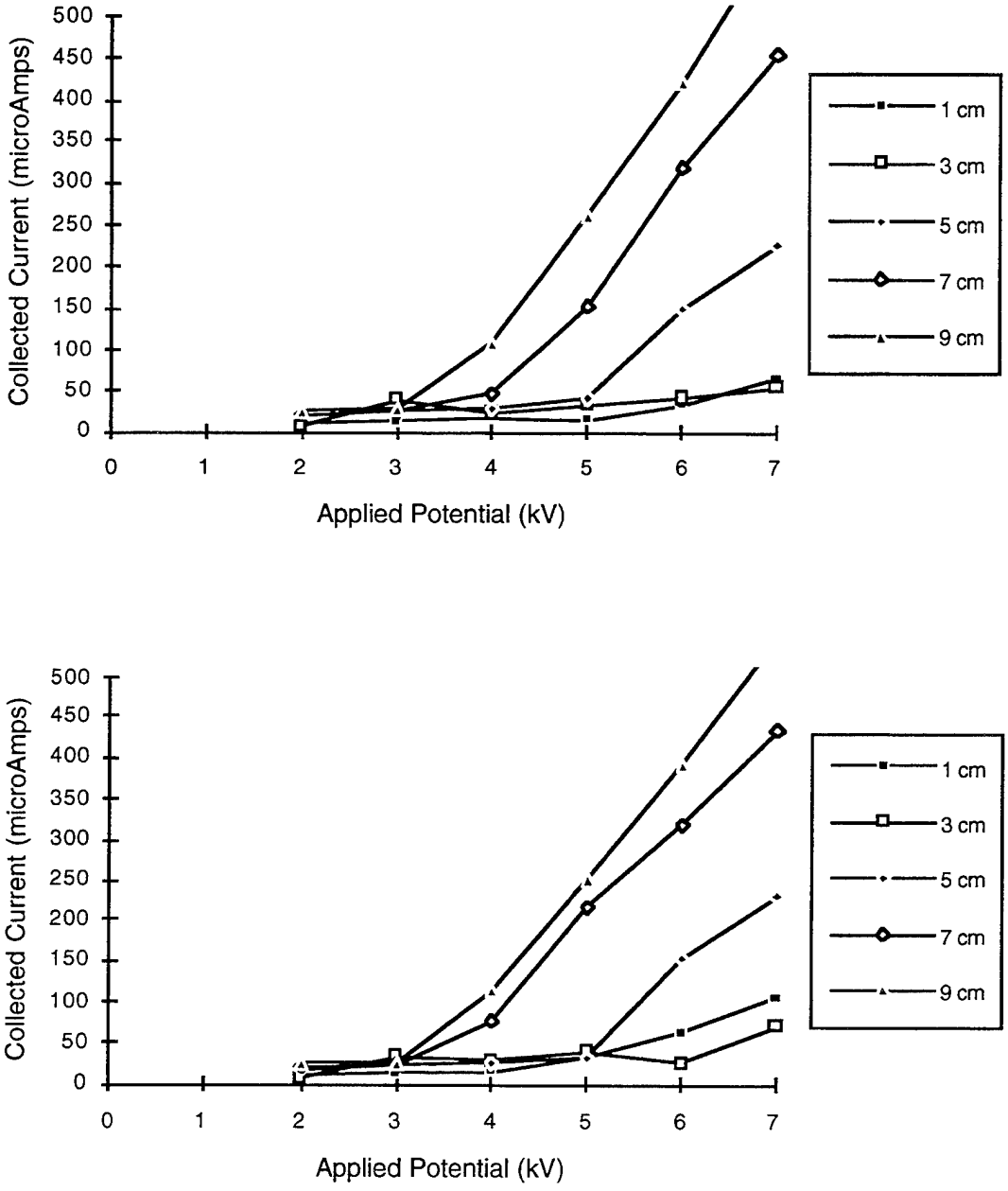

Figure 7. The I-V curves for the different sphere locations, for the (a) PIC and (b) full trajectory methods of solution.

Calculations were also done in which the ions were taken to have a thermal spread of 0.05 eV. The results were the same and even though more particles were followed, the solution did not converge better.

We also did a set of calculations in which the ion temperature was taken to be the same as the electron temperature, 2.5 eV. While these calculations do not represent the laboratory experiment, they are more like what will be seen in space. These calculations rapidly, smoothly converged to a stable solution with only 50% sharing of charge densities and no sharing of potentials. Figure 8 shows trajectories of macroparticles in the converged potentials for the 5 cm, 6000 V case. The particles are spread out, but the potential does not change much. Trajectories for particles in the center of the distribution are much as the same as those for the zero temperature ion case. The current for this case is greater than the zero temperature case by under 10%.

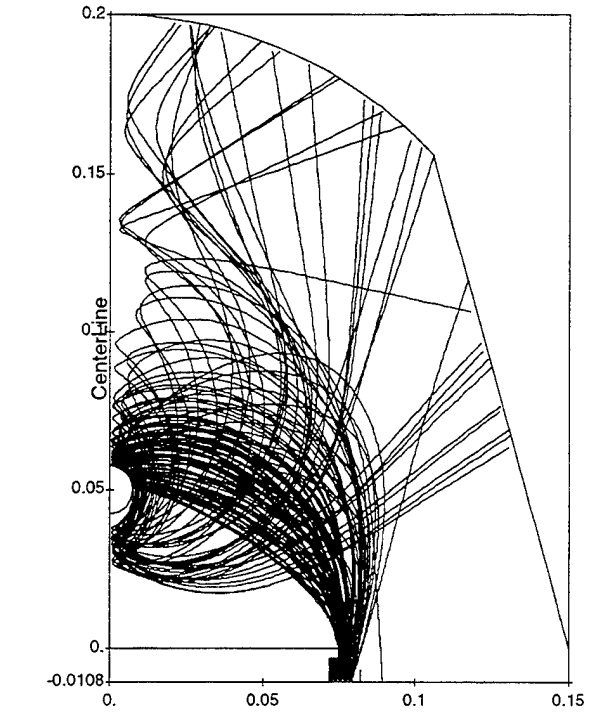

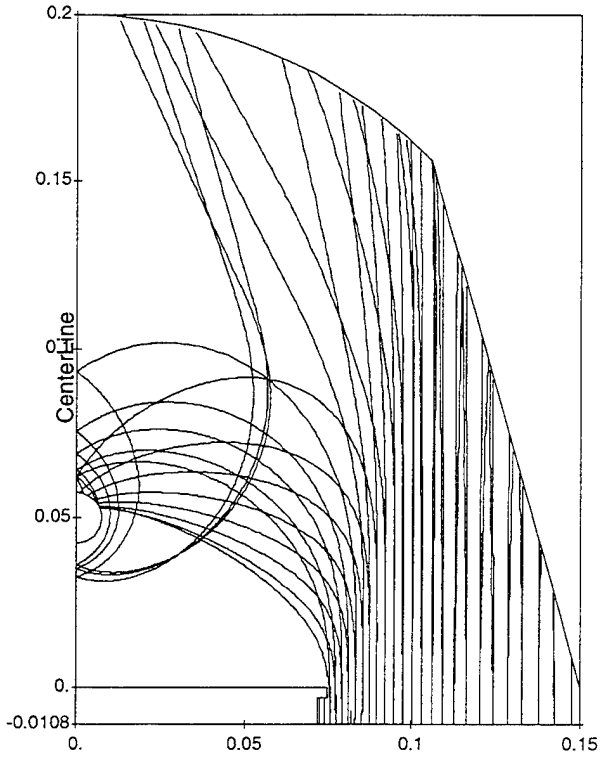

Figure 8. A few ion trajectories for the 5 cm, 6000 V case where the ions are at 2.5 eV. (a) shows a thermal distribution of particles starting from a few locations near the disk. (b) shows a set of particles with the same initial conditions as those shown in figure 2.

Finally, we are interested in the effect of a potential on the disk. We did a few calculations for a biased disk. Figure 9 shows trajectories of macroparticles in the converged potentials for the 5 cm, 6000 V case for an ion temperature of 2.5 eV and a disk potential of –20 V. The trajectories are pulled toward the disk. The current for this case is 30% more than the case shown in Figure 8.

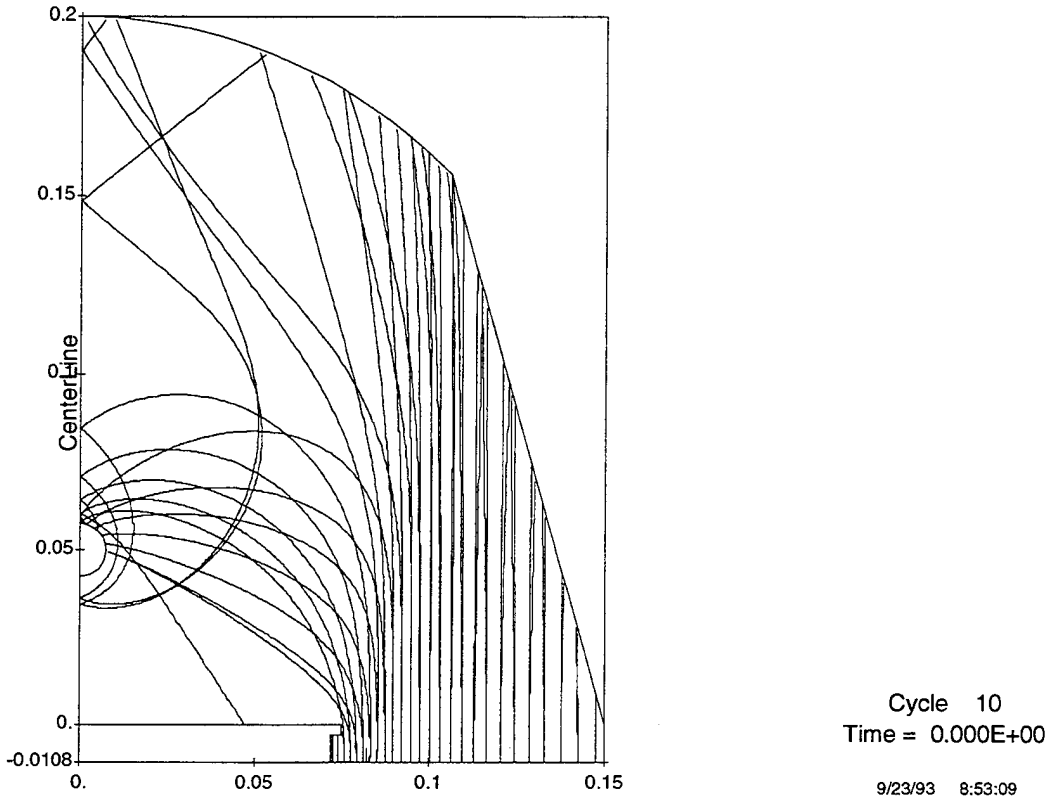

Figure 9. A few ion trajectories for the 5 cm, 6000 V case where the ions are at 2.5 eV and the disk is based –20 V. The macroparticles have the same initial conditions as those shown in Figure 2.

6. MODELING OF THERMAL AND ELECTROSTATIC EFFECTS ON WAKE FILLING IN A CYLINDRICALLY SYMMETRIC SYSTEM

We did a set of calculations as a preliminary exploration of the relative importance of the electrostatic filling and thermal filling of the wake region.

The grid is as shown in Figure 10a. The disk edge portion is expanded in 10b. The disk has the same radius as WSF.

Figure 11 shows the ion density for a 1×10^{12} m^{-3}, 0.1 eV oxygen plasma with a ram energy of 5.11 eV. This density was computed from the analytic formula.

Figure 12a shows the potentials that result from a charge density that is the sum of the ion density shown in Figure 11 and a barometric electron density, $n_o e^{-\phi/\theta}$ where $n_o = 10^{12}$ m^{-2} and $\theta = 0.1$ V. The sphere behind the disk has a fixed potential of 1V. Figure 12b shows some typical electron trajectories in these potentials. Note that some particles are accelerated into the wake.

For comparison, Figure 13 shows some typical electron trajectories if zero potential boundary conditions are imposed.

We want to compare Figures 11 and 12 with similar calculations in which the ion charge density is determined from tracking macroparticles.

Figure 14 shows the ion charge density that results from tracking a large number of particles with no applied potentials. The units are such that 1.81×10^4 is 10^{12} m^{-3}. While the charge density does not look smooth, it is smooth enough for potential calculations. The lower densities are on right are due to the fact that no particles are coming from the right, outside the grid.

Figure 15a shows the potentials that result from a charge density that is the sum of the ion density shown in Figure 14 and a barometric electron density, $n_o e^{-\phi/\theta}$ where $n_o = 10^{12}$ m^{-2} and $\theta = 0.1$ V. The sphere behind the disk has a fixed potential of 1V. Figure 15b shows some typical electron trajectories in these

potentials. Figures 12 and 15 are different methods of calculating the same thing. That the potentials and trajectories look the same provides us with reassurance that the calculational procedure is appropriate.

Figures 11, 12 and 13–15 do not include any electrostatic effects on the filling of the wake in the charge density and potential calculations. A comparison of Figure 13b and 15b makes it clear that particles are accelerated into the wake by the electric field due to the ion density gradient. In order to include this effect, we computed self-consistent ion densities and potentials. The final ion charge density is shown in Figure 16. The final potentials are shown in Figure 17a. Figure 17b shows some typical electron trajectories in these potentials. The wake fills in much faster and the potential is not as high or as large an area. The potential and density peaks along the axis are numeric artifacts. Interestingly, the particle trajectories are similar to those in Figures 12b and 15b.

We also did a calculation for cold ions. We computed self-consistent ion densities and potentials for ions with no thermal motion. The electrons are still modeled as barometric with a temperature of 0.1 eV. The final ion charge density is shown in Figure 18. The final potentials are shown in Figure 19a. Figure 19b shows some typical electron trajectories in these potentials. The particles plotted form a distribution for a temperature of 0.1 eV to facilitate comparison with the previous figures. The wake closes faster than in the thermal only case, but not as fast as when both effects are included. The potentials look similar to those obtained when only thermal filling was included. The trajectories span the same region of space, but show beaming.

For this case, the thermal and electrostatic filling of the wake are comparable.

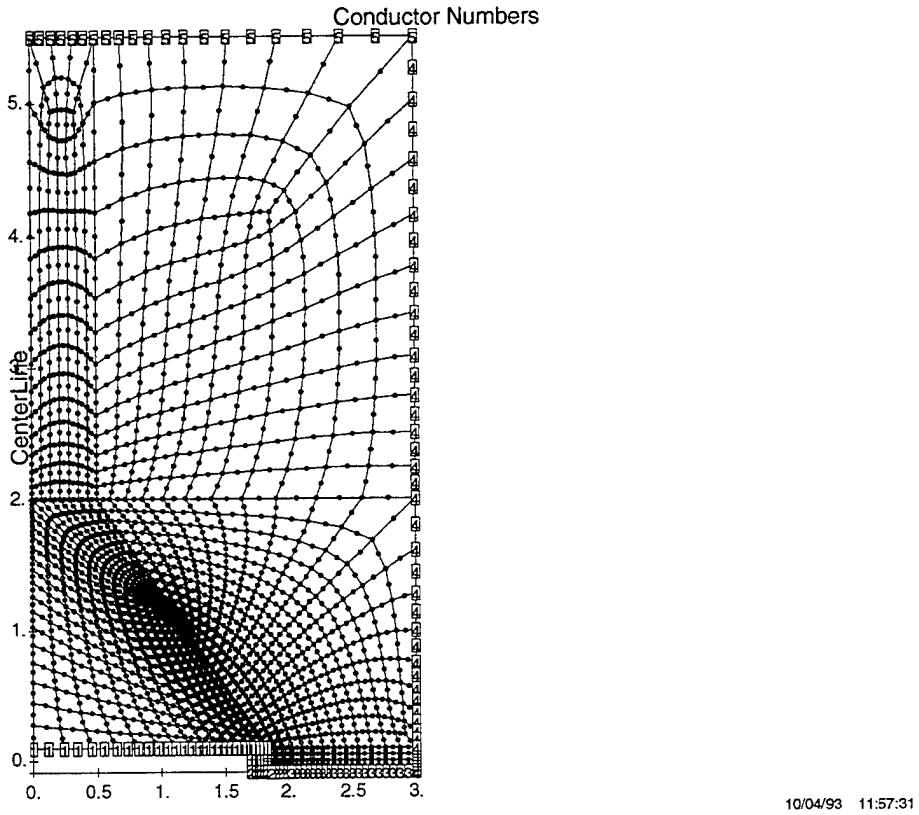

Figure 10a.

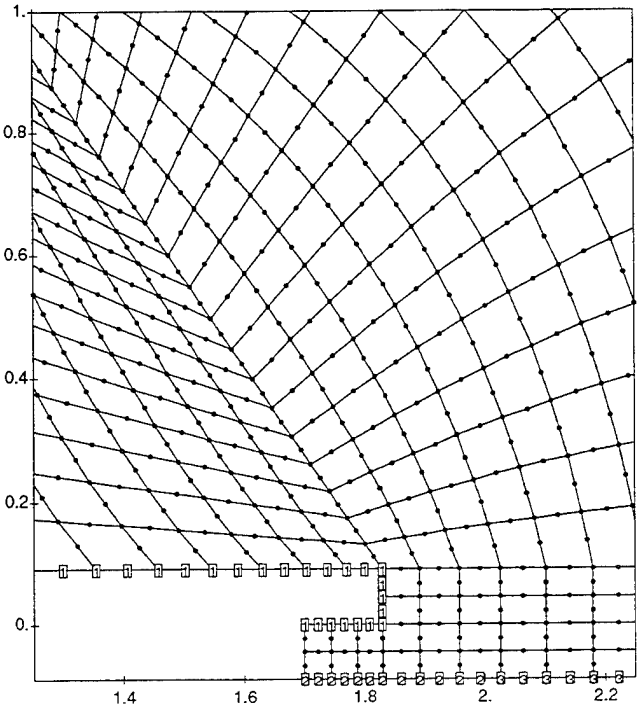

Figure 10b.

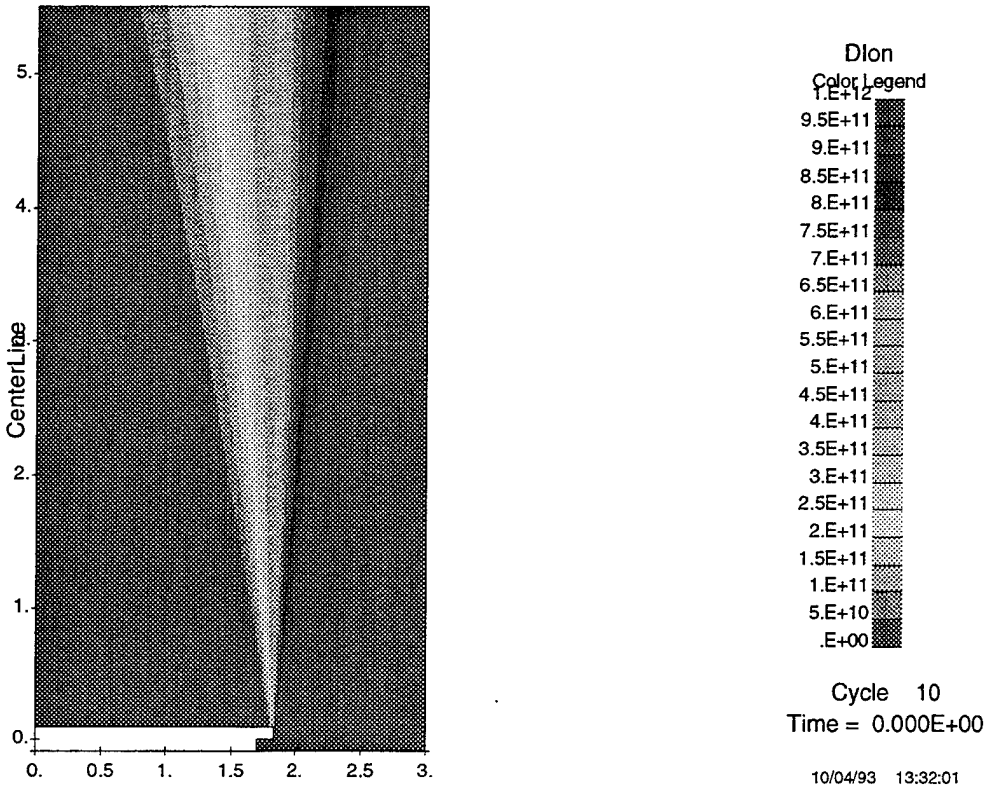
CenterLine
5.
4.
2.
1.
0.
0.
0.5
1.
1.5
2.
2.5
3.
Dion
Color Legend
1.E+12
9.5E+11
9.E+11
8.5E+11
8.E+11
7.5E+11
7.E+11
6.5E+11
6.E+11
5.5E+11
5.E+11
4.5E+11
4.E+11
3.5E+11
3.E+11
2.5E+11
2.E+11
1.5E+11
1.E+11
5.E+10
.E+00
Cycle 10
Time = 0.000E+00
10/04/93 13:32:01

Figure 11.

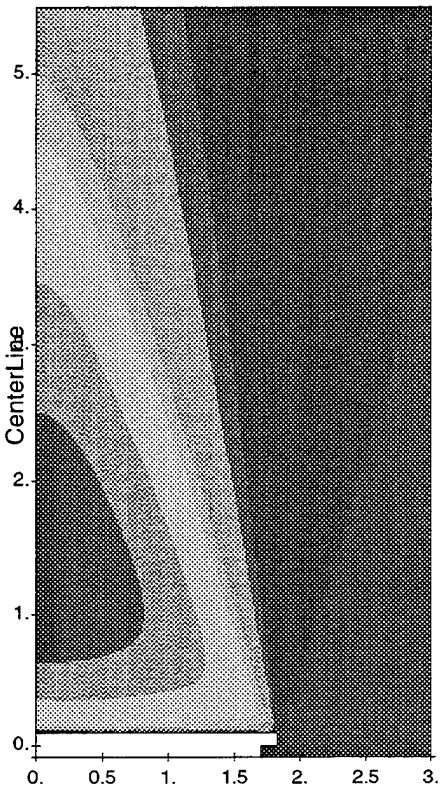

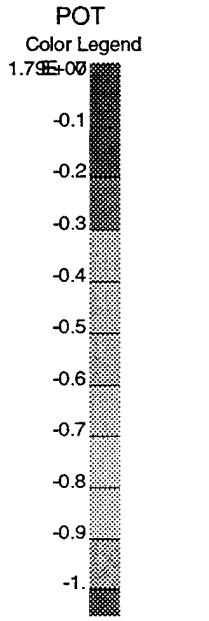

Cycle 10
Time = 0.000E+00

10/04/93 13:34:46

Figure 12a.

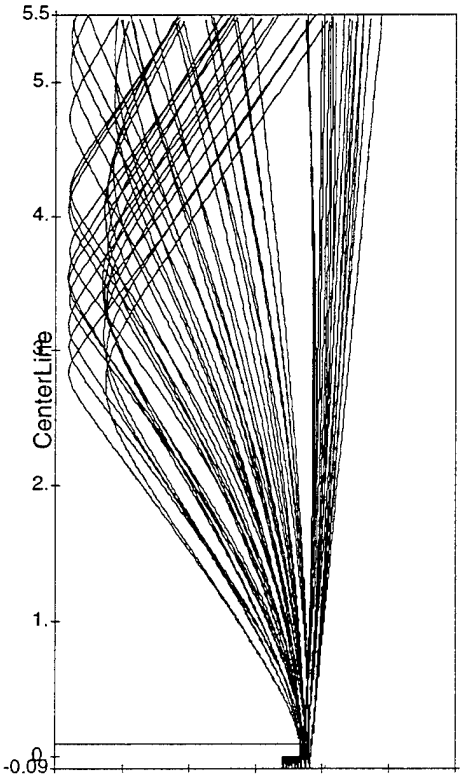

Cycle 10
Time = 0.000E+0

Figure 12b.

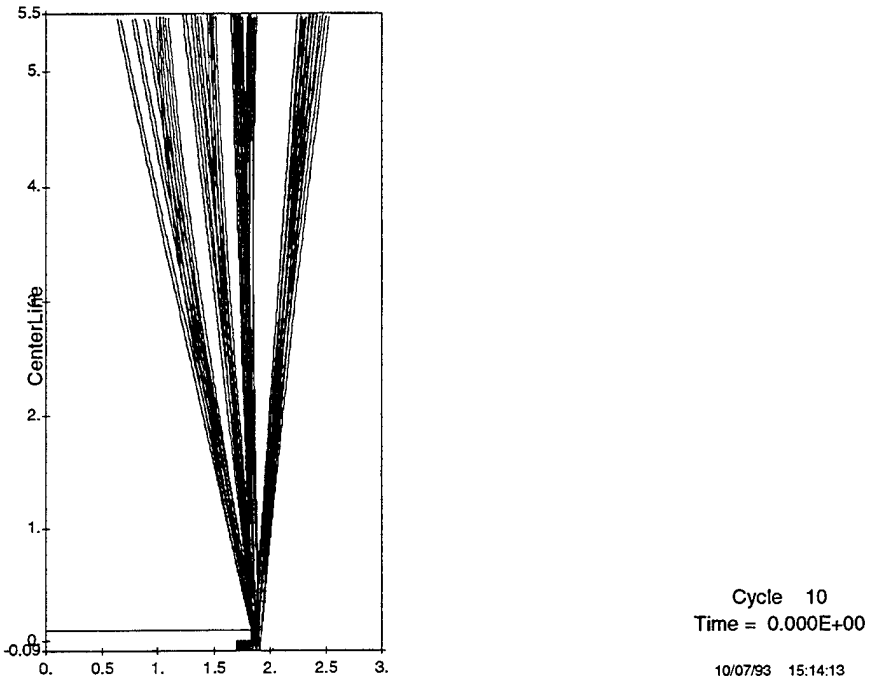

Figure 13.

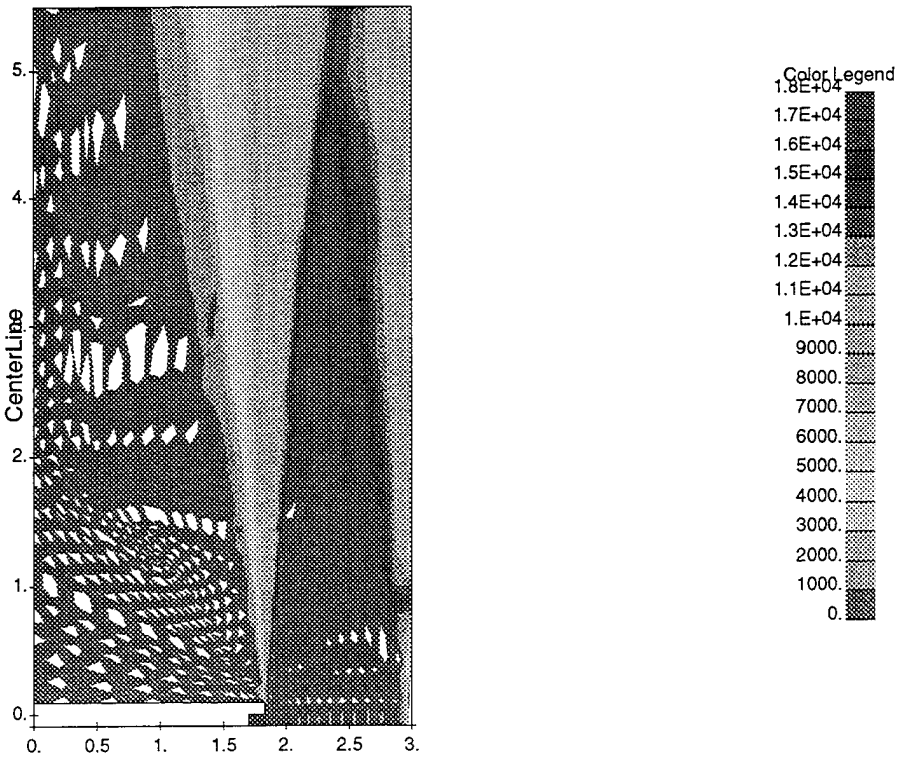

Figure 14.

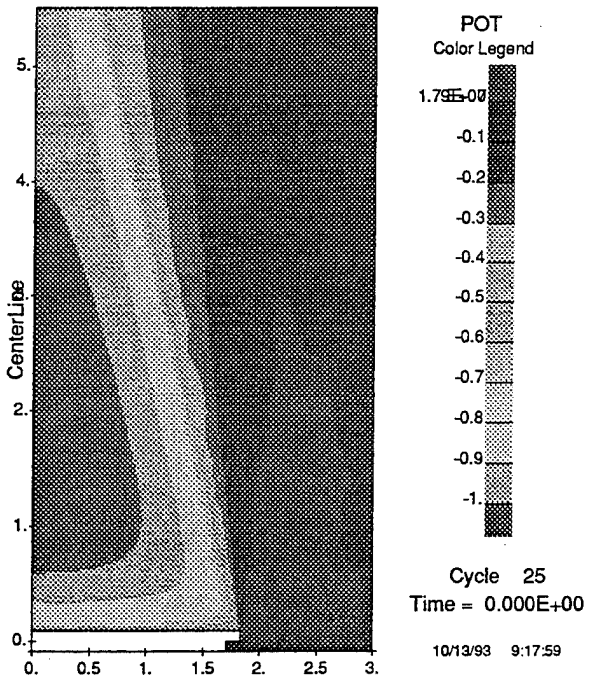

Figure 15a.

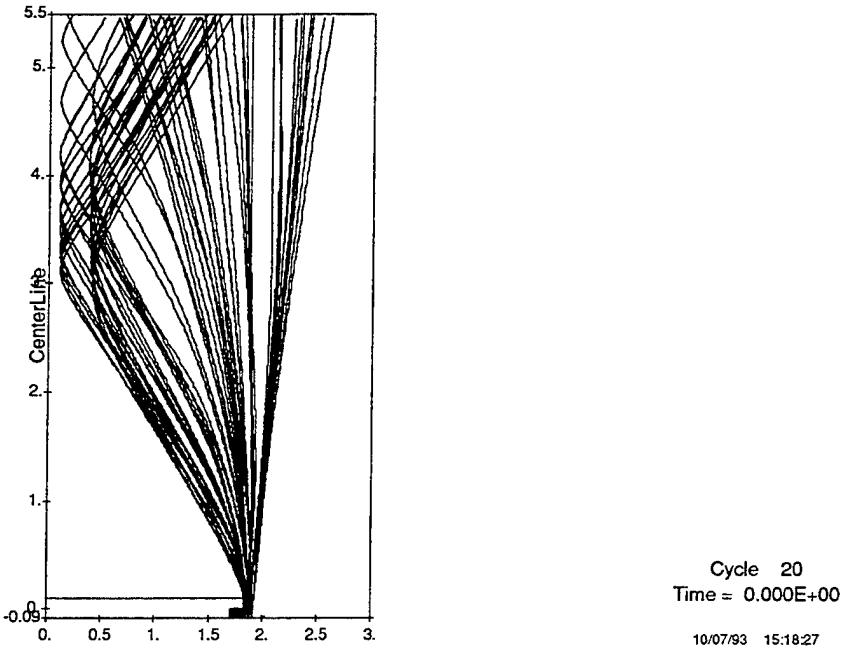

Figure 15b.

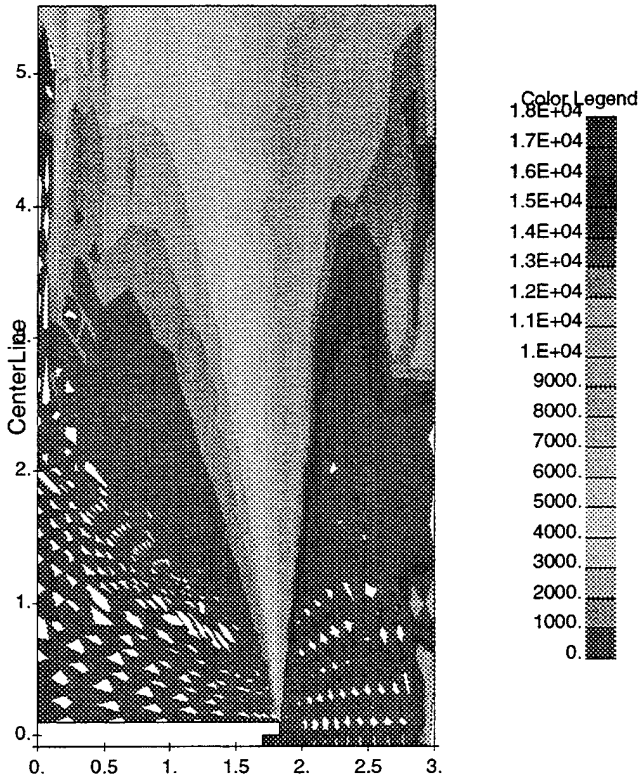
Color Legend
1.8E+04
1.7E+04
1.6E+04
1.5E+04
1.4E+04
1.3E+04
1.2E+04
1.1E+04
1.E+04
9000.
8000.
7000.
6000.
5000.
4000.
3000.
2000.
1000.
0.
CenterLine
5.
4.
2.
1.
0.
0.
0.5
1.
1.5
2.
2.5
3.

Figure 16.

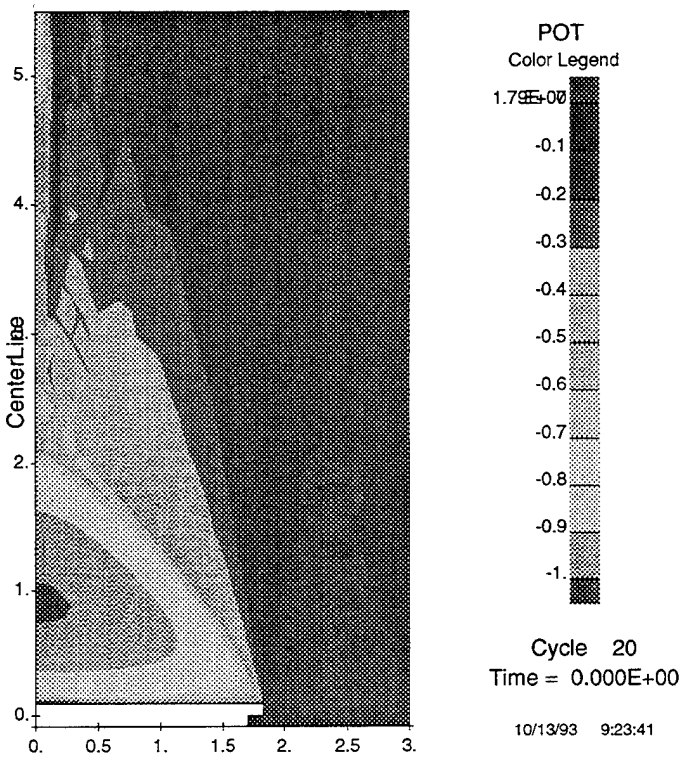

Figure 17a.

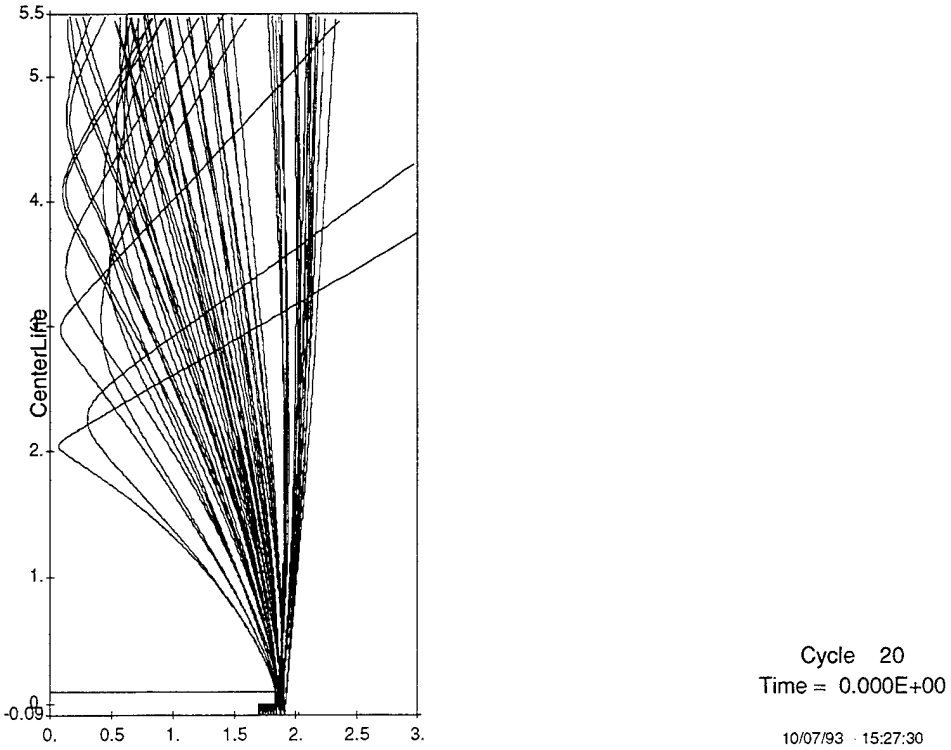

Figure 17b.

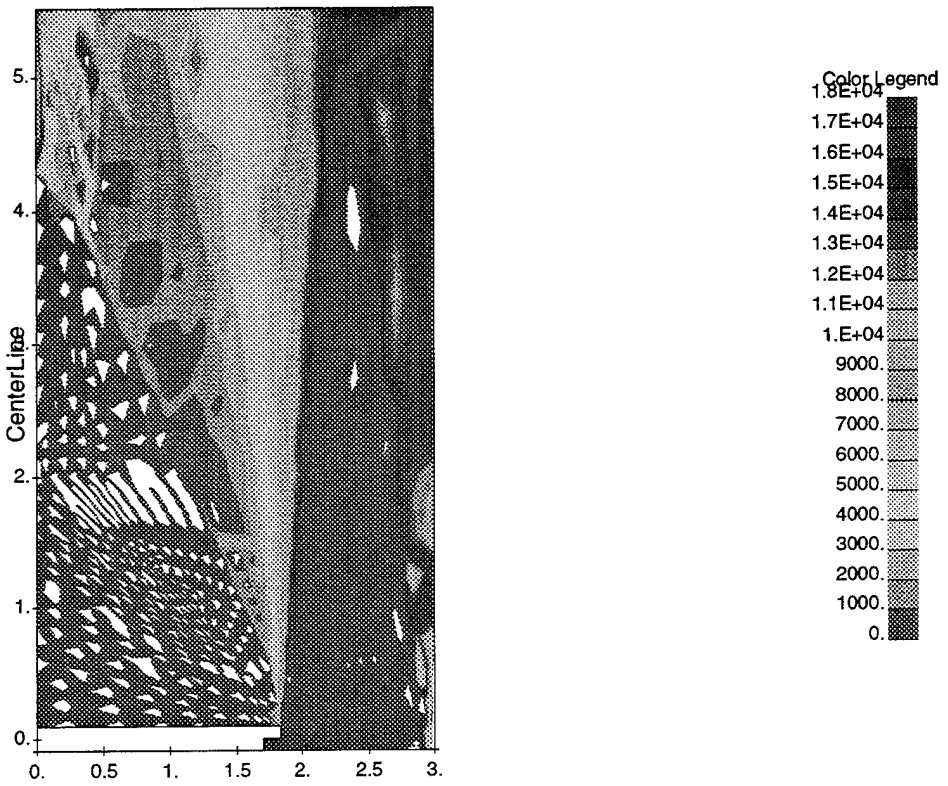
Color Legend
1.8E+04
1.7E+04
1.6E+04
1.5E+04
1.4E+04
1.3E+04
1.2E+04
1.1E+04
1.E+04
9000.
8000.
7000.
6000.
5000.
4000.
3000.
2000.
1000.
0.
CenterLine
5.
4.
2.
1.
0.
0.
0.5
1.
1.5
2.
2.5
3.

Figure 18.

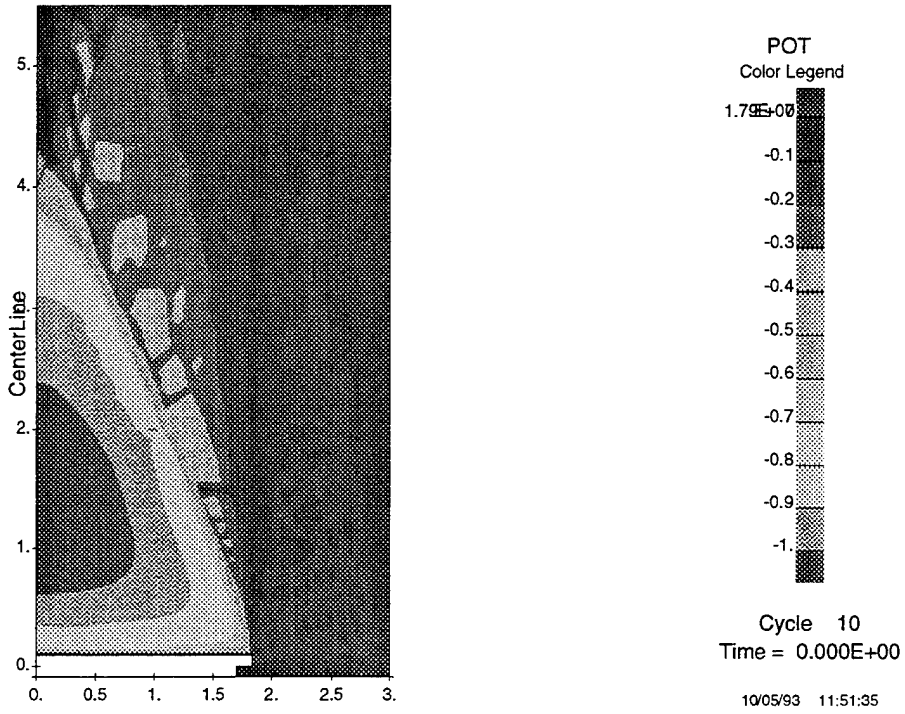

Figure 19a.

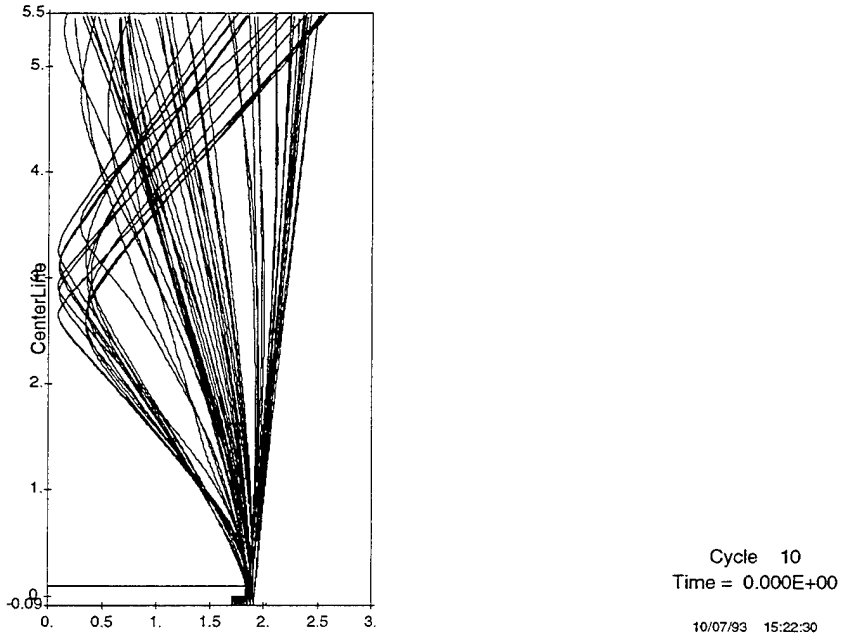

Figure 19b.

7. DYNAPAC MODELING OF CURRENT TO CHAWS WAKE SIDE DETECTOR

We have done 42 self-consistent DynaPAC calculations of the current to the CHAWS wake side probe under various conditions of probe bias, WSF tilt, WSF potential, plasma density, and hydrogen to oxygen ratio. The calculations are listed in Table 1.

Table 1. DynaPAC Calculations of CHAWS Currents

Run Code	Model	Bias [V]	Tilt [deg]	V_{WSF} [V]	$n(O^+)$ 10^{11} m^{-3}	n(H+) 10^{11} m^{-3}	Current μA	EPSAT 14 Jan 94
0	New	5000	0	0	5	0	409	510
1	Old	2000	0	0	5	0	202	233
2	New	2000	40	0	1	0	164	160
3	Old	2000	0	0	2		155	153
4	New	2000	30	0	1	0	150	145
5	New	2000	0	0	0.9	0.1	144	148
6	Old	2000	15	0	1	0	136	123
7	New	2000	15	0	1	0	129	123
8	New	2000	0	-5	1	0	115	118
9	Old	2000	0	0	1	0	115	112
10	New	2000	0	0	1	0	114	112
11	Old	2000	-15	0	1	0	105	104
12	Old	1500	0	0	1	0	87	80
13	Old	1000	0	0	1	0	59	50
14	New	1000	0	0	1	0	52	50
15	Old	700	0	0	1	0	41	32
16	New	500	0	0	1	0	22	21
17	Old	400	0	0	1	0	17.8	15
18	Old	300	0	0	1	0	12.0	10
19	Old	200	0	0	5	0	7.8	12
20	Old	200	0	0	2	0	7.0	7.3
21	Old	200	0	0	1	0	5.7	5.3
22	New	200	0	0	1	0	5.5	5.2
23	Old	150	0	0	1	0	2.9	2.9
24	New	100	40	0	0.9	0.1	12.1	13.0
25	New	100	40	0	1	0	9.2	8.0
26	New	100	40	-5	1	0	9.0	8.0
27	New	100	0	0	0.9	0.1	6.2	4.6
28	New	100	30	0	1	0	5.8	5.1
29	New	100	0	-5	1	0	3.5	3.4
30	New	100	0	-1.5	1	0	2.3	2.3
31	New	100	15	0	1	0	2.2	2.1
32	Old	100	0	0	1	0	1.3	0.8
33	New	100	0	0	1	0	0.8	0.8
34	New	50	40	-5	1	0	4.5	3.9
35	New	50	40	0	1	0	4.3	3.9
36	New	50	30	0	1	0	1.9	1.9
37	New	50	0	-5	1	0	1.5	1.4
38	New	50	0	-1.5	1	0	0.5	0.4
39	New	20	0	0	0.9	0.1	1.7	0.6
40	New	20	40	0	1	0	1.3	1.4
41	New	0	40	-5	1	0	0.4	-

For the calculations, there is a thermal distribution of ram ions emitted from the problem boundaries. The ion charge densities and currents are taken from full trajectory tracking. The electrons are represented by a Boltzman distribution.

$$n_e = n_o e^{\phi/\theta}$$

Self-consistent solutions were found in all cases.

Two models of the WSF/CHAWS system were used. The "Old" model includes only the disk and the probe. The "New" model also includes the factory and the support strut nearest the probe. WSF is modeled as a disk with radius 1.83 m and thickness 9.54 cm. It has 160 surface elements. The CHAWS wake side probe is modeled as a cylinder with radius 5.4 cm and length 45.7 cm. It is separated from the disk by 0.25 cm and has 114 surface elements. The "Old" model is shown in Figure 20. The "New" model has improved resolution on WSF near CHAWS. It has 218 surface elements for the disk, factory, and strut. The "New" model is shown in Figure 21.

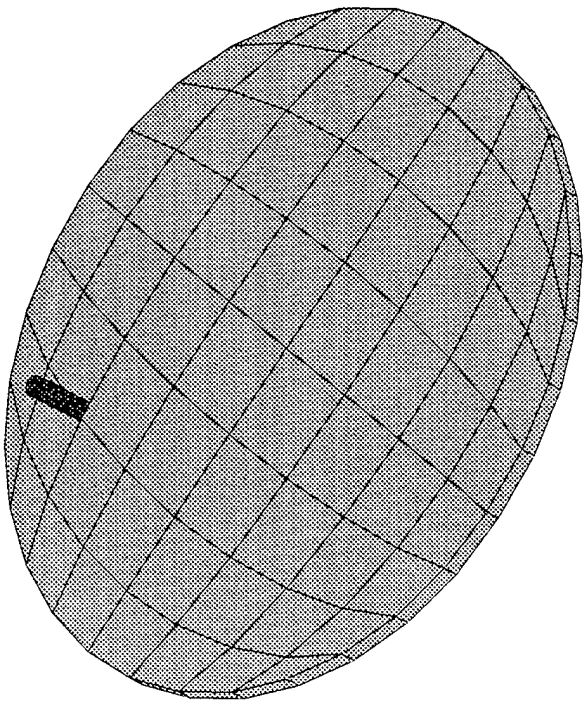

Figure 20. The "Old" model of the WSF/CHAWS system used for DynaPAC calculations.

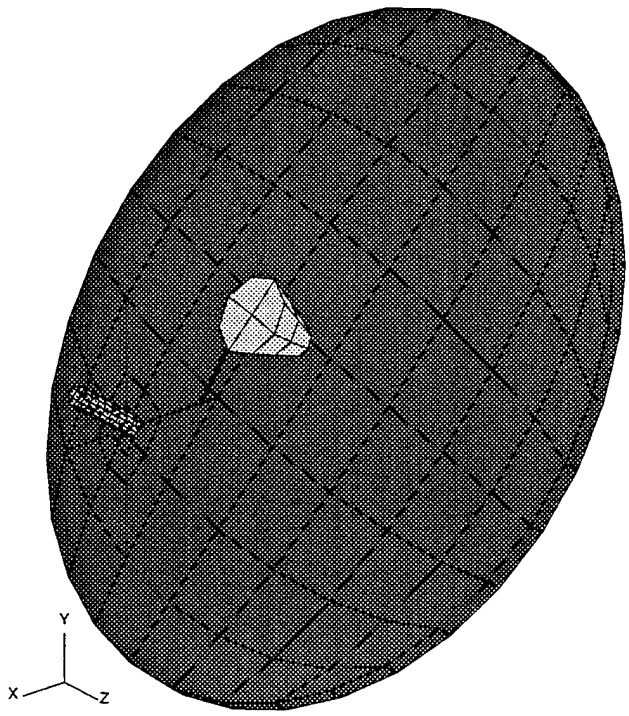

Figure 21. The "New" model of the WSF/CHAWS system used for DynaPAC calculations.

The entire object is contained within a 32 cm resolution grid. At the WSF edge the grid resolution is 8 cm. In the CHAWS region the resolution is 4 cm. The "Old" model has 2 cm resolution at the disk edge near CHAWS.

Figure 22 shows the self-consistent potentials for the case of –2 kV bias on the probe, a pure oxygen plasma with a density of 10^{11} m^{-3} and temperature of 0.1 eV, no tilt, and no potential on the disk. Note that the potentials extend 40 cm beyond the edge of the disk. The total charge within the high potential regions is that needed to shield the probe potential. The extent of the high potential region beyond the shield is always large enough to attract enough current to provide the shielding. While the high potential region is smaller for higher densities, the current collected is only weakly dependent on density.

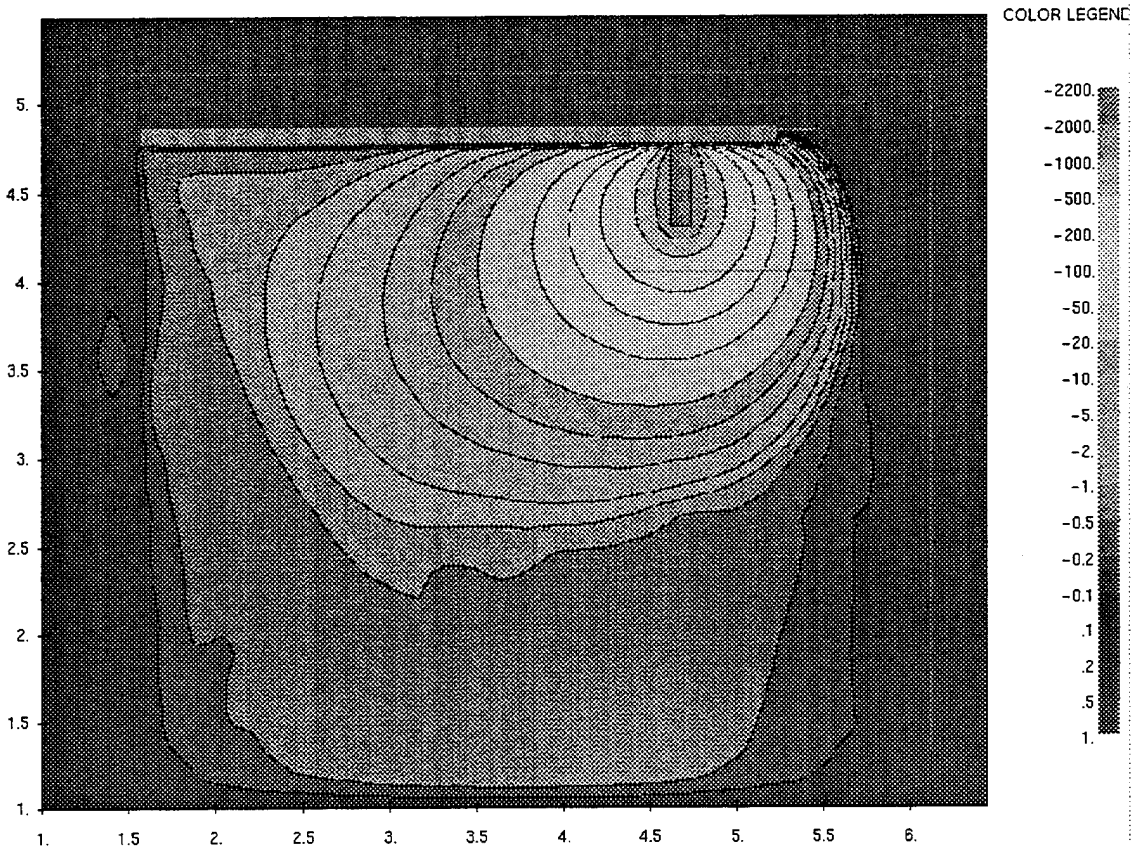

Figure 22. Self-consistent potentials for the case of –2 kV bias on the probe, a pure oxygen plasma with a density of 10^{11} m^{-3} and temperature of 0.1 eV, no tilt, and no potential on the disk.

Figures 23a and 23b show ion trajectories for ions that started in a plane through the center of the disk and probe and the ion charge density in this plane for the case shown in Figure 22. There are 48 ion trajectories from each boundary point to represent the thermal distribution. There are few ions between the disk edge and the probe. There is a region of high ion charge density where the bulk of the ions flow. Figure 24 shows four typical trajectories. The most strongly attracted ions strike the outboard side of the probe within a few centimeters of the tip. The tip surface has a high current density of ions striking at oblique angles. The tipward portion of the inboard side of the probe is shadowed by the tip, but a large current is collected on the inboard side beyond the shadowed region. These ions are typically incident at about 30 degrees. The location of the peak of this current depends on the probe potential and the disk tilt with respect to the ram flow. Finally, ions deflected by the far-field contribute to the filling of the wake.

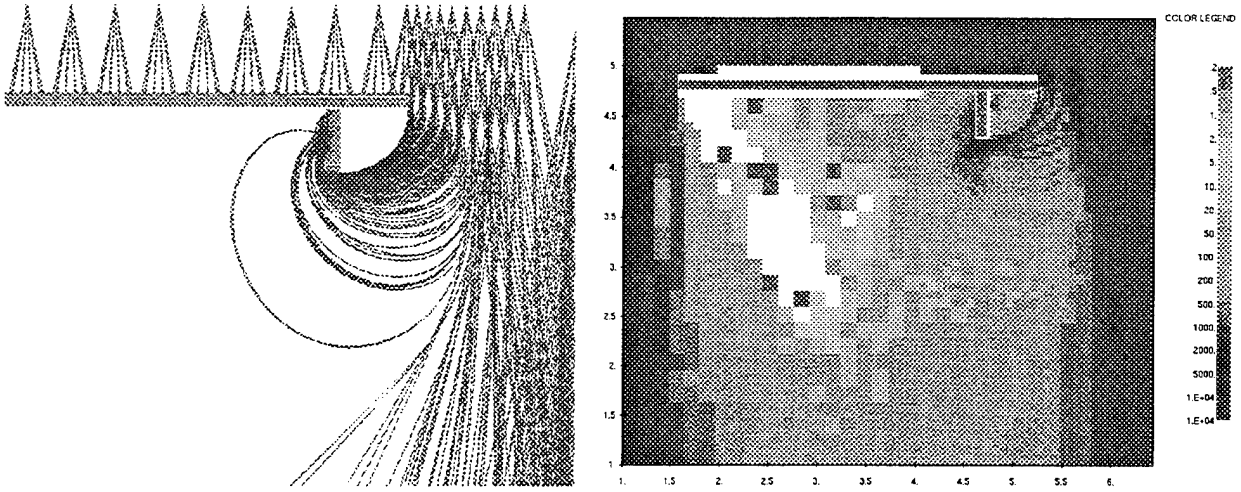

Figure 23 (a) Ion trajectories for ions that started in a plane through the center of the disk and probe. (b) Ion charge density in this plane for the case shown in Figure 22.

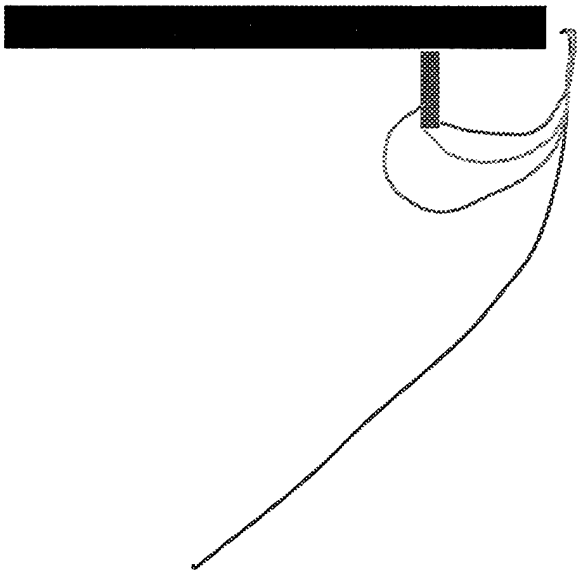

Figure 24. Four typical ion trajectories.

Figure 25 shows the current to the probe as a function of probe potential for all the calculations. The incident current is fairly linear with a threshold at 100 V bias. The threshold is lower and the current greater when the disk is tilted so that the probe is toward the ram flow; with 40 degree tilt significant current is collected at 20 V bias. Tilting away from the ram flow provides a moderate reduction in current. Current is also increased by negative bias of the entire disk.

The presence of H^+ in the plasma also increases the collected current. At high bias the H^+ current is about four times the corresponding current from O^+. Near or below threshold, a small amount of ambient H^+ contributes the bulk of the current to the probe.

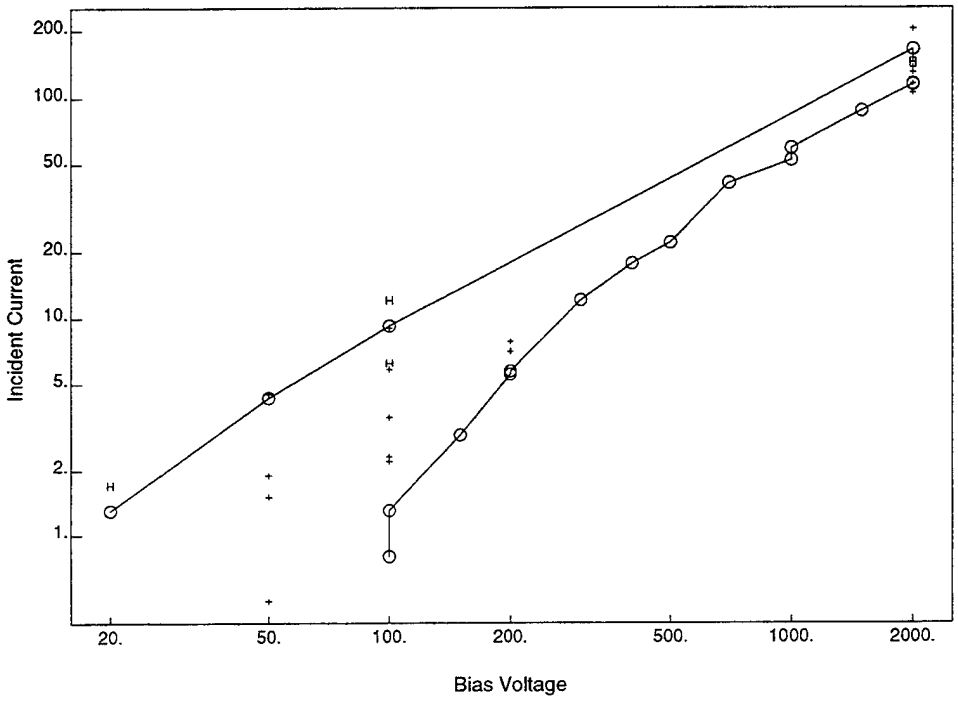

Figure 25. Total ion current [μa] to the probe as a function of probe potential. The lines connect points for density 1 x 10^{11} m^{-3}, no bias on the WSF, and tilts of zero degrees (lower) and 40 degrees into flow (upper). Points plotted with "H" contain ten percent H^+. Points plotted with "+" represent various other conditions, including increased density, negative bias on WSF, other tilt angles, and combinations thereof.

There are three regions of high current density to the CHAWS probe. On the probe tip the peak flux is toward the inboard edge. The diffuse spot on the inboard side varies in location and size with problem parameters. The peak moves toward the tip with increasing plasma density or increasing negative bias. The peak is near the WSF surface at threshold. The peak flux at the inboard detector location occurs when the disk is tilted 15 degrees away from the ram flow. On the outboard side, the flux is within a few centimeters of the tip and increases with increasing plasma density. The peak current regions become more diffuse as the temperature increases or the hydrogen fraction increases.

WSF Wake Side Ion Currents

The question has arisen as to whether biasing the CHAWS probe induces ion current to the wakeward side of the WSF. This information is available through analysis of the DynaPAC runs. Table 2 lists the total wake side current and (for a few cases) the current density at the WSF wake side center. (The central current density is always within a factor of two of the mean density to the 10 m^2 surface.) All the listed runs use the "New" model, have plasma density of $1x10^{11}$ m^3, and (with few exceptions) assume pure O^+.

Table 2. Ion currents to WSF wakeward surface for selected DynaPAC runs. Asterik denotes a 10% H^+ concentration.

Run Code	Bias [V]	Tilt [deg]	V_{WSF} [V]	WakeSide Current [μA]	Central Density [μA m^{-2}
40	20	40	0	0.9	0.1
16	500	0	0	0.9	
10	2000	0	0	1.0	
39*	20	0	0	1.0	
33	100	0	0	1.3	
38	50	0	-1.5	1.3	
31	100	15	0	1.4	
2	2000	40	0	1.4	
27*	100	0	0	1.5	
30	100	0	-1.5	1.6	
5*	2000	0	0	1.7	
28	100	30	0	2.0	
25	100	40	0	2.2	0.2
8	2000	0	-5	11	2
37	50	0	-5	14	
29	100	0	-5	14	2
41	0	40	-5	31	2
26	100	40	-5	32	2

From the table the conclusion is clear. In the nominal plasma we get about 1 μA of ions to the wake surface of the WSF. The degree of v x B charging produced by the WSF alone, or the presence of H^+ in the plasma, or tilting of the WSF by up to 40 degrees, produce only modest increases in the wake side

current. Bias of the CHAWS wake side probe has no obvious systematic effect. However, when the WSF is biased five volts negative (as a result of being mounted on the RMS) the current can increase by more than one order of magnitude. The current density to the center of the wake surface, which is normally about 0.1 $\mu A\, m^{-2}$, can increase to 2 $\mu A\, m^{-2}$. Note that the currents cited above are for a plasma density of $1x10^{11}\ m^{-3}$, and will vary at most linearly with density.

To repeat the main conclusion, bias of the CHAWS wake side probe has no obvious systematic effect on the current to the wakeward surface of the WSF.

Fit to DynaPAC Results for CHAWS Total Current

The DynaPAC results for CHAWS total current were fit for the purpose of extending the results to arbitrary plasma density, temperature, and composition, CHAWS bias potential, WSF tilt angle, and WSF potential. This fit was then incorporated into the EPSAT code. Because of the limited space spanned by the runs, dependence on some parameters represents actual fits, while dependence on other parameters is through application of not-strictly-applicable theoretical treatment, or through ad-hoc functions fit to very little data. Table 1 shows the full set of DynaPAC runs, together with the total current values computed by EPSAT using the fit described below.

The primary fit is for the range of parameters shown in Table 3. The procedure was to (a) calculate the Langmuir-Blodgett current, I_{LB}, in the given plasma conditions to a 0.11 meter radius sphere at the bias voltage; (b) plot $I_{DynaPAC}/I_{LB}$ vs. $\log_{10}V$ for each of the four angles; (c) fit a straight line

$$F(V, \phi) = I_{DynaPAC}/I_{LB} = a(\phi) + b(\phi)\log_{10}V$$

where ϕ is the tilt angle, defined to be positive for tilt of the probe away from the ram flow. Table 4 shows the values of $a(\phi)$ and $b(\phi)$ resulting from the fit. The fitting lines and the points fit are shown in Figure 26.

Table 3. Range of parameters for primary fit to DynaPAC total currents to CHAWS probe.

Parameter	Value of Range
Plasma Density	1×10^{11} m^{-3}
Plasma Temperature	0.1 eV
Plasma Composition	100% O+
Spacecraft Velocity	7800 m s-1
Probe Bias	-20 to -2000 Volts
WSF Tilt	0°, -15°, -30°, -40°

Table 4. Fitting parameters for the four WSF tilt angles.

Angle	Parameters	
ϕ	a (ϕ)	b(ϕ)
0	-0.4351	0.3661
-15	-0.3686	0.3613
-30	-0.1647	0.3218
-40	-0.0563	0.2632

To extend the fit to arbitrary WSF angles, we linearly interpolate for negative angles, and linearly extrapolate for positive angles, using half the slope in the interval [-15°, 0°]. Then, the fit to the current can be evaluated by calculating the Langmuir-Blodgett current to the assumed equivalent 11 cm radius sphere and multiplying by F(V, ϕ) for the appropriate voltage and tilt angle.

Dependence on parameters other than voltage and tilt angle are handled as follows:

Plasma Density: The plasma density is assumed to enter only through the Langmuir-Blodgett formulation, leading to current proportional to the 3/7 power of density. This predicts a somewhat higher density dependence than shown by the calculations.

Plasma Temperature: Similarly, we assume the temperature dependence to come from Langmuir-Blodgett. This predicts current proportional to the 3/14 power of temperature. Within the expected temperature range, this is not much different from no dependence whatever.

Plasma Composition and Spacecraft Velocity: We assume that the bias potential appearing in $F(V,\phi)$ should be scaled by the ram energy for each species. That gives

$$\frac{I_{Fit}}{I_{LB}} = \sum_i C_i \sqrt{\frac{16}{M_i}}\, F\left(\left(\frac{16}{M_i}\right)\left(\frac{7800}{V_{sc}}\right)^2 V, \phi\right)$$

where I_{LB} is computed for pure O^+, the sum is over species, c_i is the fractional concentration of species i, V_{sc} is the actual spacecraft velocity, and M is the species mass in AMU. (We limit the first argument of F to 2500 volts.) This appears do to fairly well at high potential or tilt angle, but underestimates the low mass species currents for low voltages with no tilt.

WSF Potential: The dependence on WSF potential is small for high bias or for strong tilt into the ram. We somewhat arbitrarily add to $F(V, \phi)$ a term $0.57(1 + \phi/40)\,(V_w/V)^{1/2}$ (where V_w/V is the ratio of the disk potential to the bias voltage), which gives a reasonable fit to most of the available calculations.

The last column of Table 1 shows the EPSAT-calculated currents for comparison with the DynaPAC runs. Overall, the fit is quite good.

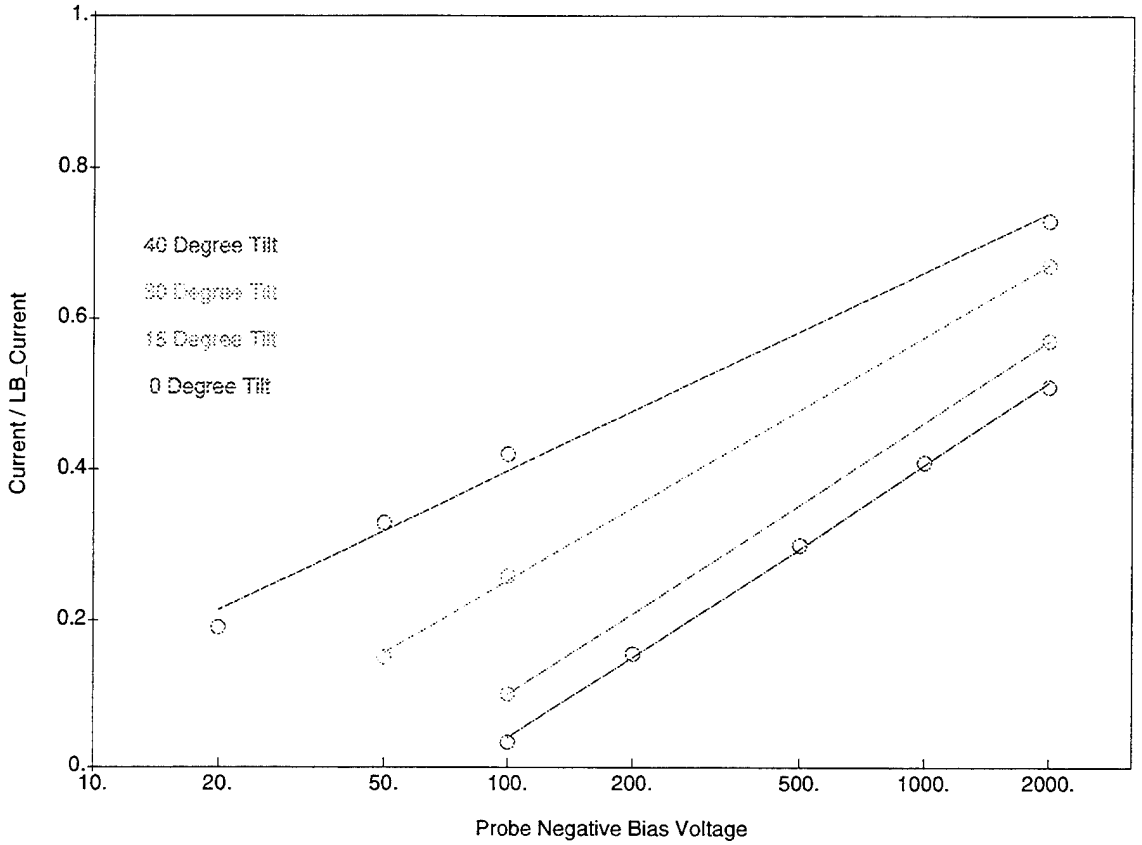

Figure 26. DynaPAC computed current normalized by the Langmuir-Blodgett current as a function of the logarithm of the probe voltage. The points are the calculations and the lines the fit.

Detector Angular Distributions

Most of the runs have been analyzed for particle distributions to the detectors. (Runs likely to be duplicative, or having excessively low total current, are omitted.) These analyses are based on the particle files, which list every ion hitting the WSF or CHAWS. The particles hitting the surface cells neighboring each detector location are assigned to that detector. The detector current is then divided into bins according to the angle each particle makes with the detector's axial direction. In addition, each detector is assigned a subsidiary direction, and each bin is subdivided (by color) according to the sign of the velocity component along the subsidiary direction. Light gray means along the subsidiary direction, while dark gray means opposite the subsidiary direction. The histograms follow this section. Table 5 shows how each detector is characterized.

Table 5. Identification of detectors with calculational surface cells.

Detector	Cells	Area [cm^2]	Subsidiary Direction
Inboard	33,55	32	Toward WSF
Outboard	7,81	32	Toward WSF
Side	12,34,60,82	64	Outboard
Tip	110	16	Outboard

Each detector is sensitive only to particles entering nearly along the detector axis ($\cos\theta > 0.9$). With this factor taken into account, in nearly all the 100 detector cases analyzed, the detector will see only a small current of atypical ions. To determine whether a detector sees a significant current of mainstream ions, we loosely apply the following three criteria:

(1) The current density to the detector must be a sensible fraction (>0.1) of the mean current density to the CHAWS sensor; and

(2) The weight in the near-axial angular bin(s) must be a sensible fraction (>0.3) of the maximum bin weight.

(3) The particle number to the detector must be sufficient to support the above two criteria.

By this criterion, significant mainstream current is seen in 24 cases, as seen in Table 6. The cases preceded with an asterisk (*) satisfy the more stringent criteria of current density at least equal the mean to the probe, with an angular distribution not substantially below the maximum at normal incidence.

Table 6. Cases with significant current incident on detectors.

Run Code	Detector	Species	Direction
3	Inboard	O	Toward WSF
4	Side	O	Inboard (?)
5	Inboard	O	Toward WSF
*5	Tip	H	Both
7	Inboard	O	Toward WSF
7	Outboard	O	Away WSF
*10	Side	O	Outboard
*10	Inboard	O	Toward WSF
*11	Side	O	Outboard
*11	Inboard	O	Toward WSF
*12	Inboard	O	Toward WSF
*14	Inboard	O	Toward WSF
16	Side	O	Inboard
*16	Inboard	O	Both
*20	Outboard	O	Away from WSF
22	Outboard	O	Away from WSF
24	Side	H	Inboard
24	Tip	H	Inboard
24	Outboard	H	Away from WSF
*26	Outboard	O	Away from WSF
27	Side	H	Inboard
27	Outboard	H	Both
27	Tip	H	Both (?)
*34	Outboard	O	Away from WSF

Some additional comments:

(a) The highest current density generally occurs at the tip. (In fact, on the outboard edge of the tip.) Nonetheless, we will rarely see this current because none of it is normally incident on the detector.

(b) Current to the inboard detector is sporadic, depending on where the current peak on the inboard side is located. Highly noteworthy is Run Code 11

(2 kV bias tilted 15 degrees away from the ram) for which the current peak falls directly on the inboard detector.

(c) When hydrogen ions are present, their distribution over surface and angle is far broader than for oxygen. It should be expected that, if any appreciable hydrogen concentration is present in the ambient ionosphere, the current seen by the detectors will be mostly hydrogen, even if most of the total probe current is oxygen.

Run Code 1 N = 5x10^11

2000 Volts Bias <J> = 1.23x10^-3

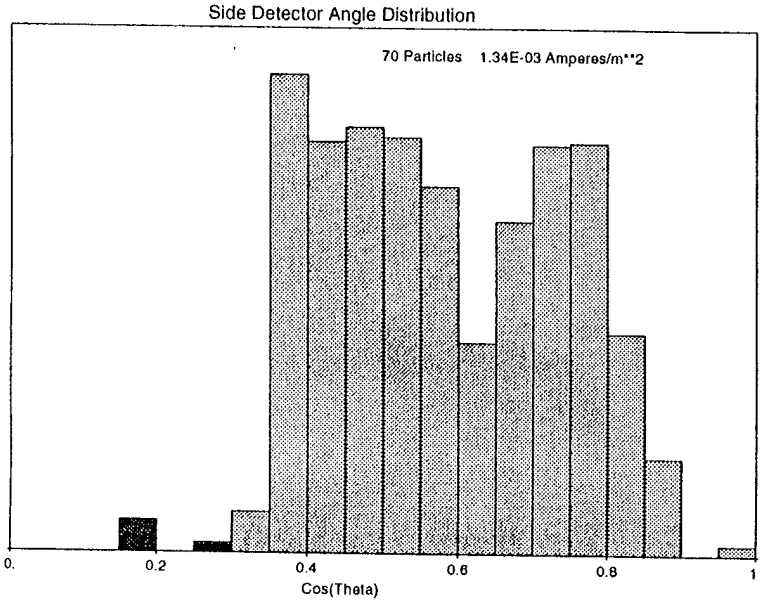

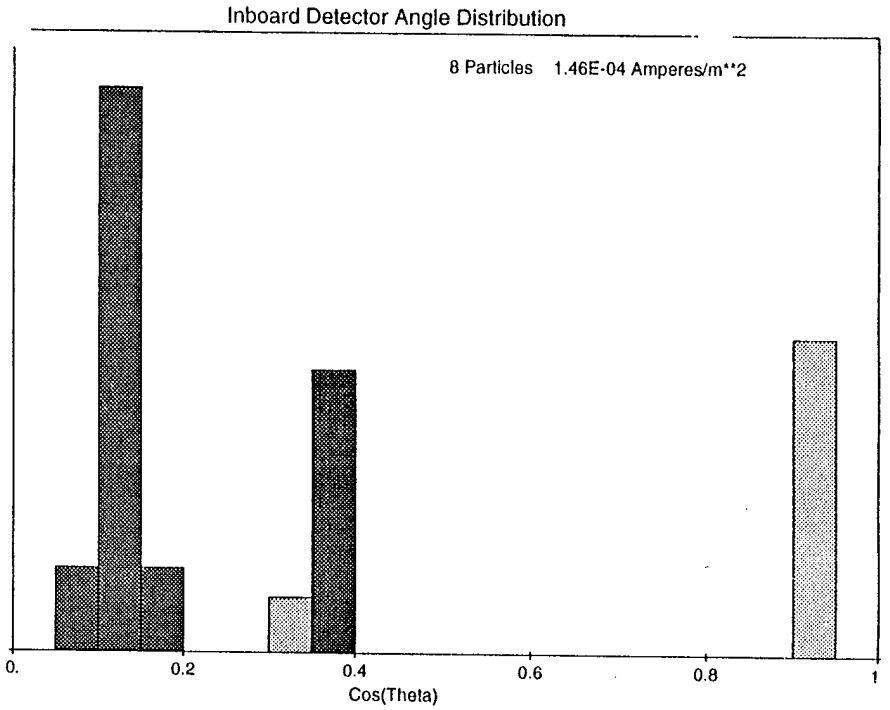

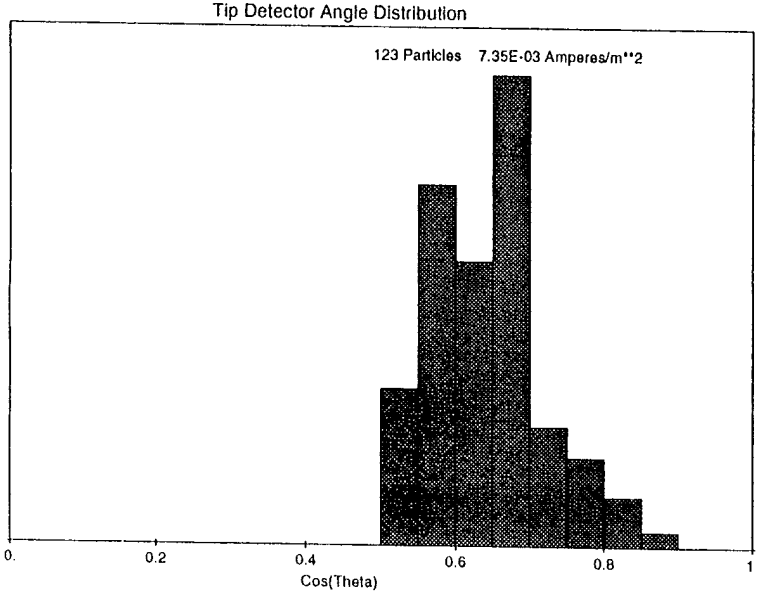

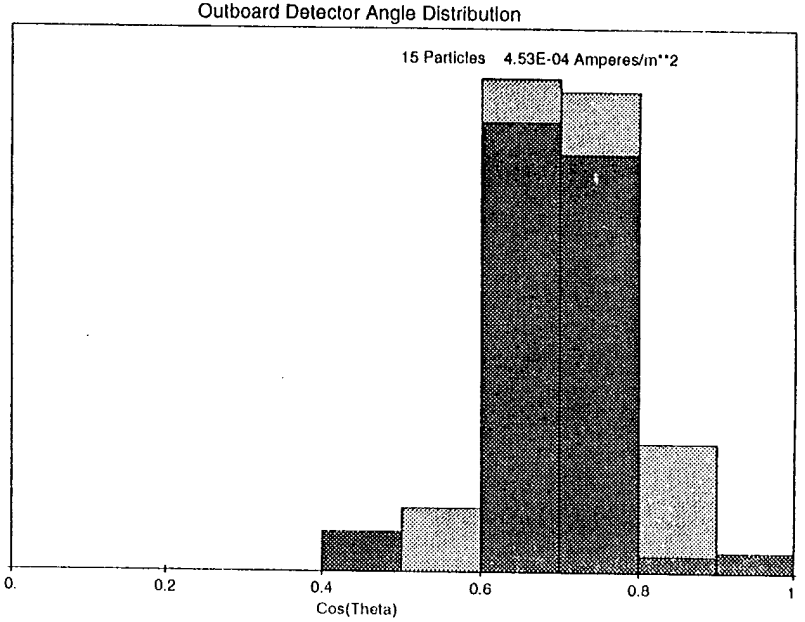

Run Co. ɜ 2 40 deg. Tilt

2000 Volts Bias <J> = 1.0x10−3

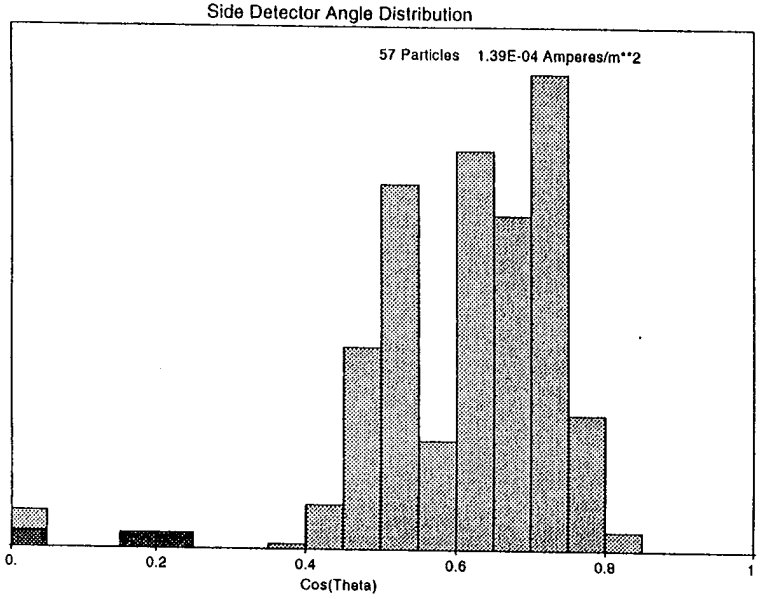

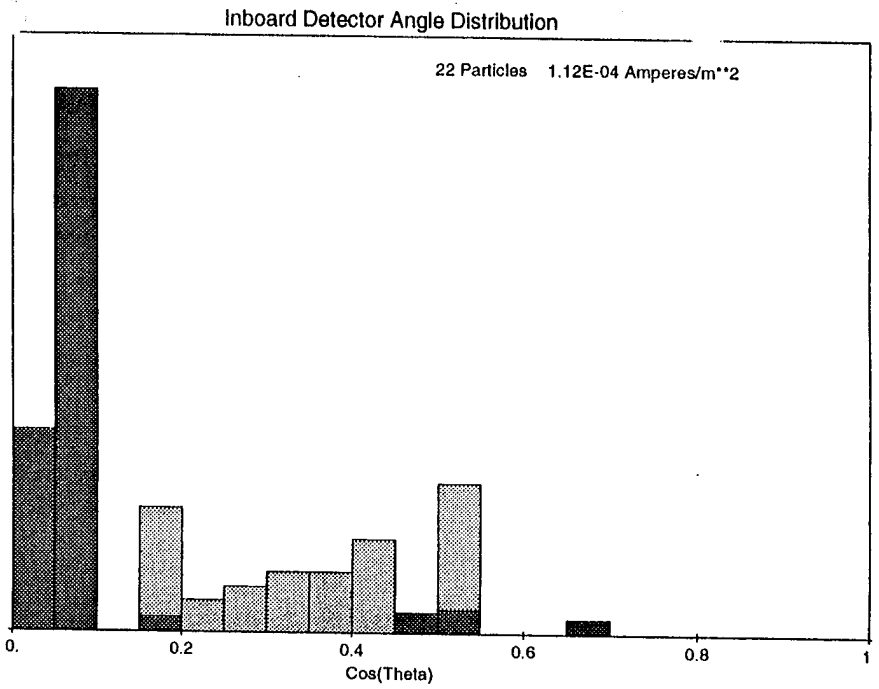

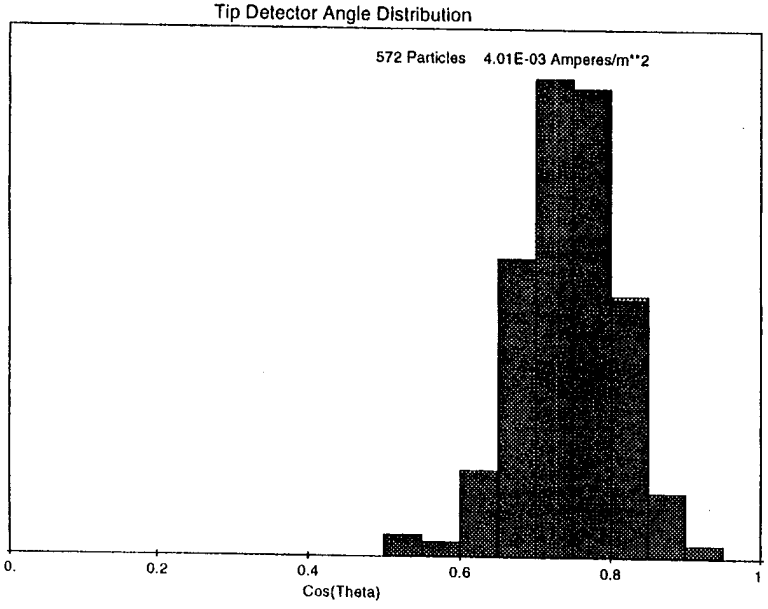

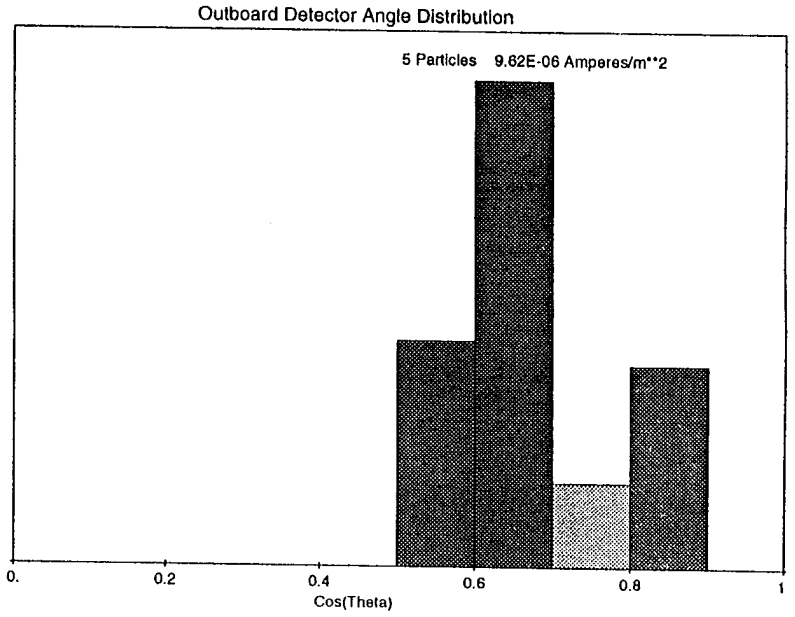

Run Code 3 N = 2x10^11

2000 Volts Bias <J> = 9.5x10−4

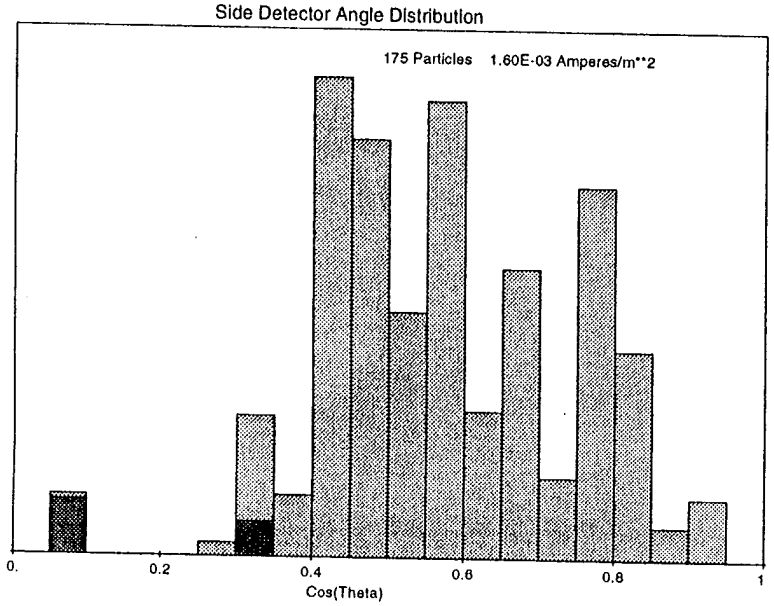

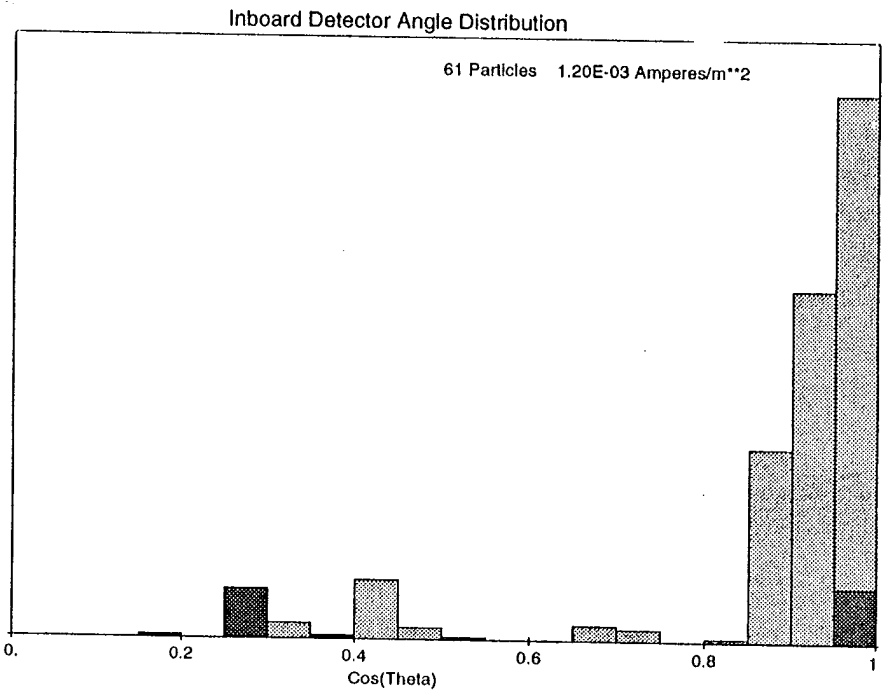

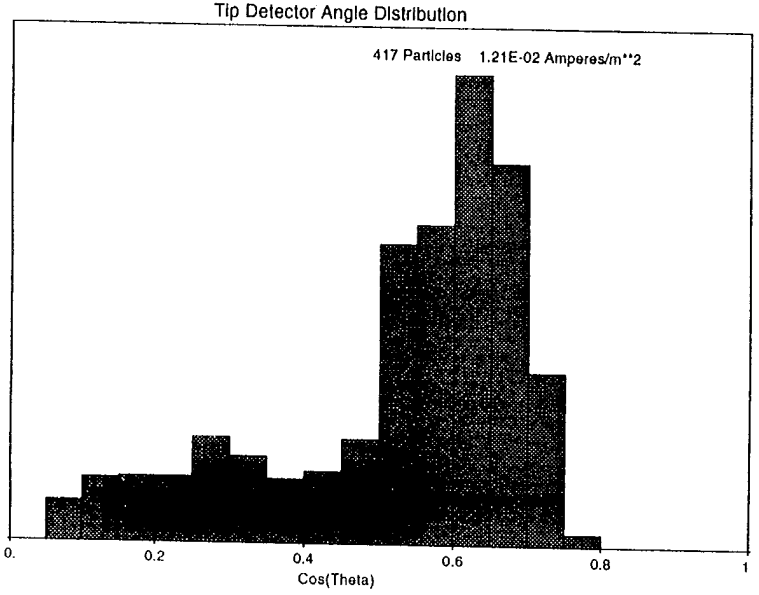

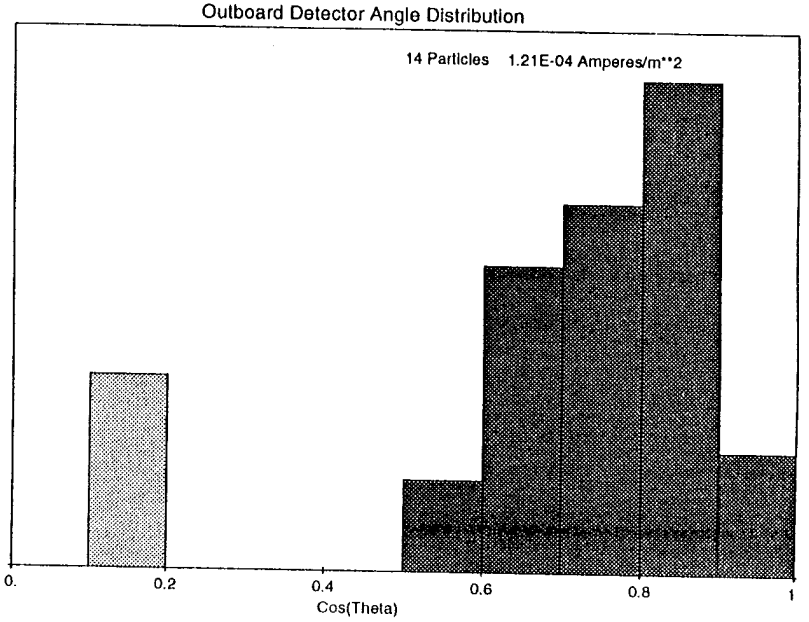

Run Cc .e 4 30 deg. Tilt

2000 Volt Bias <J> = 9.1x10−4

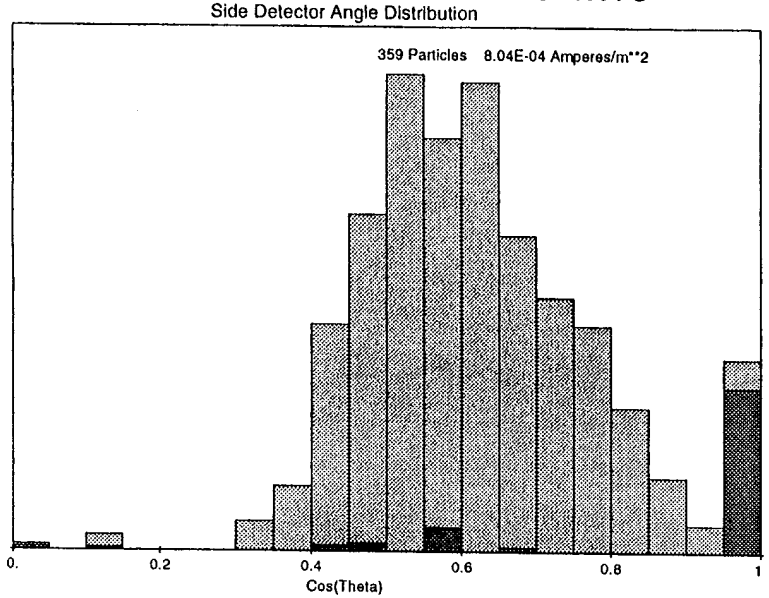

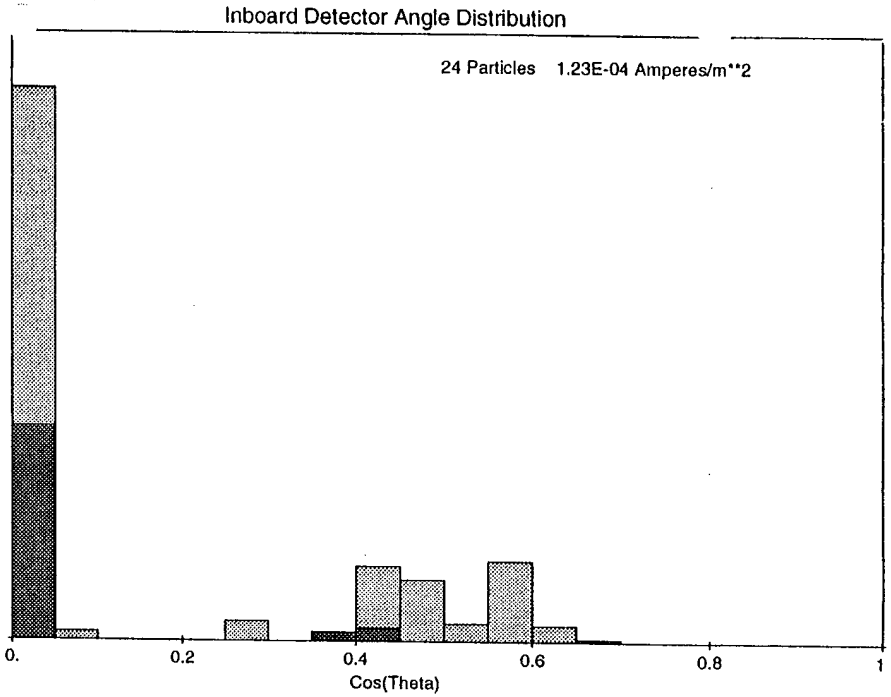

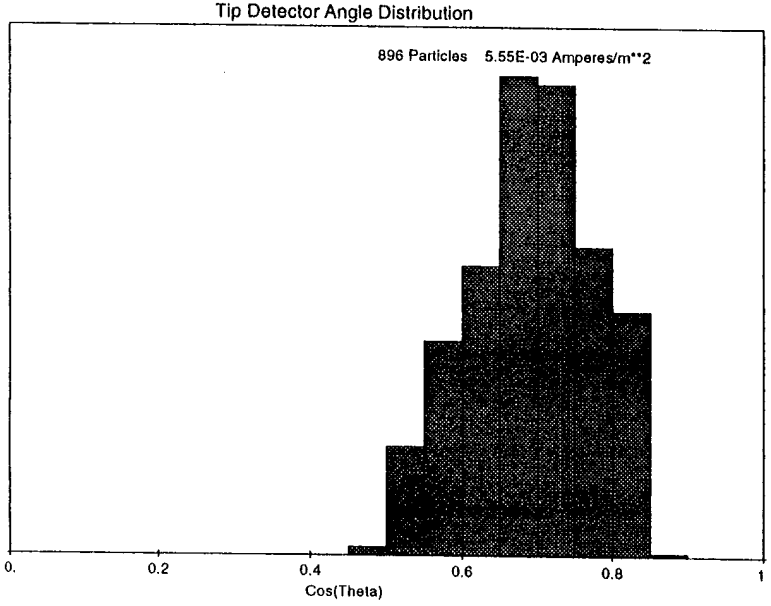

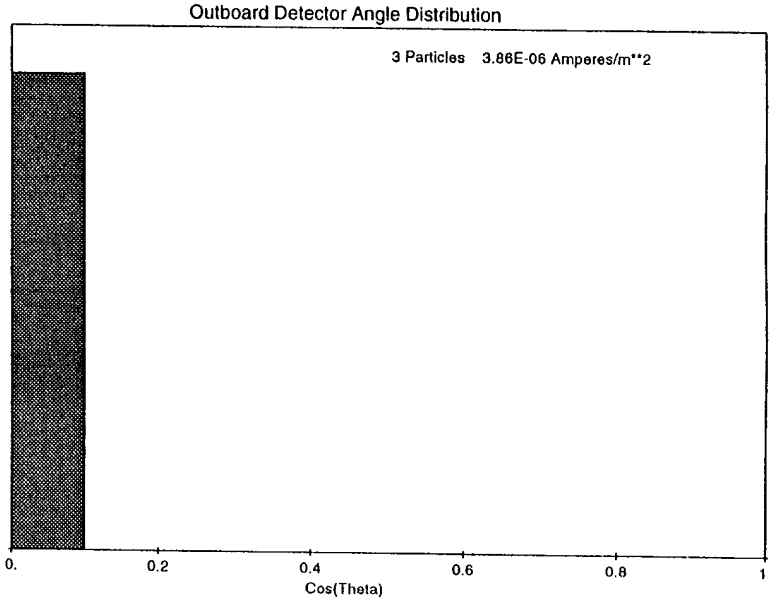

Run Cc ə 5 10% H <J> = 8.8x10−4

2000 Volts Bias (O only distribution)

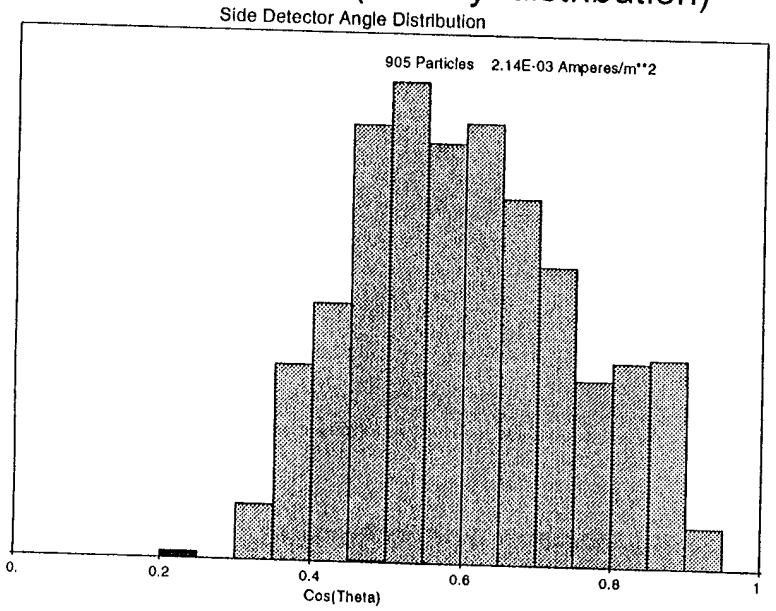

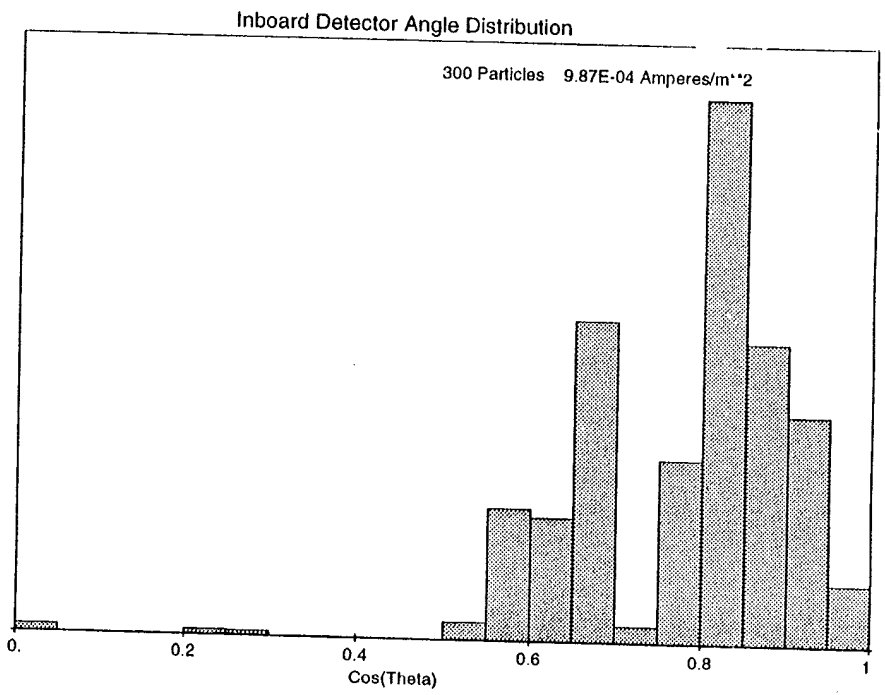

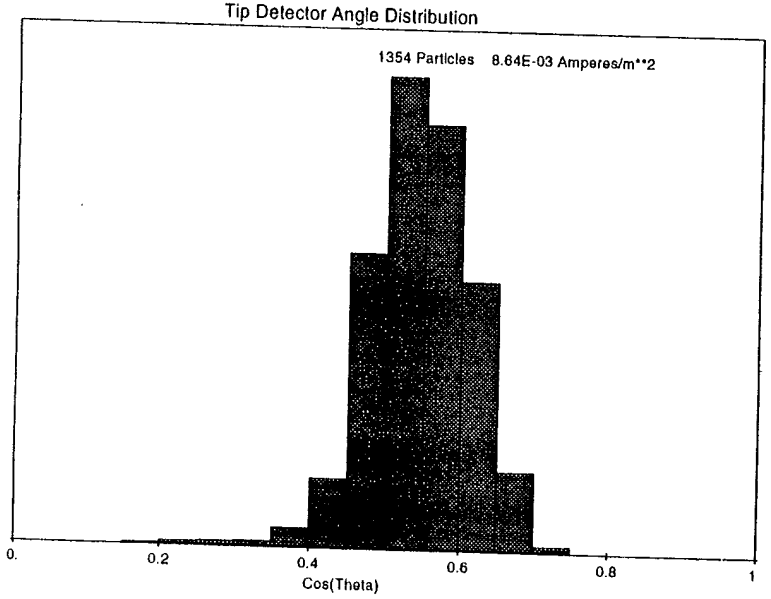

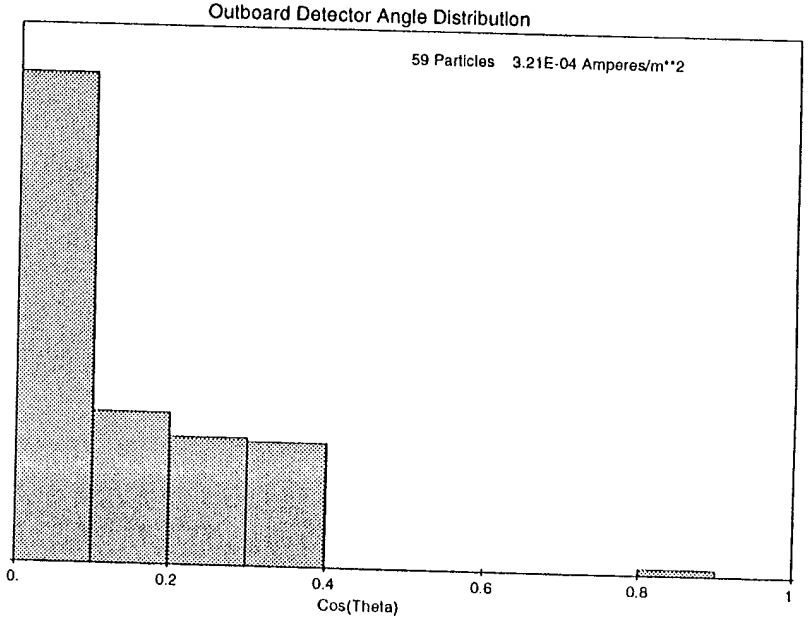

Run Co › 5 10% H <J> = 8.8x10−4

2000 Volts Bias (H only distribution)

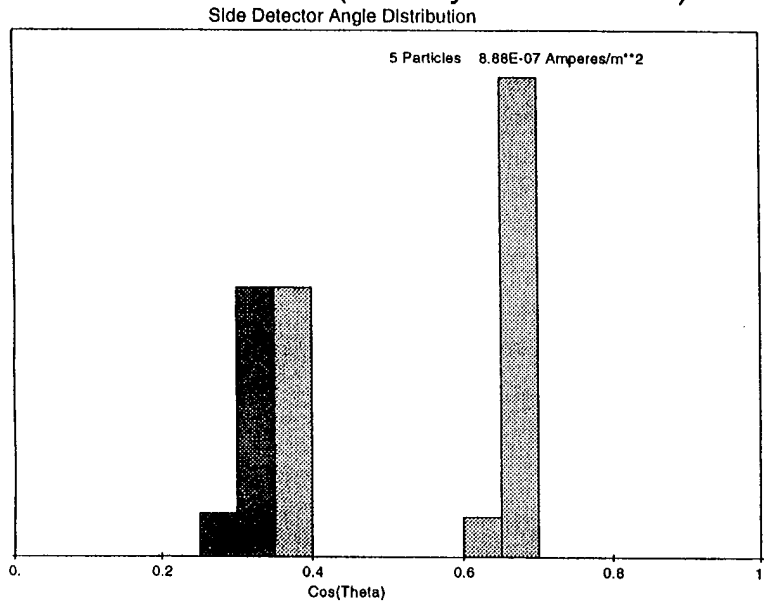

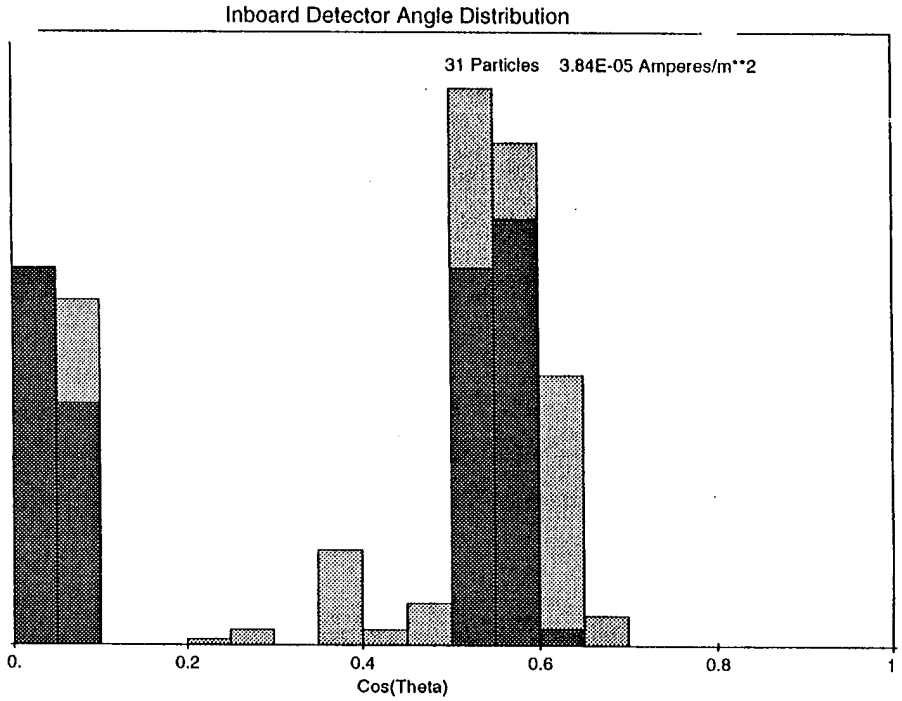

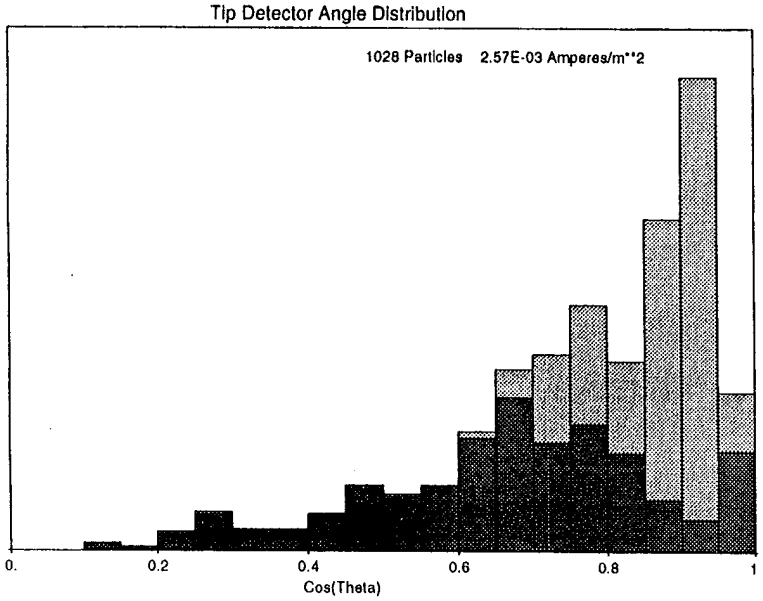

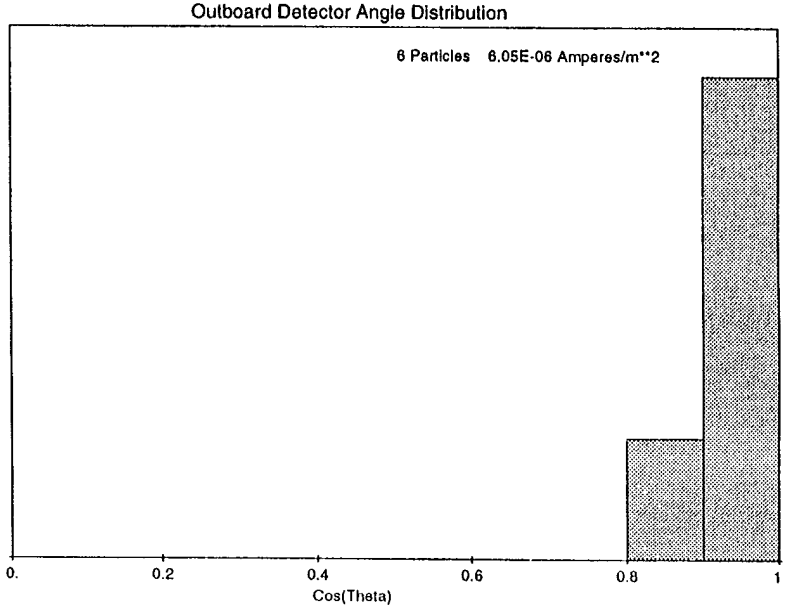

Run Code 7 15 deg. tilt

2000 Volts Bias <J> = 7.9x10−4

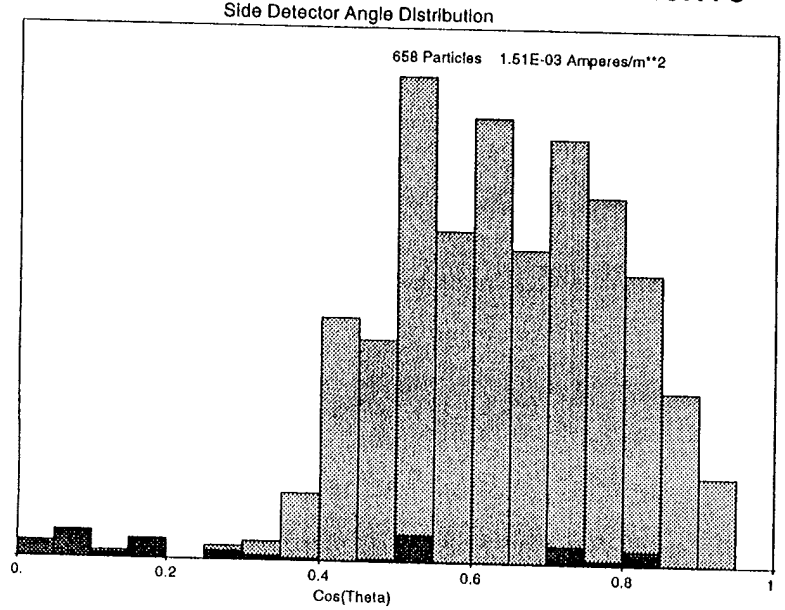

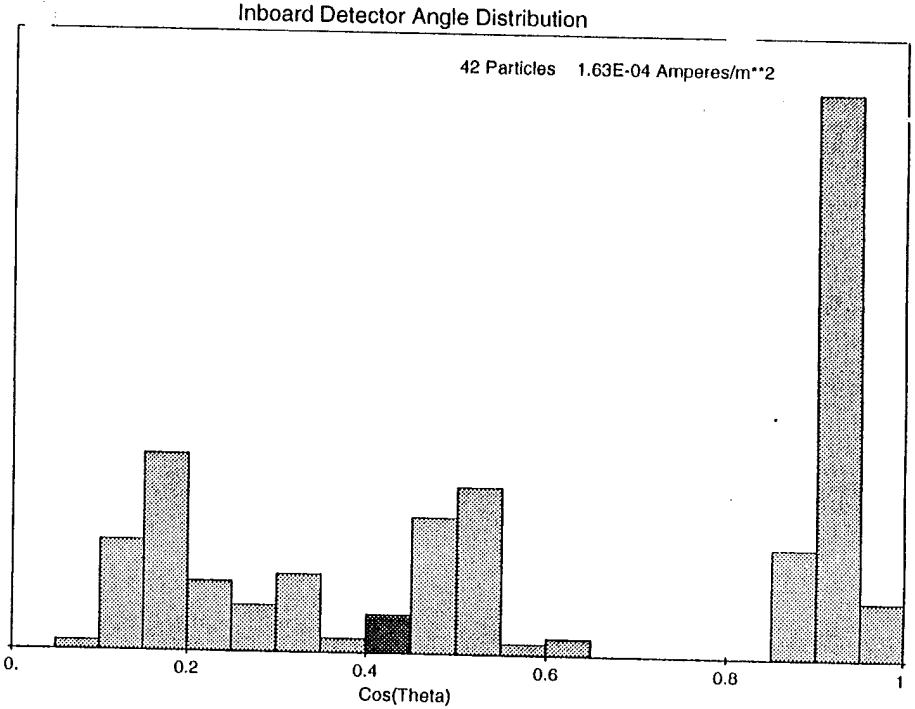

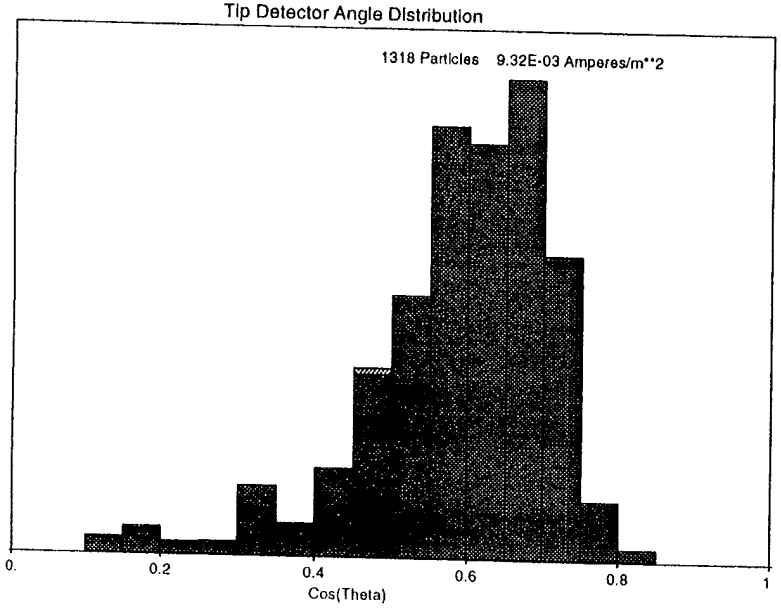

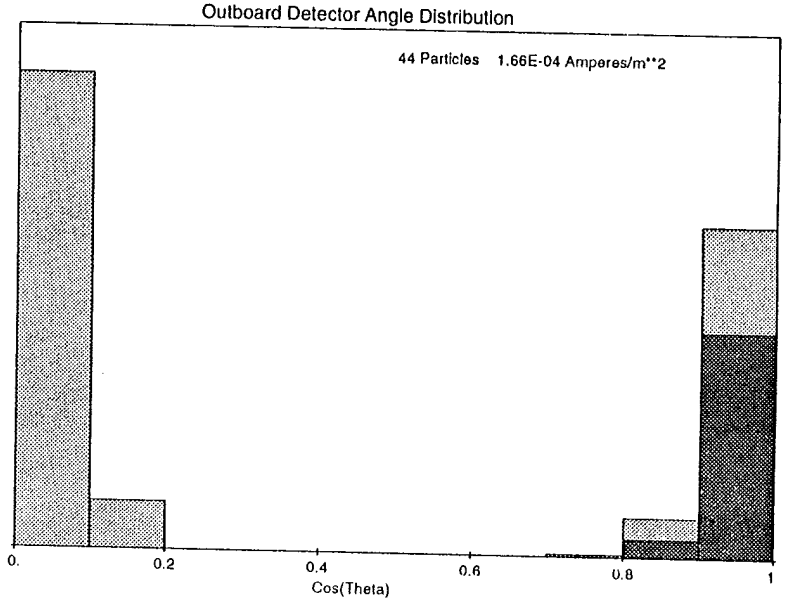

Run Co( ) 10
2000 Volts Bias

<J> =7.0x10−4

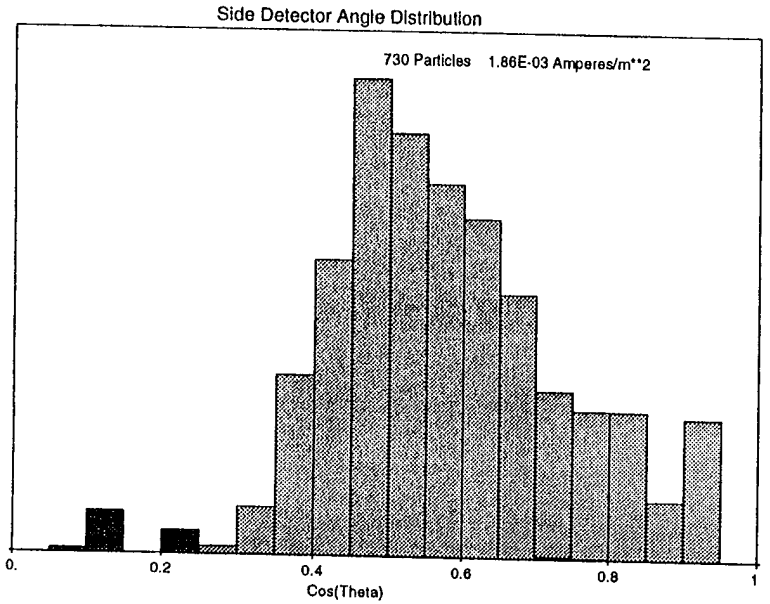

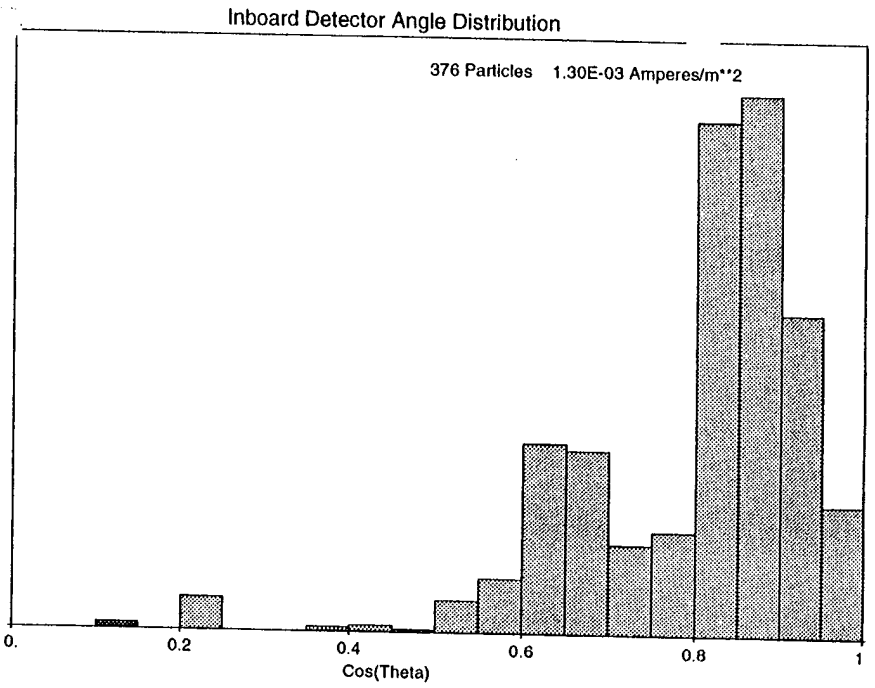

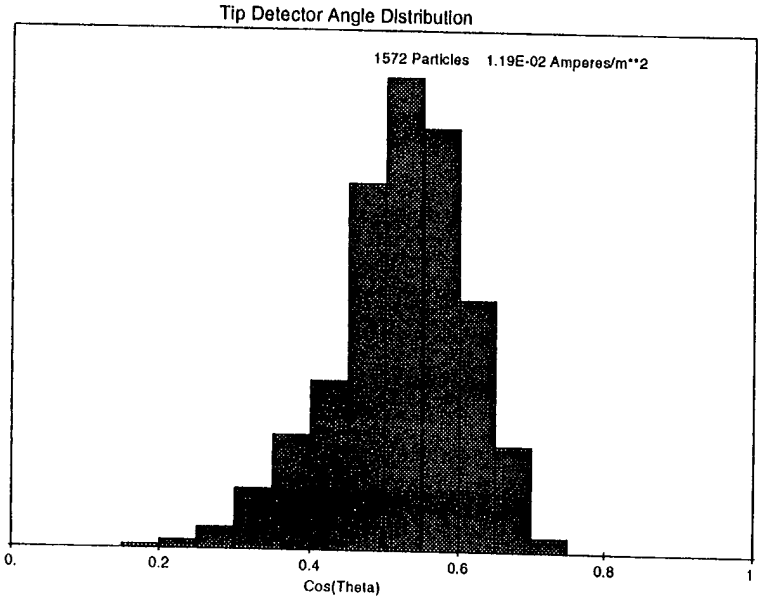

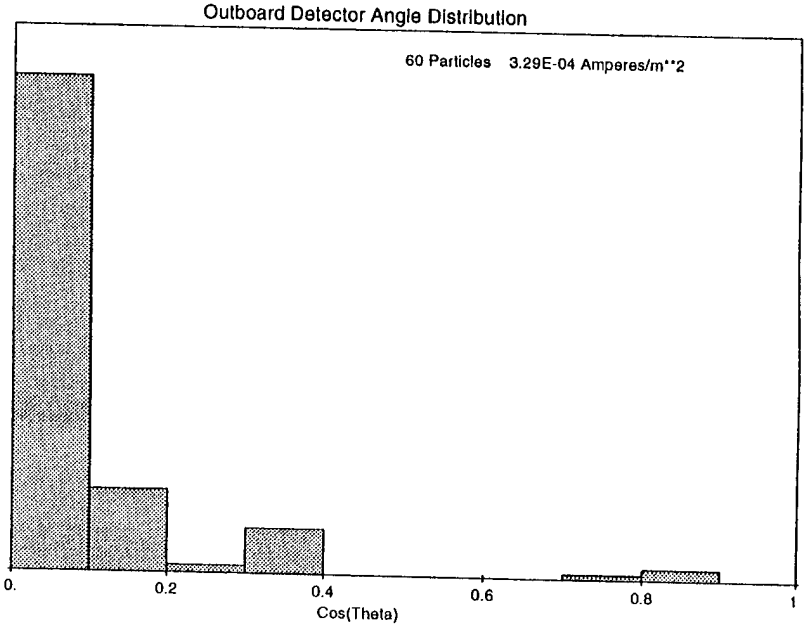

Run Co..e 11 −15 deg. Tilt

2000 Volts Bias <J> = 6.4x10−4

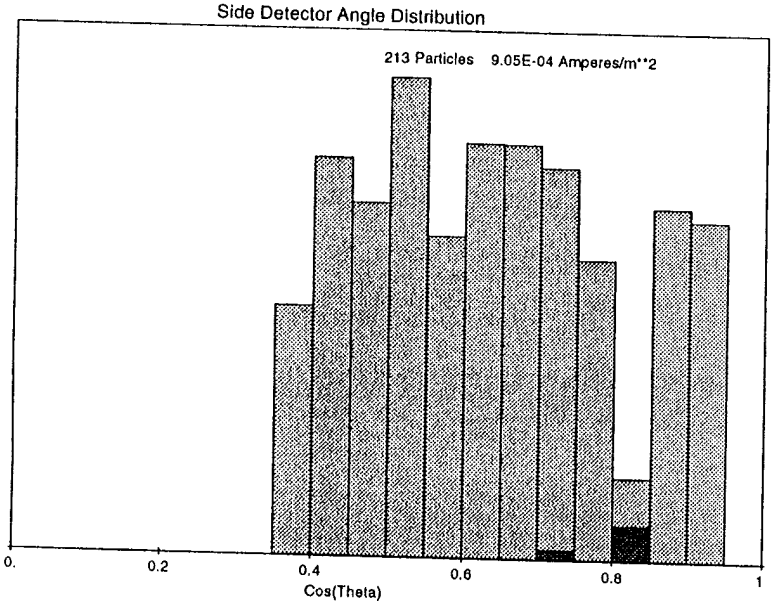

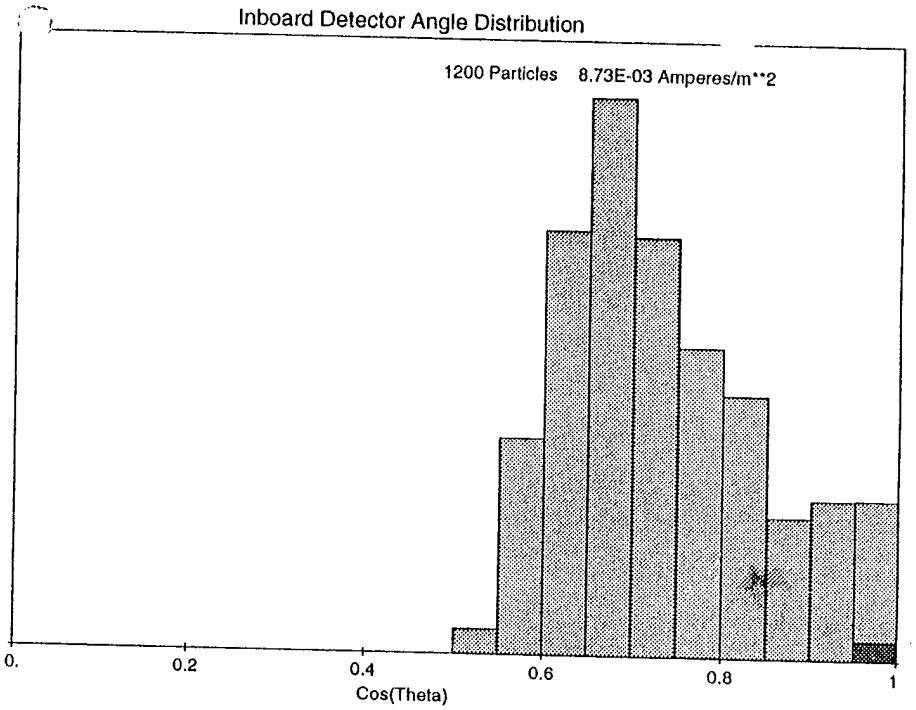

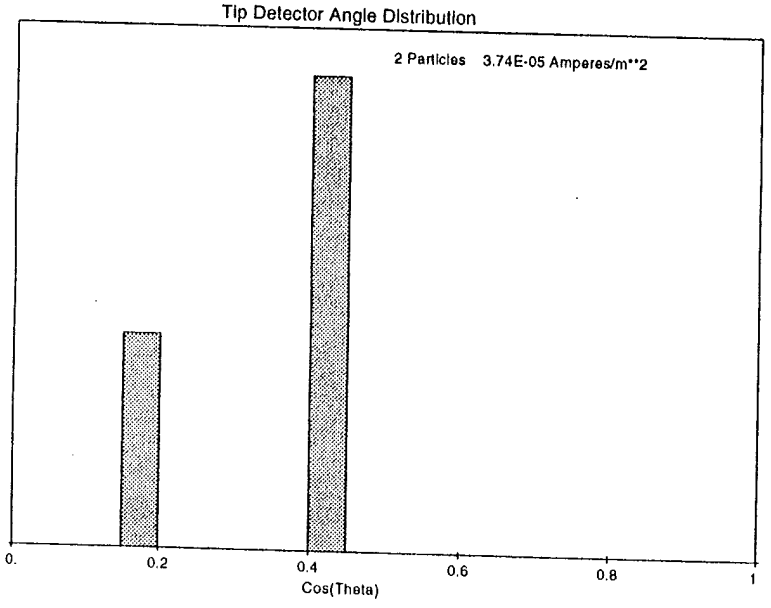

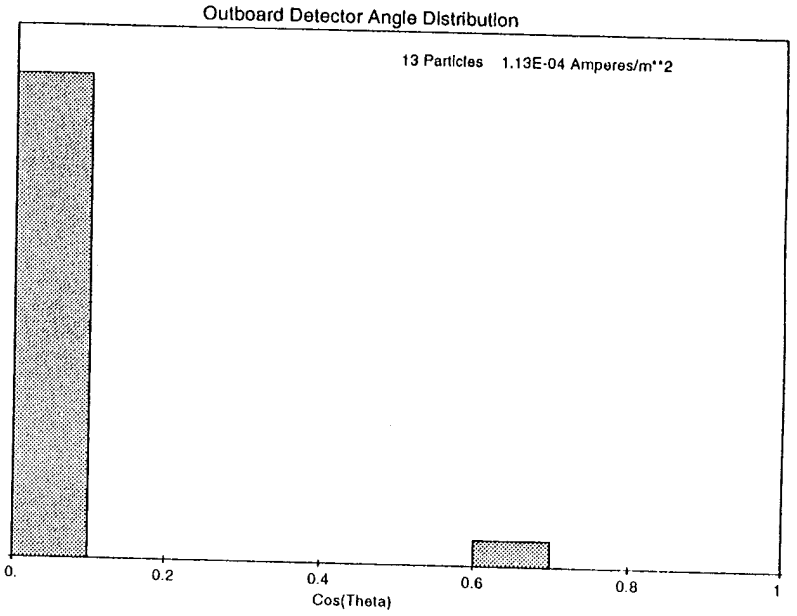

Run C de 12

1500 Volt Bias

<J> = 5.3x10−4

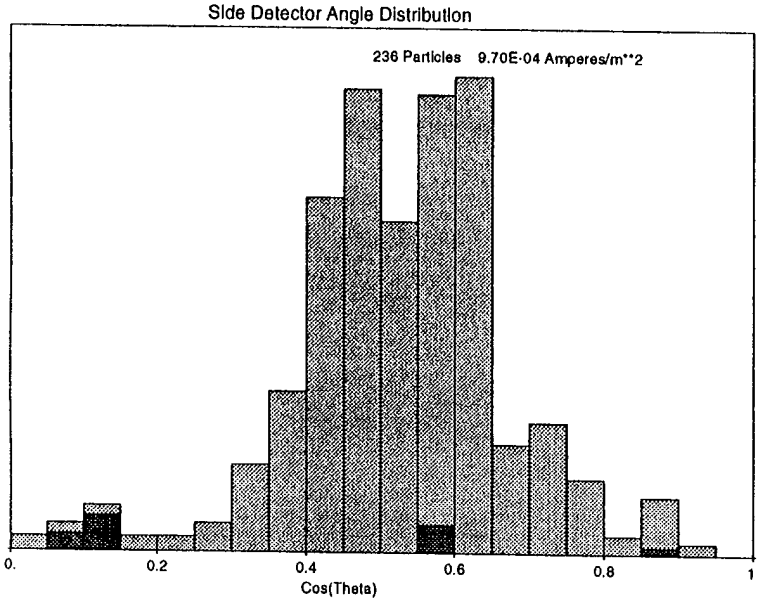

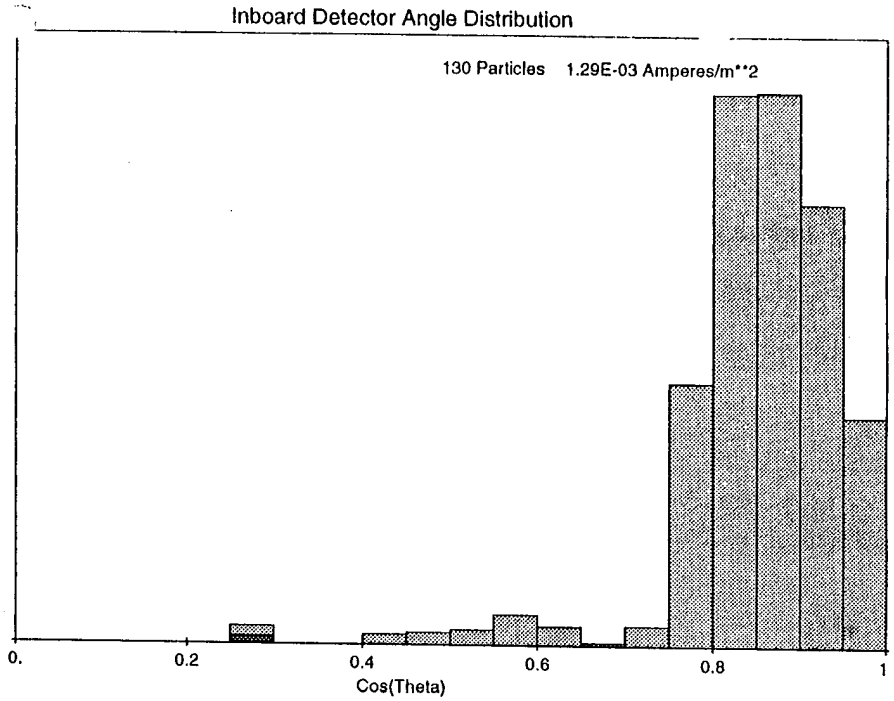

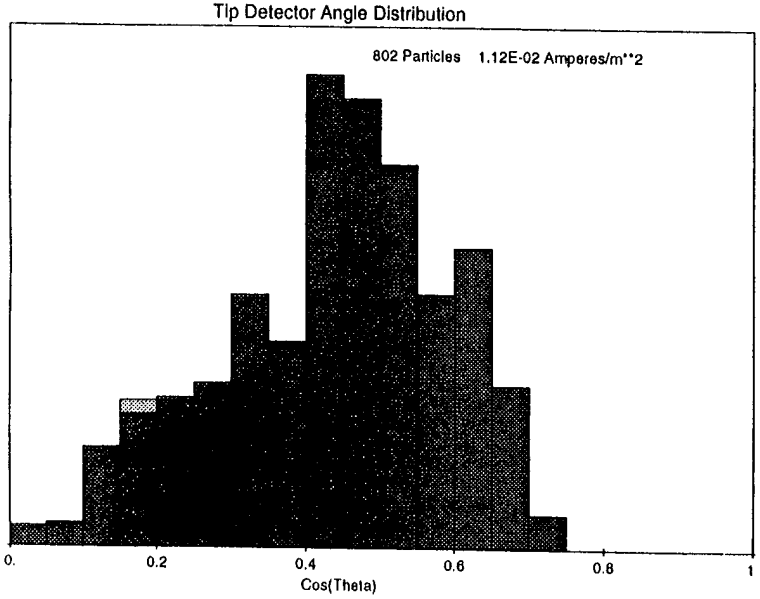

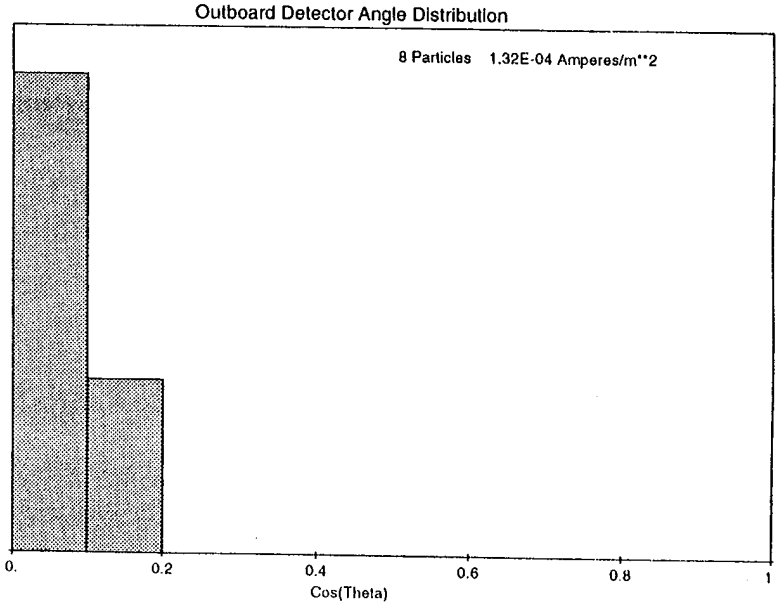

Run Co[illegible] 14

1000 Volts Bias

<J> = 3.2x10−4

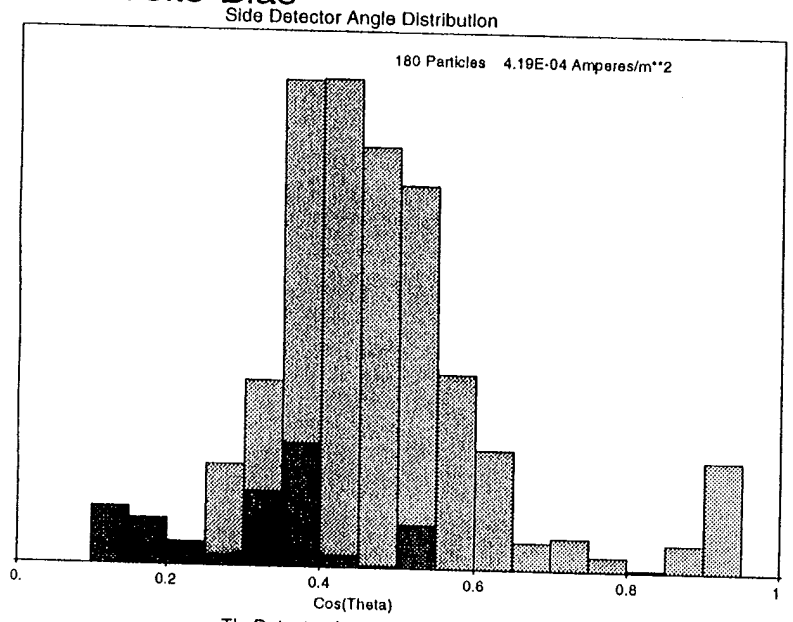

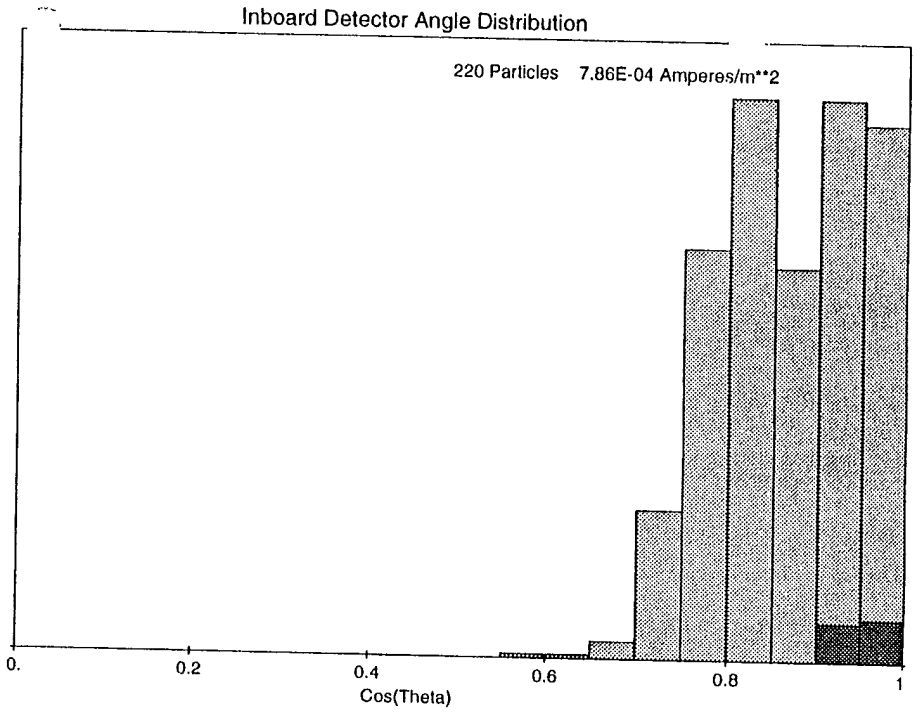

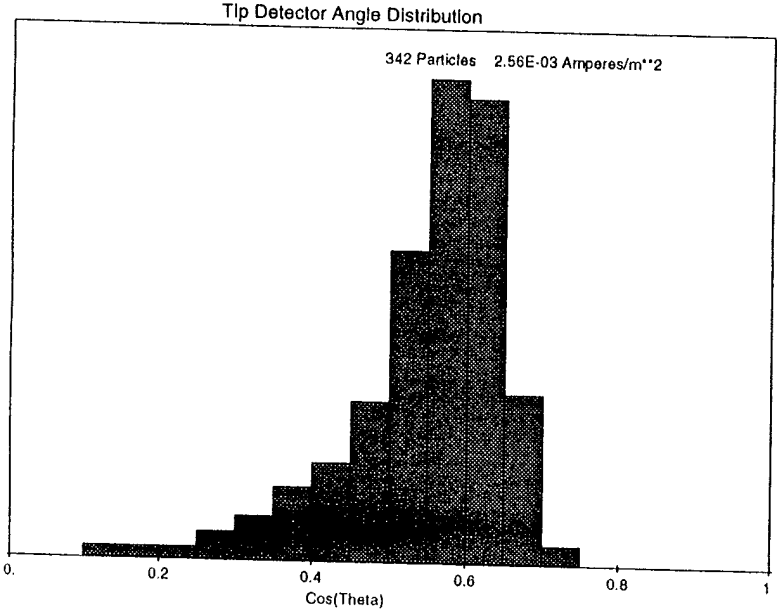

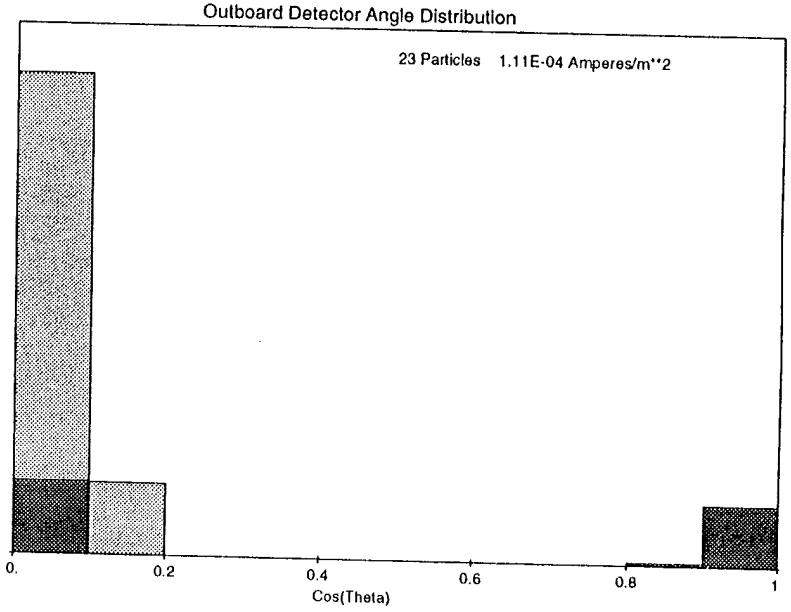

Run Co( ) 16
500 Volt Bias

<J> = 1.3x10−4

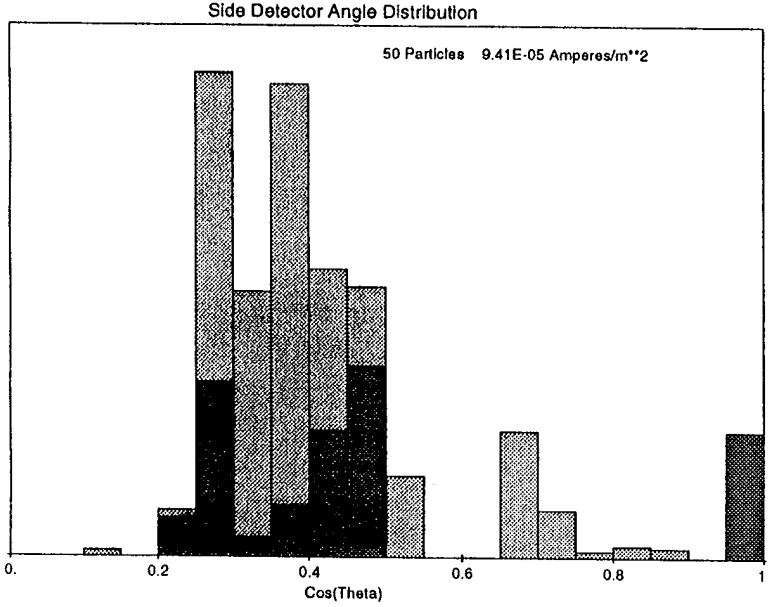

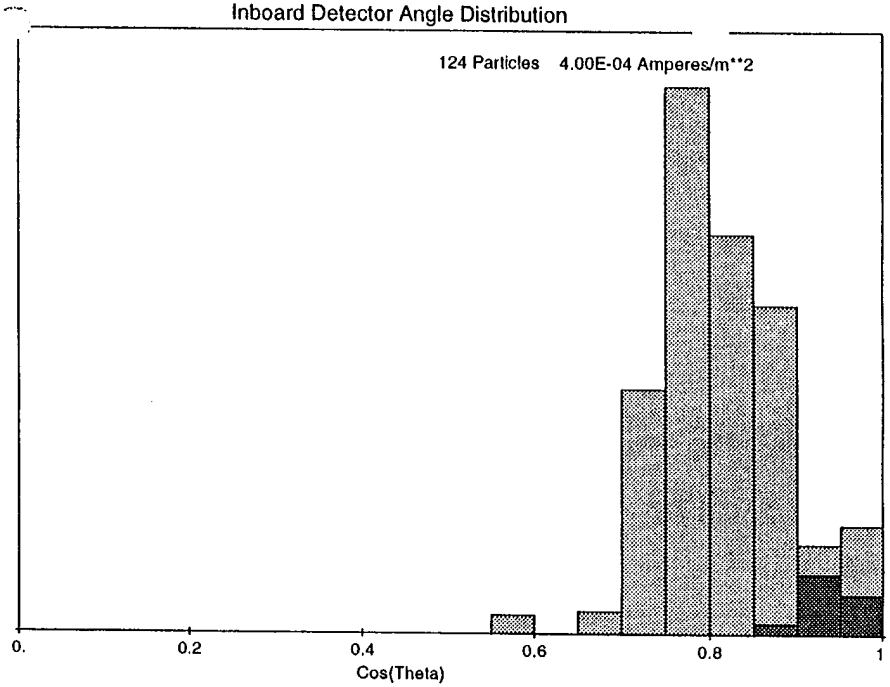

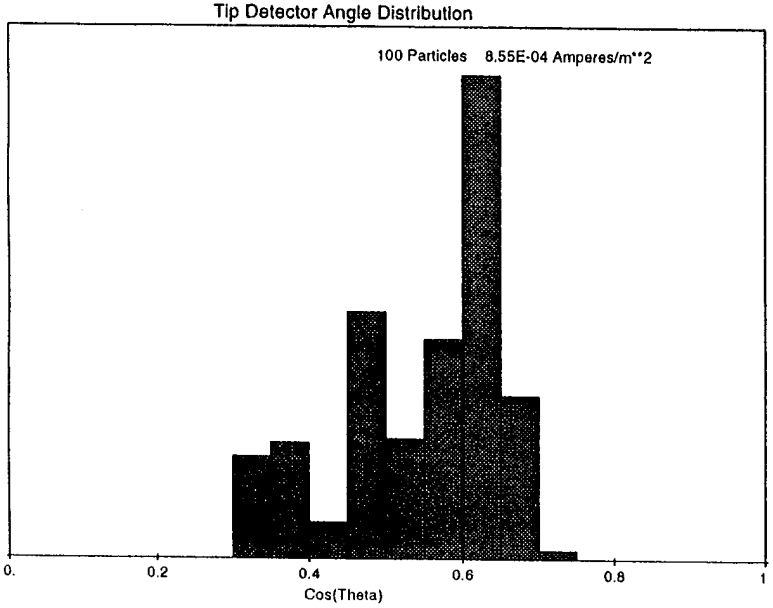

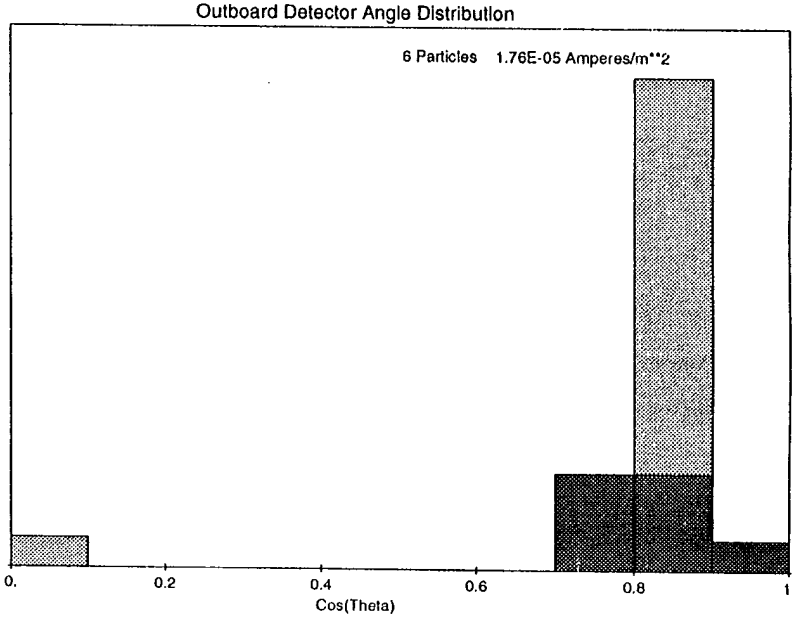

Run Co( ) 19 N = 5x1011 <J> = 4.8x10−5

200 Volts Bias

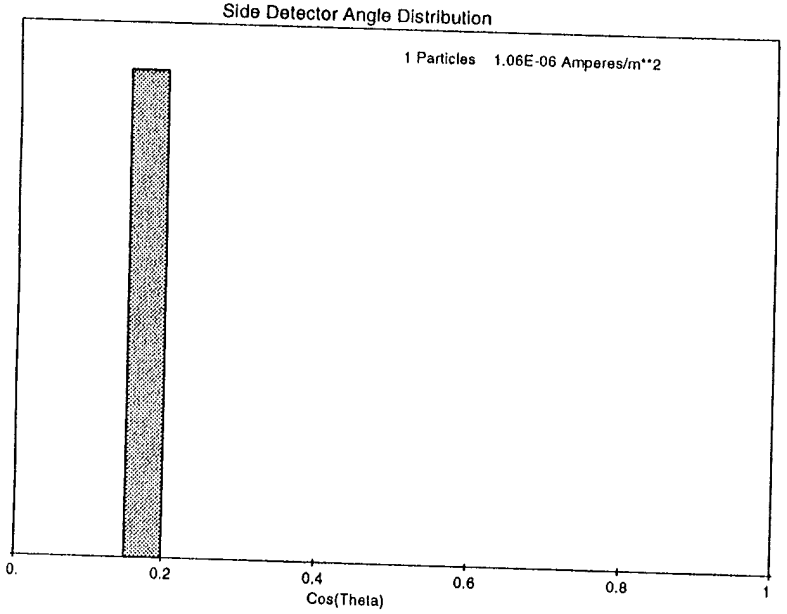

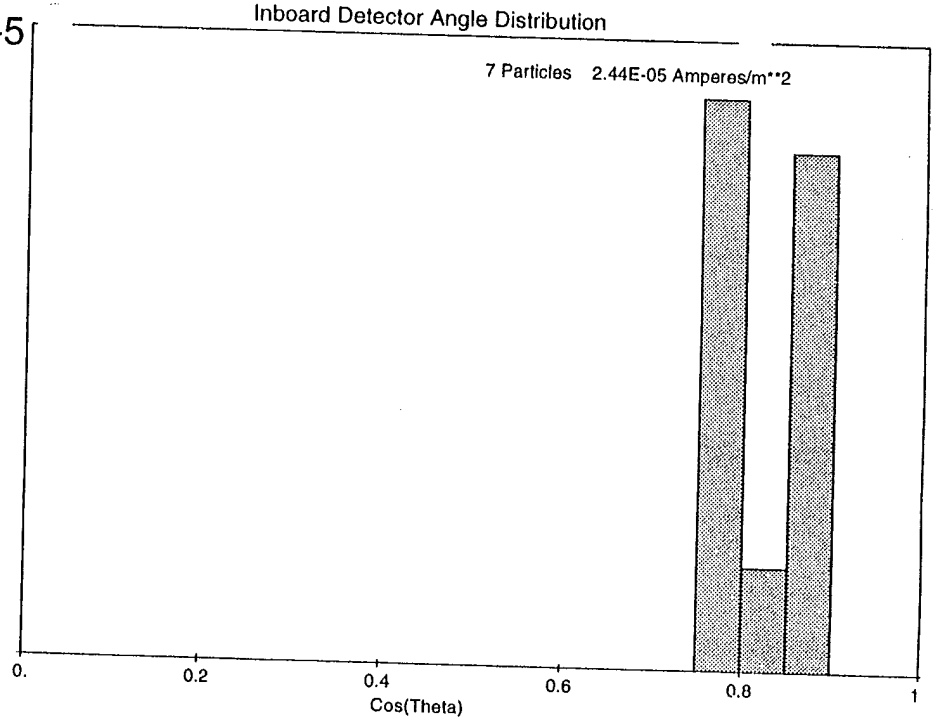

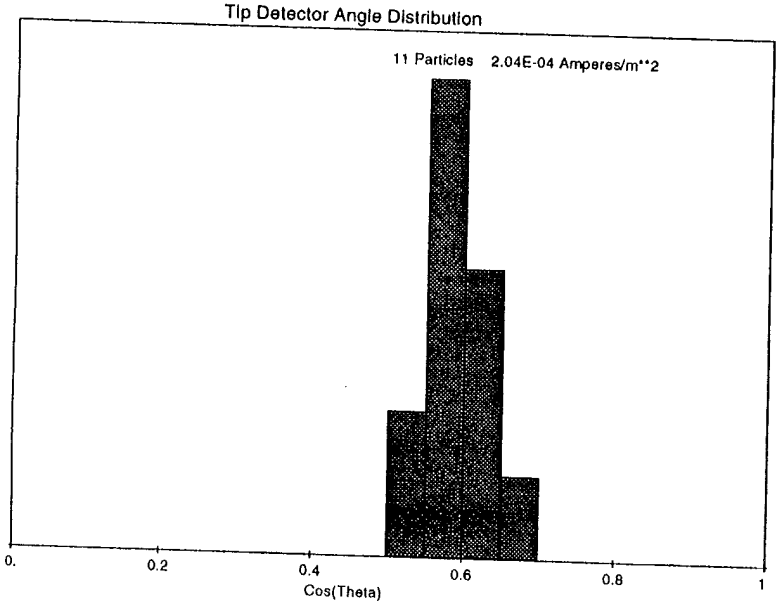

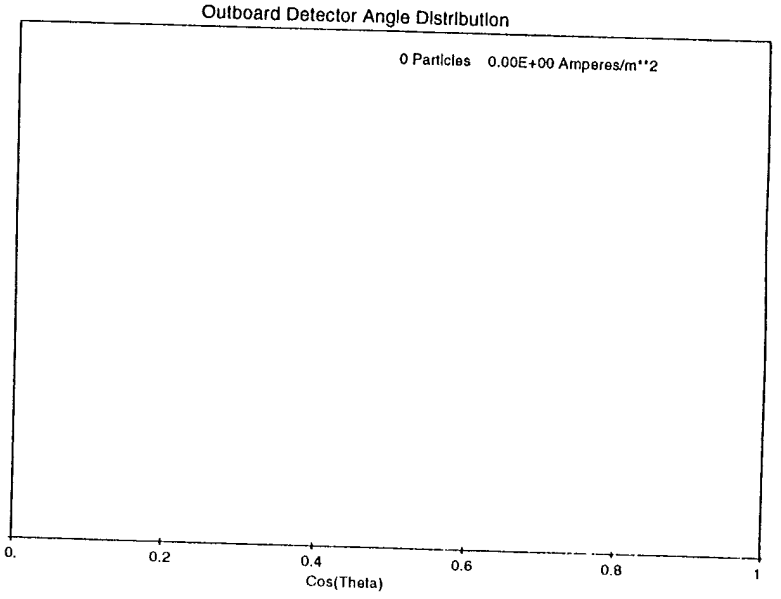

Run Code 20
200 Volts Bias

$N = 2x10^{11}$ $\langle J \rangle = 4.3x10^{-5}$

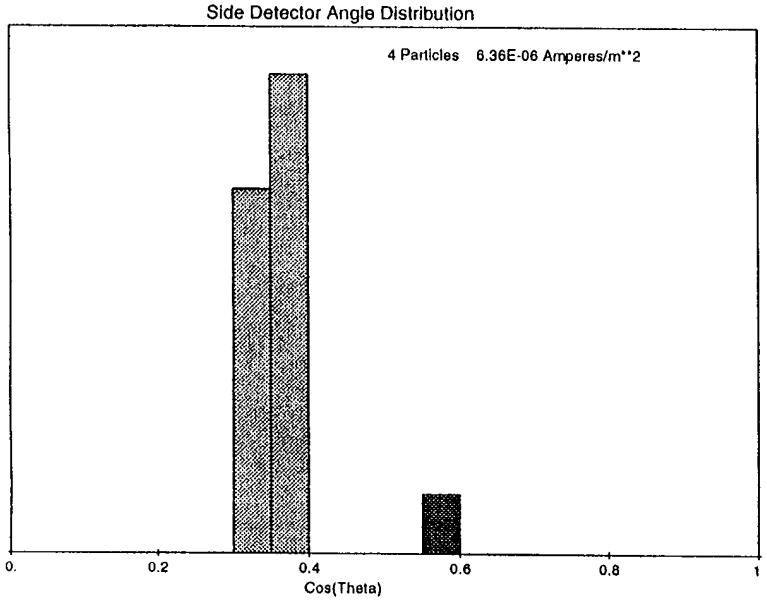

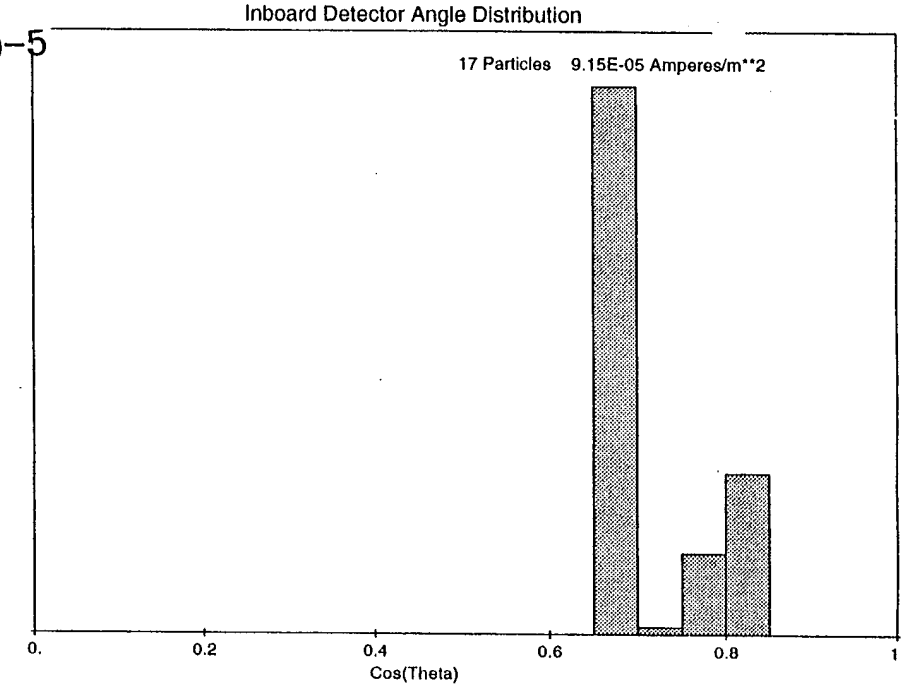

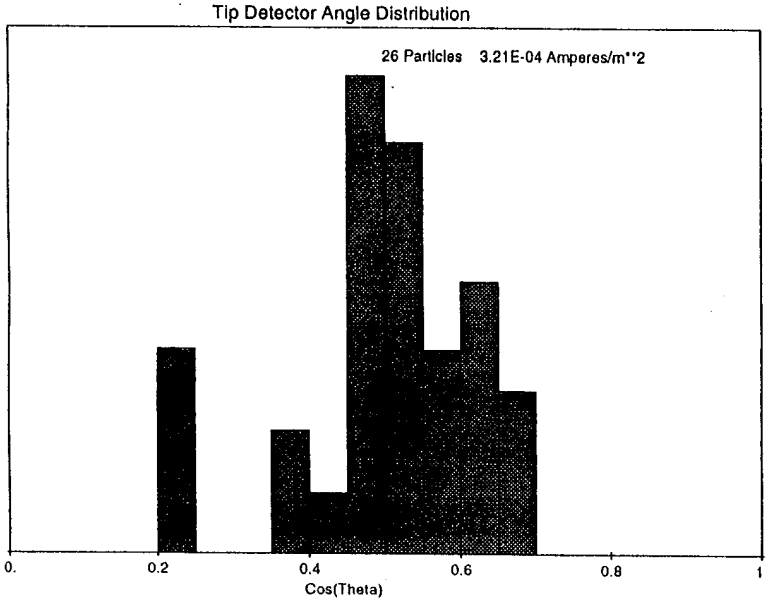

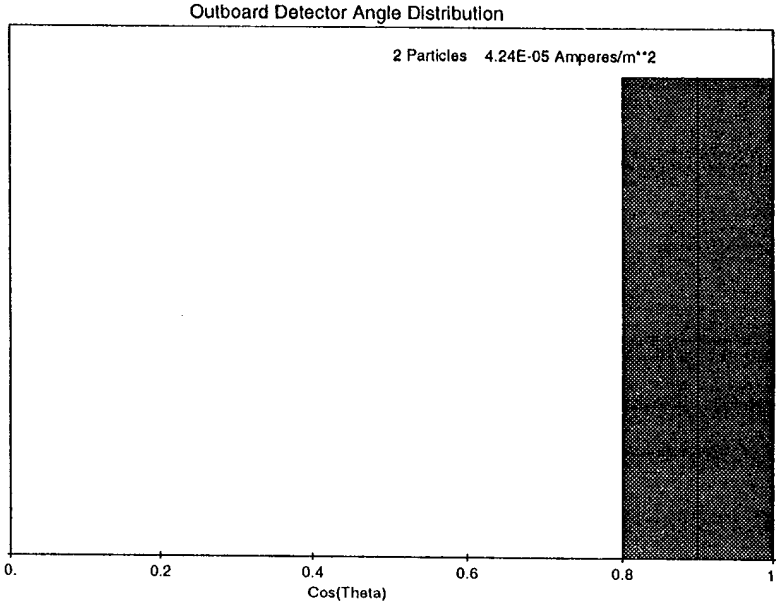

Run Co › 22

200 V Bias

<J> = 3.4x10−5

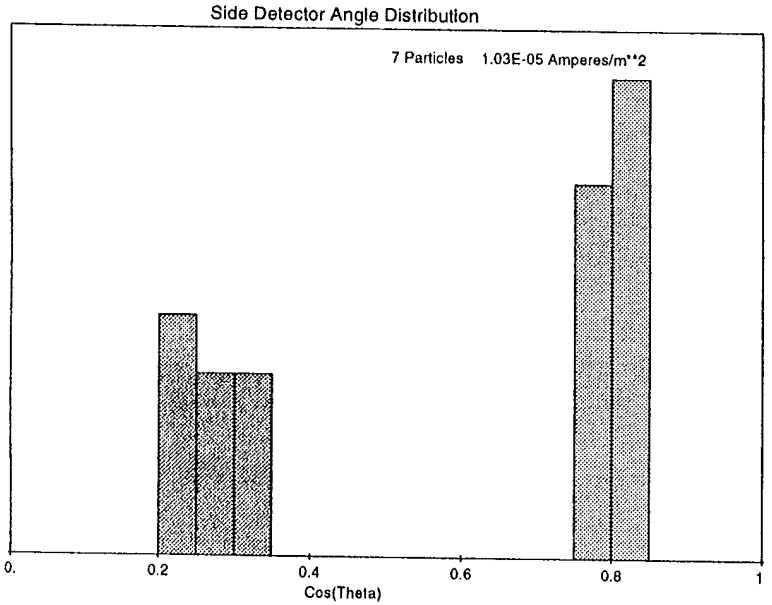

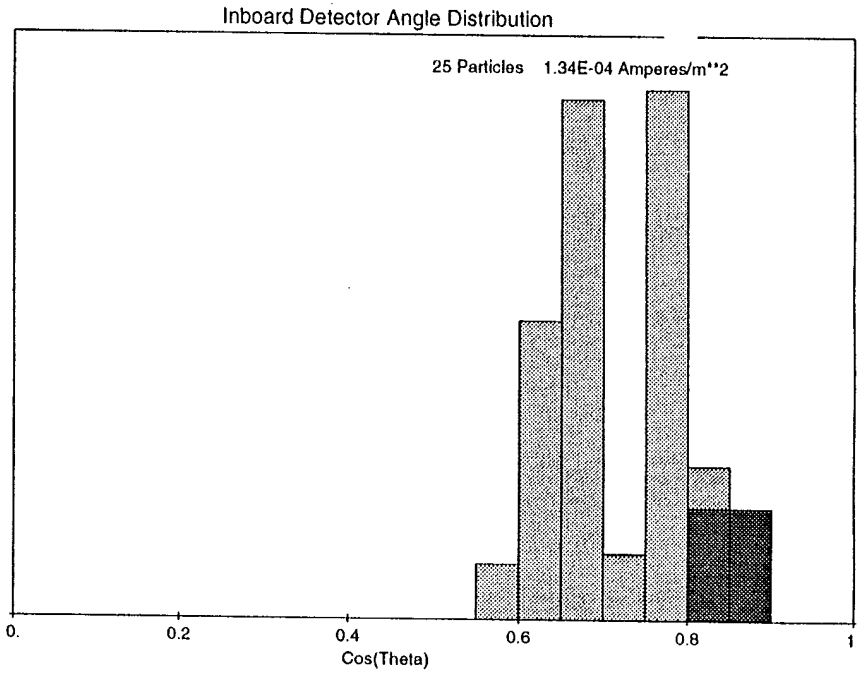

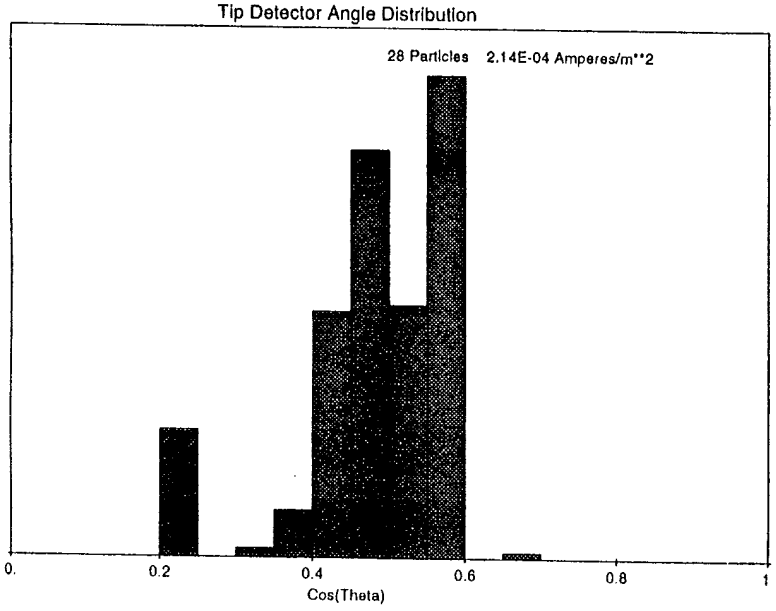

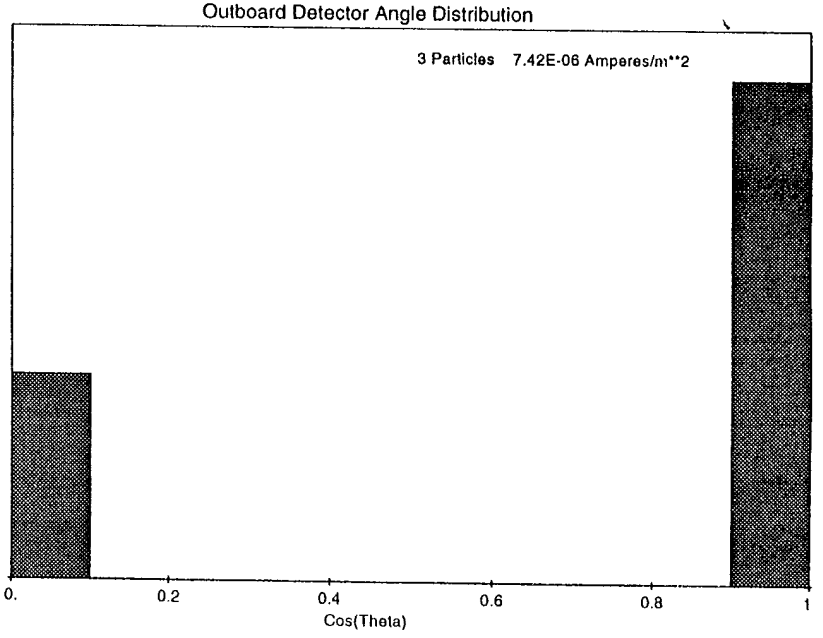

Run Co:) 24 40 deg. tilt <J> = 7.4x10−

100 V Bias 10% H (O distribution)

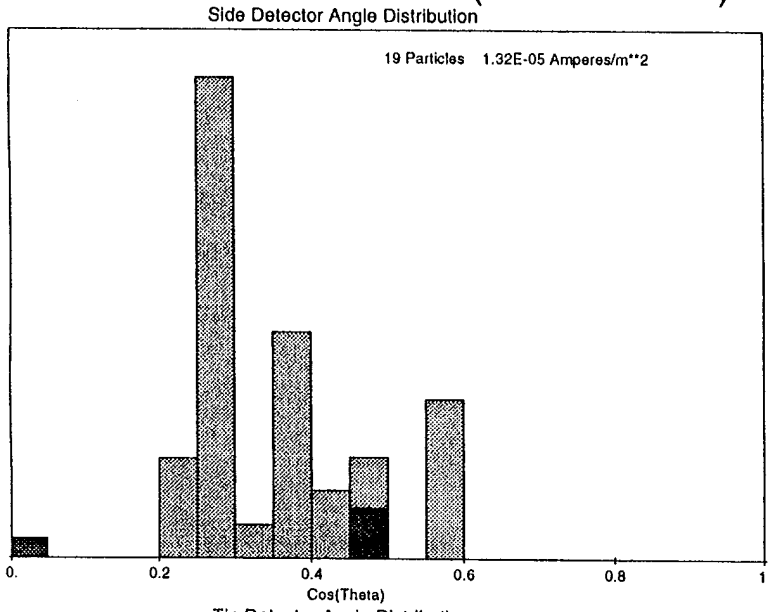

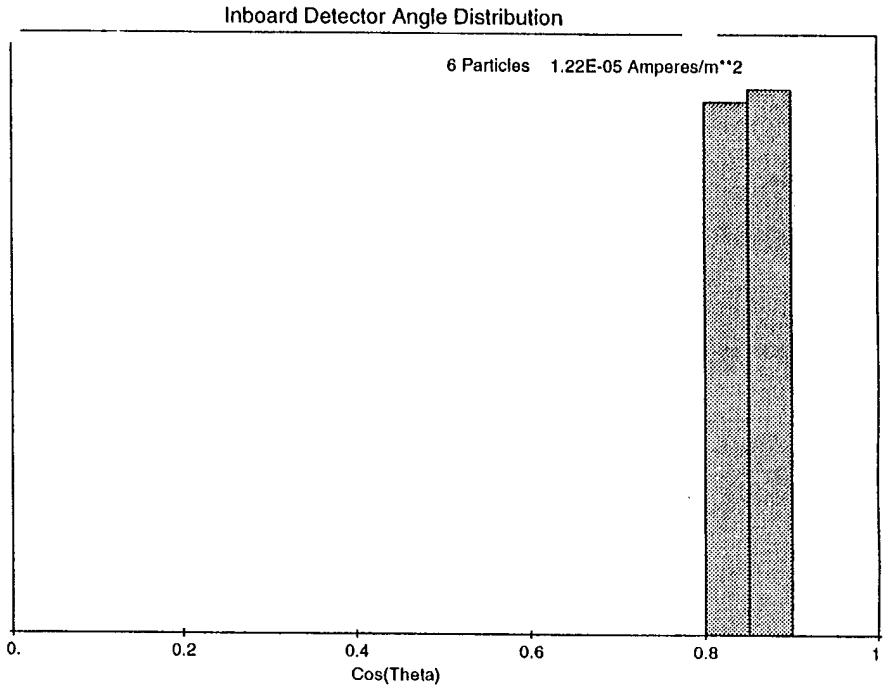

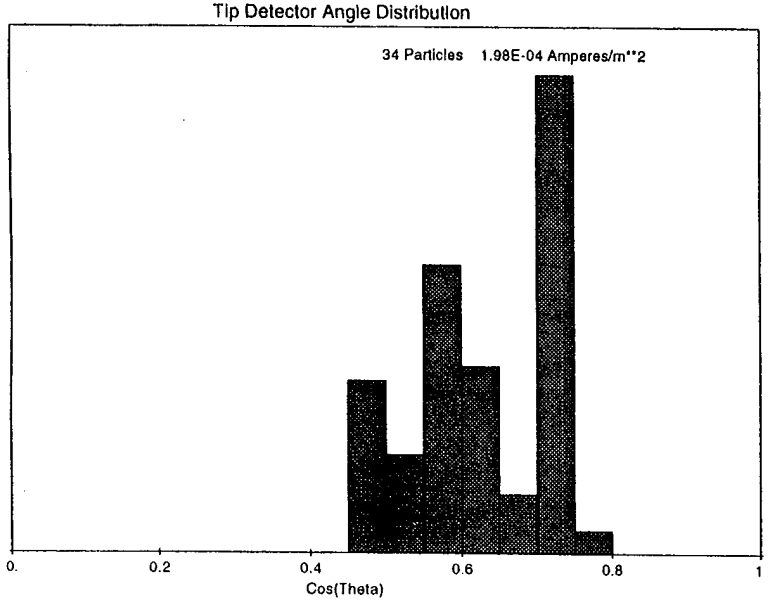

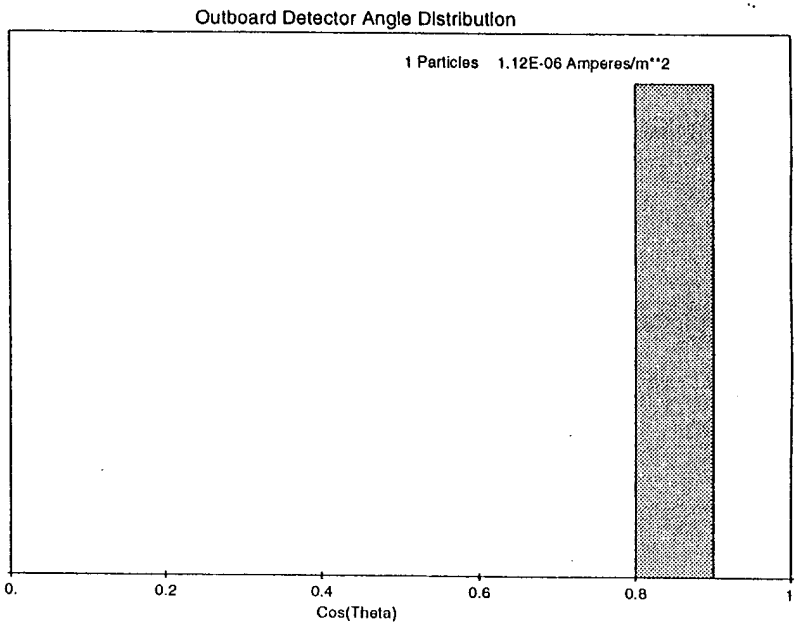

Run Co.. 24 40 deg. tilt <J> = 7.4x10⁻

100 V Bias 10% H (H distribution)

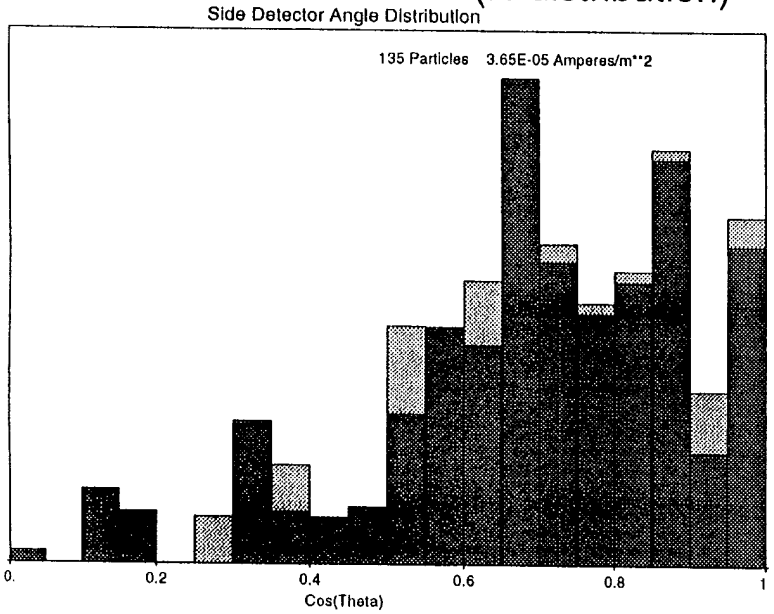

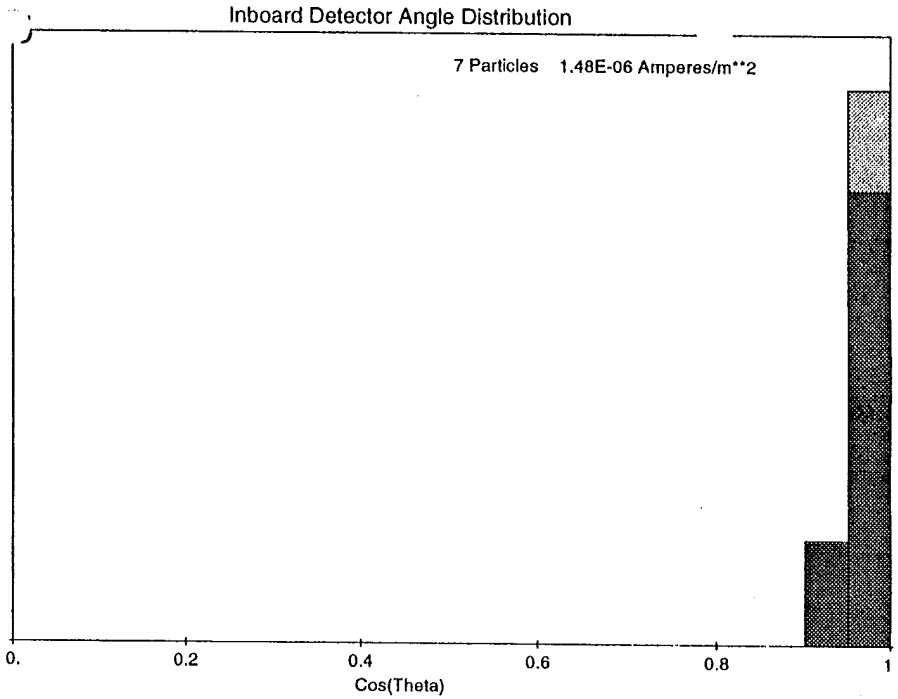

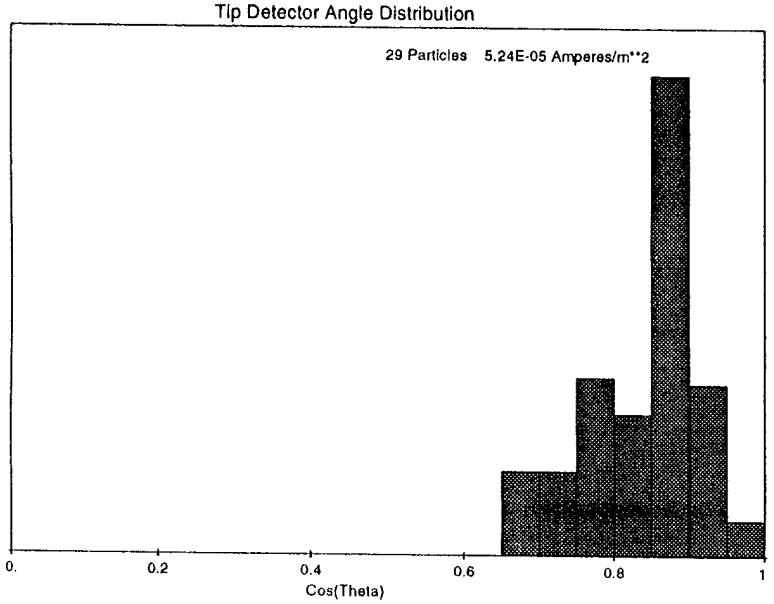

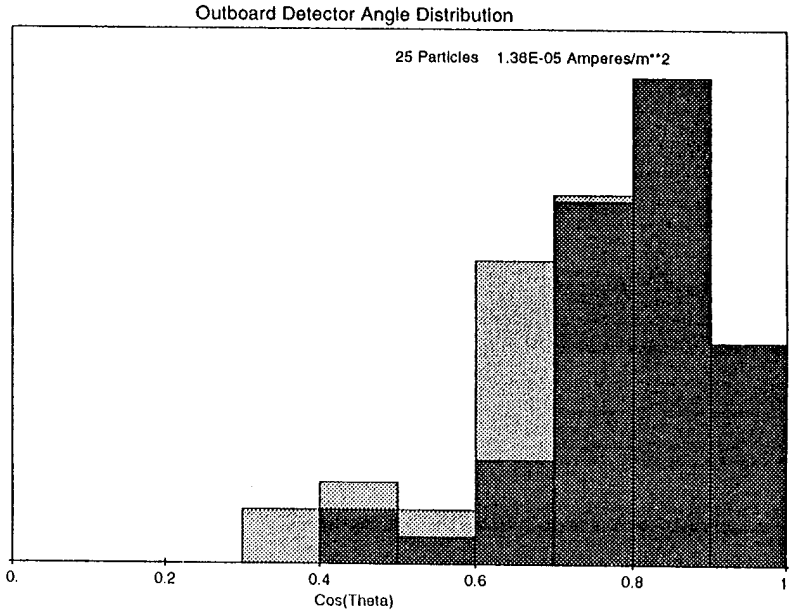

Run Co..e 25
100 V Bias

40 deg. tilt <J> = 5.6x10−5

Side Detector Angle Distribution

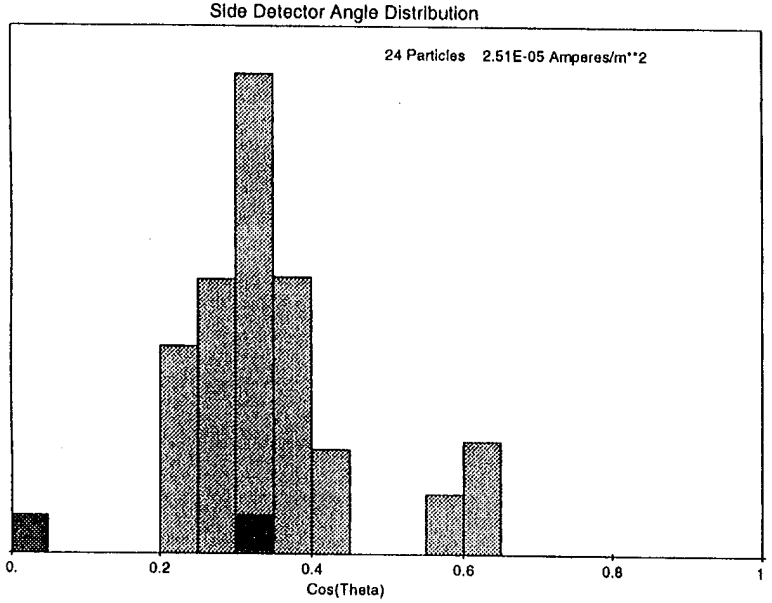

Inboard Detector Angle Distribution

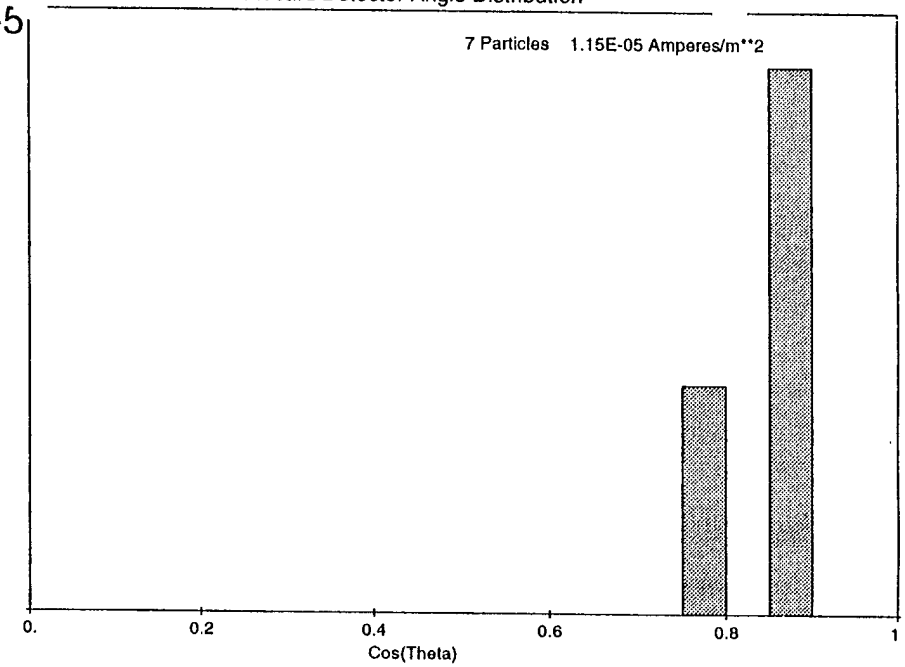

Tip Detector Angle Distribution

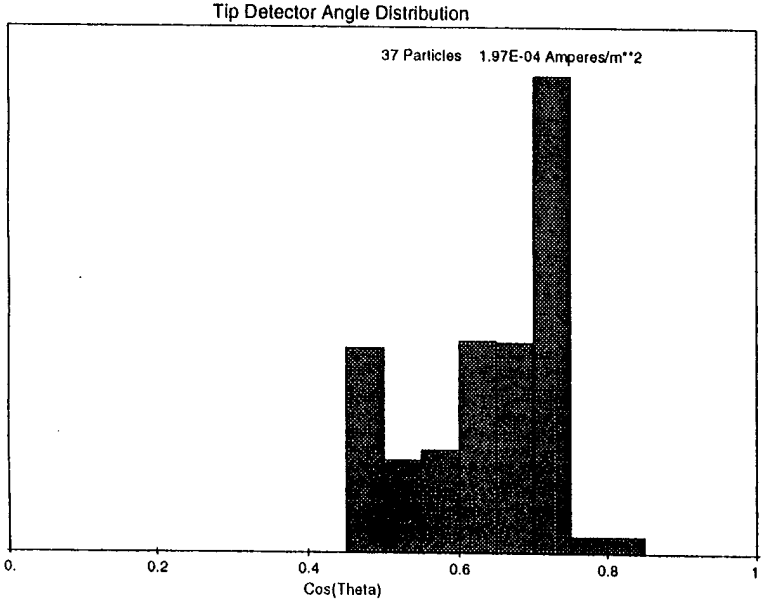

Outboard Detector Angle Distribution

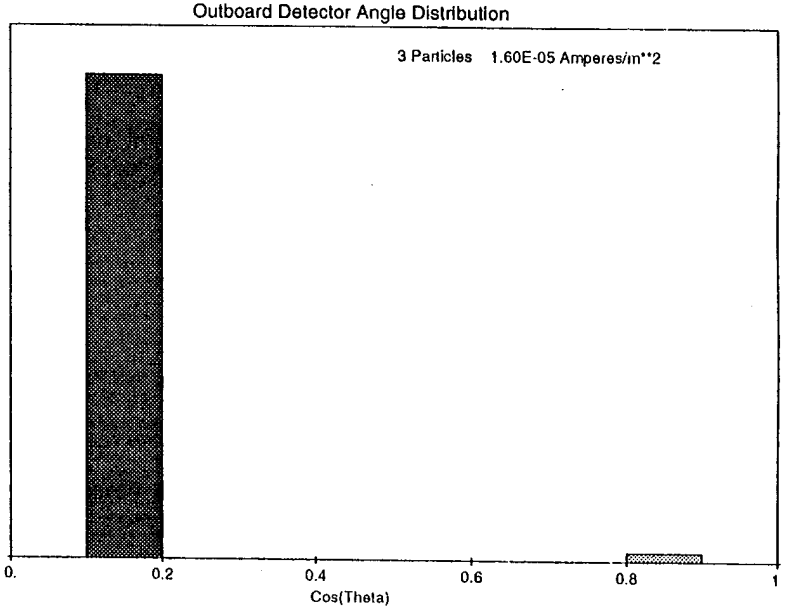

Run Co.. 26 40 deg. tilt <J> = 5.5x10−

100 V Bias −5 Volts on WSF

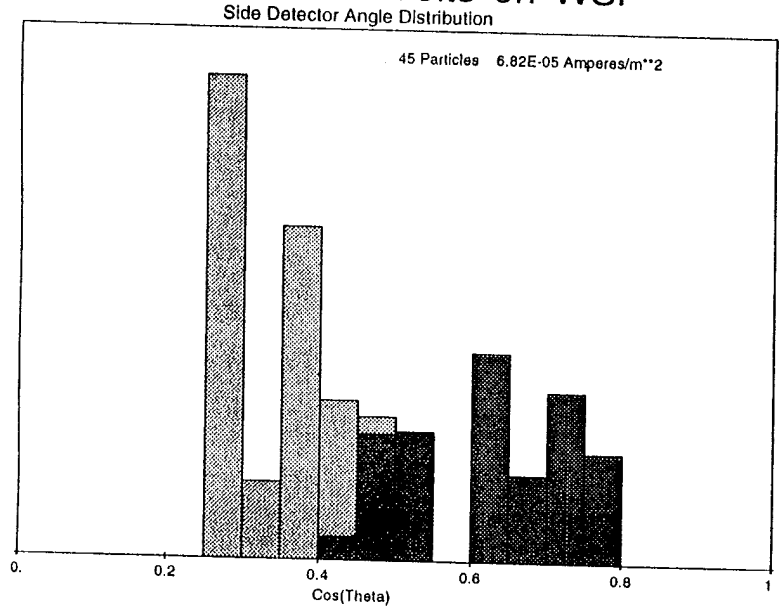

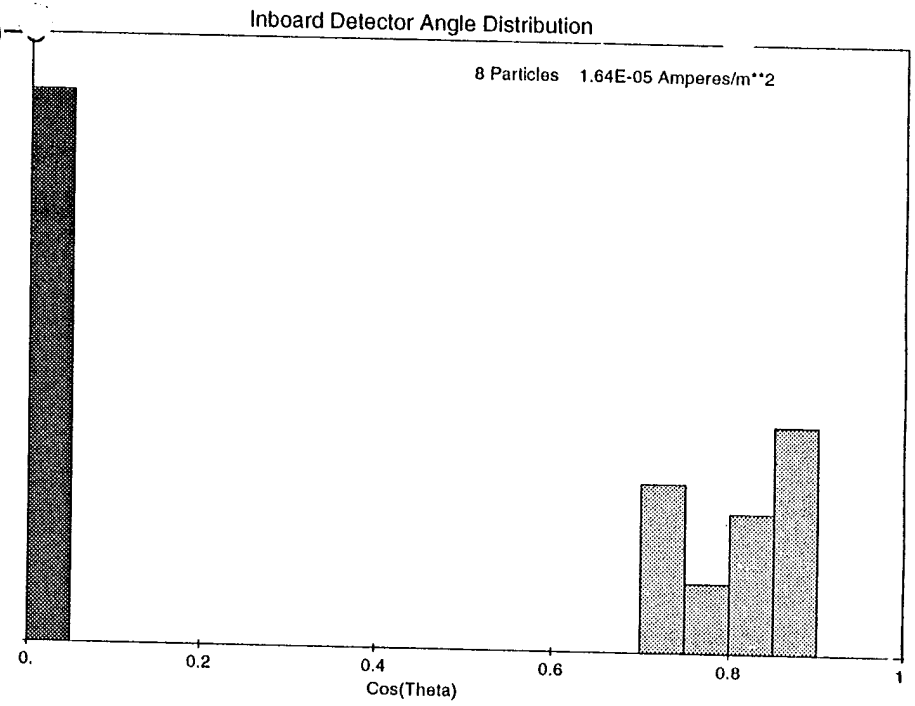

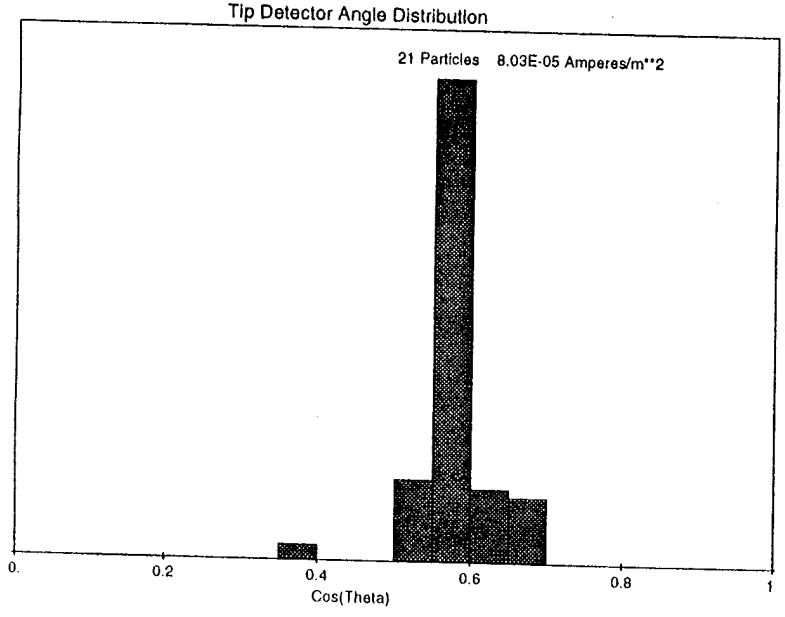

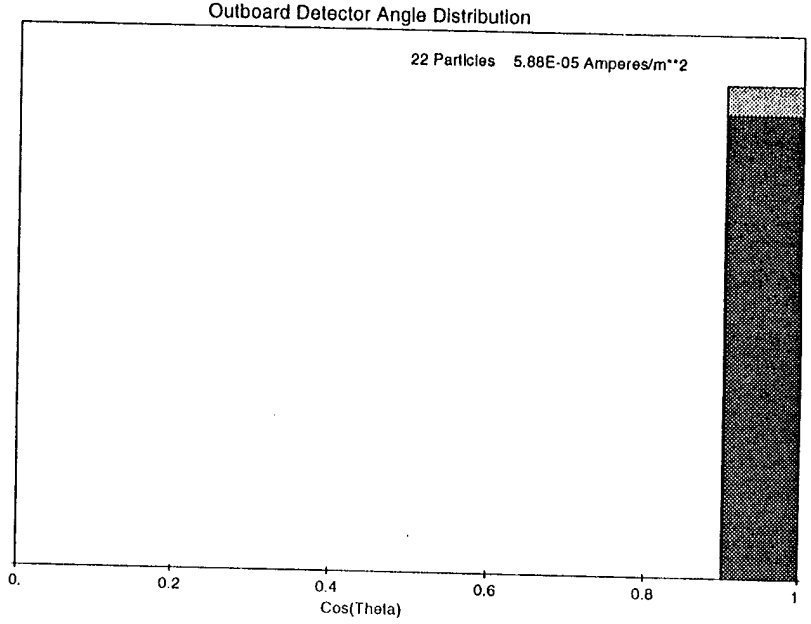

Run Co[illegible] 27 0 deg. tilt <J> = 3.8x10−5

100 V Bias 10% H (O distribution)

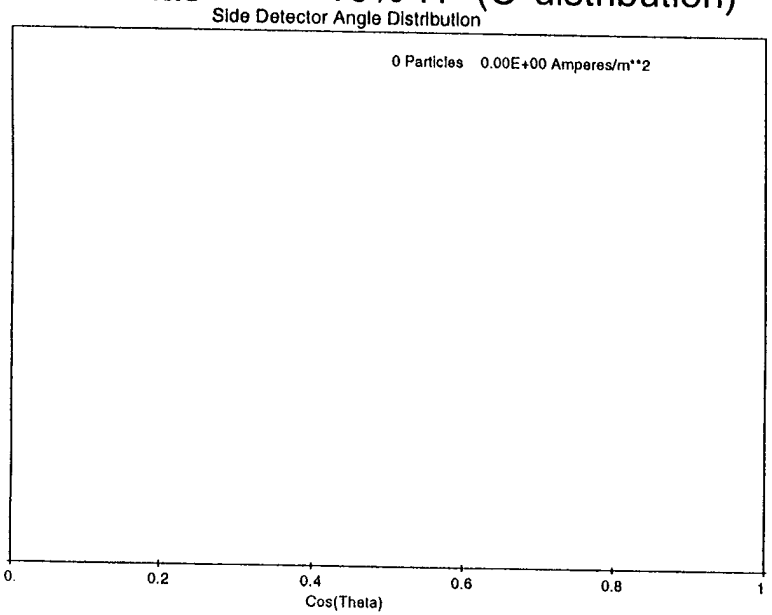

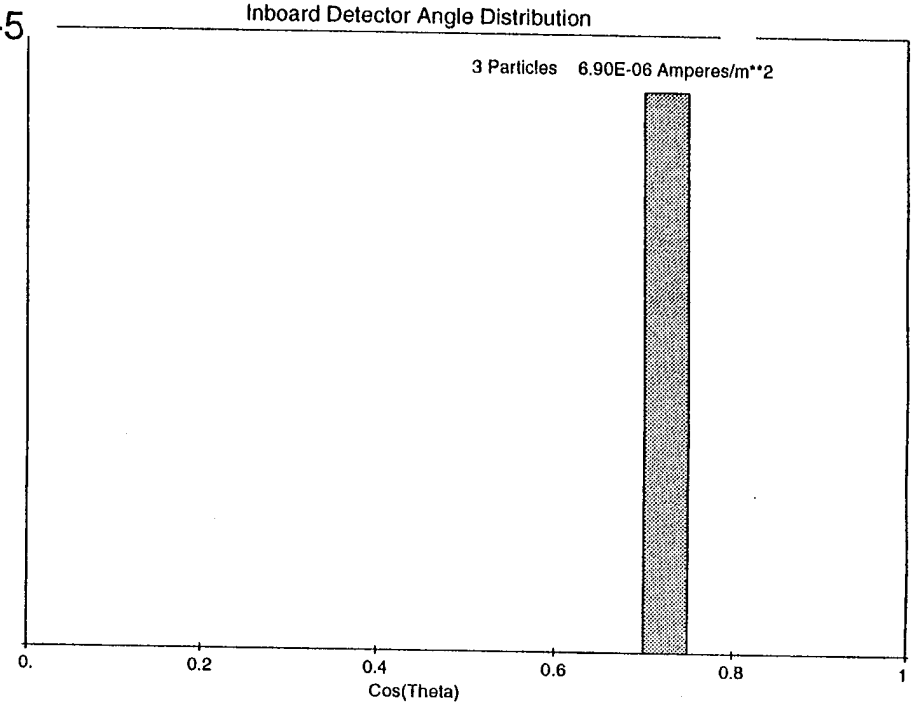

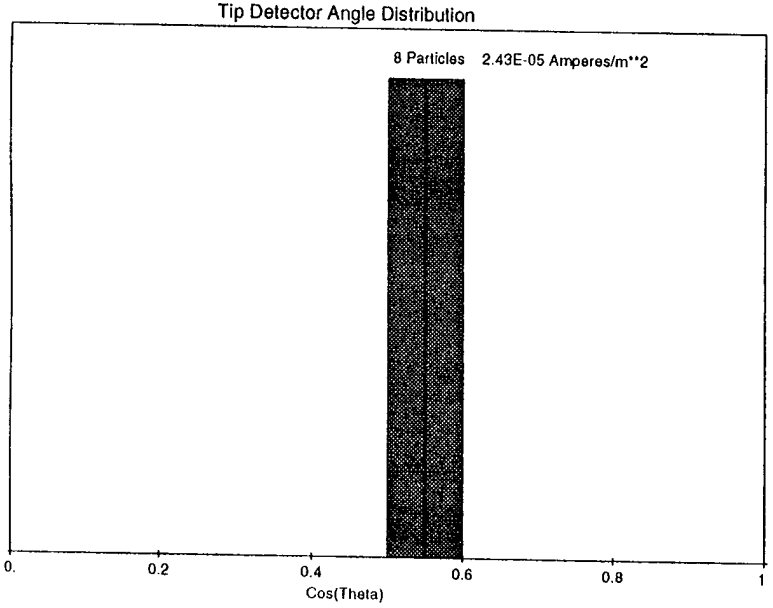

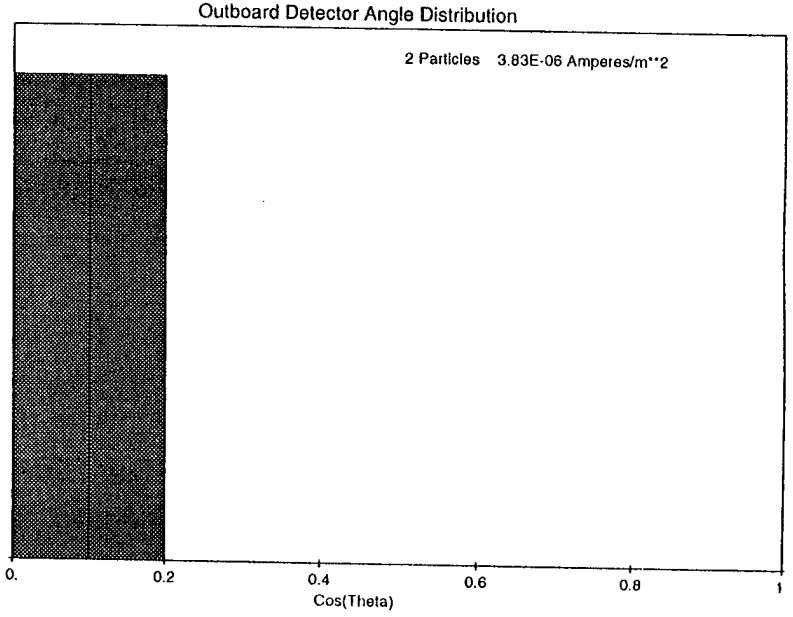

Run Co[illegible] 27 0 deg. tilt <J> = 3.8x1[illegible]-5

100 V Bias 10% H (H distribution)

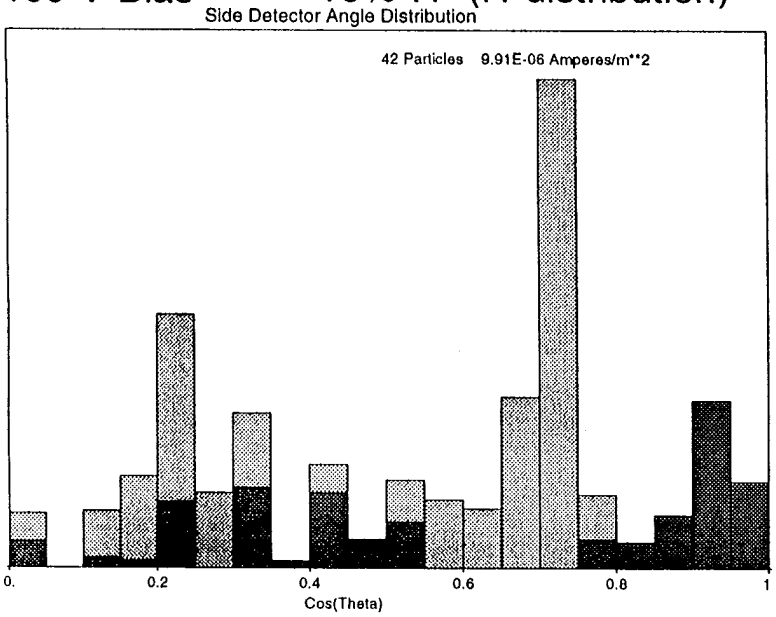

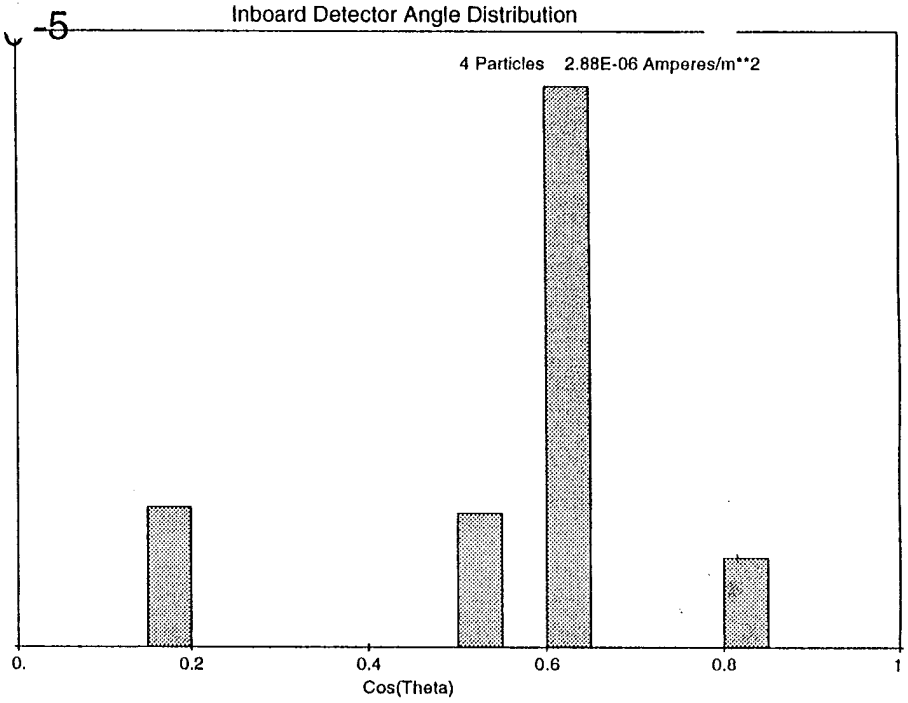

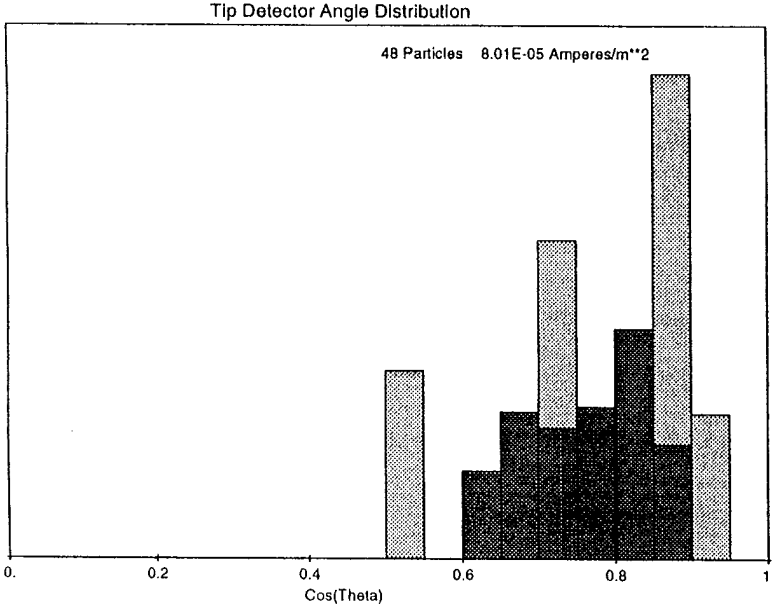

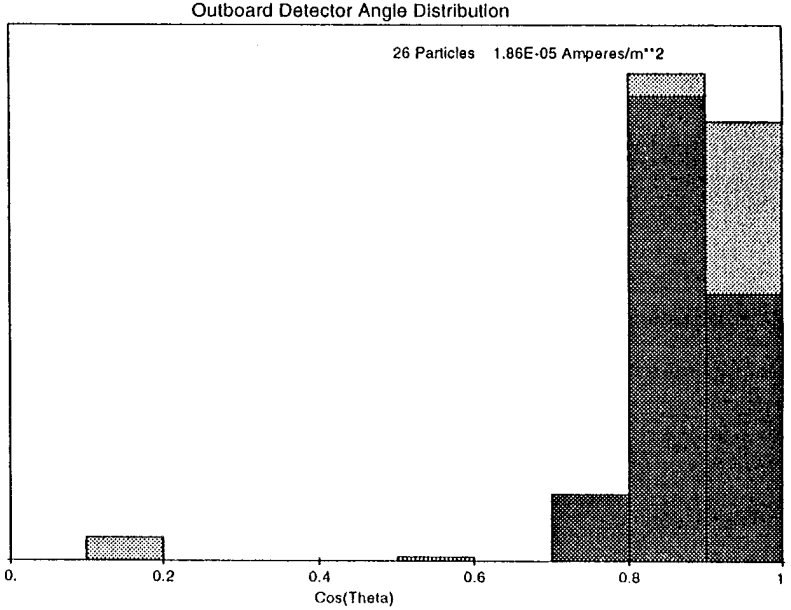

Run Cc ɜ 28 30 deg. tilt <J> = 3.5x10−5

100 Volts Bias

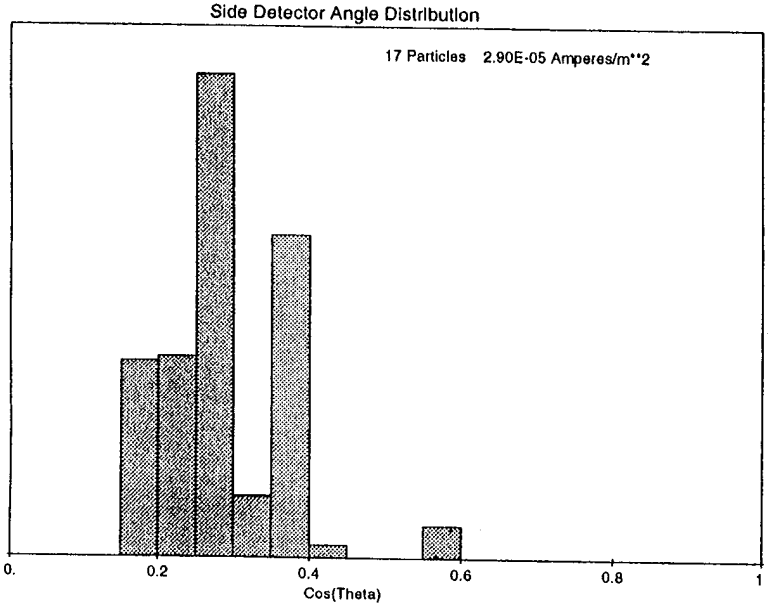

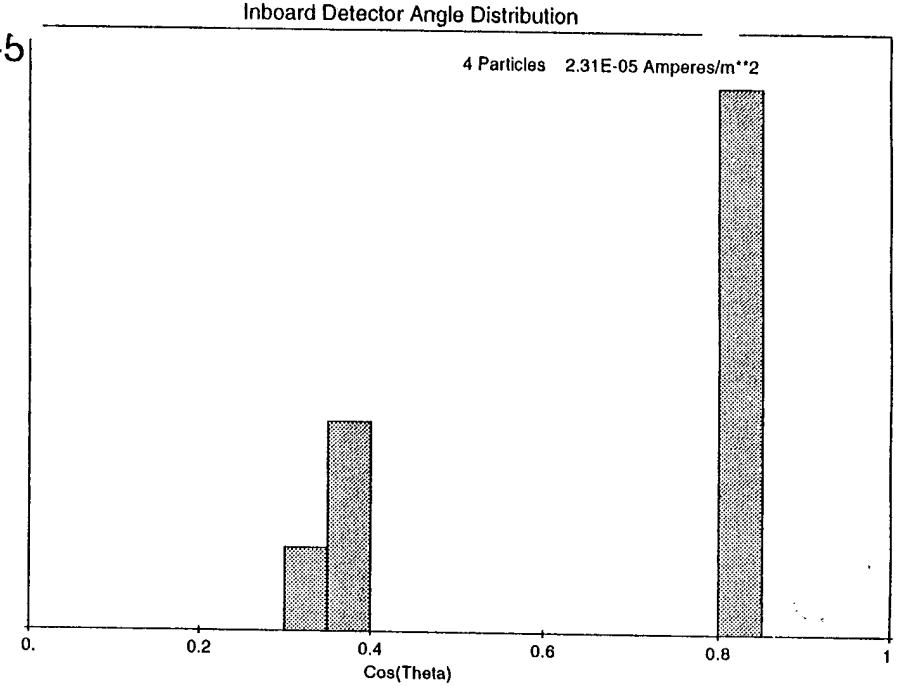

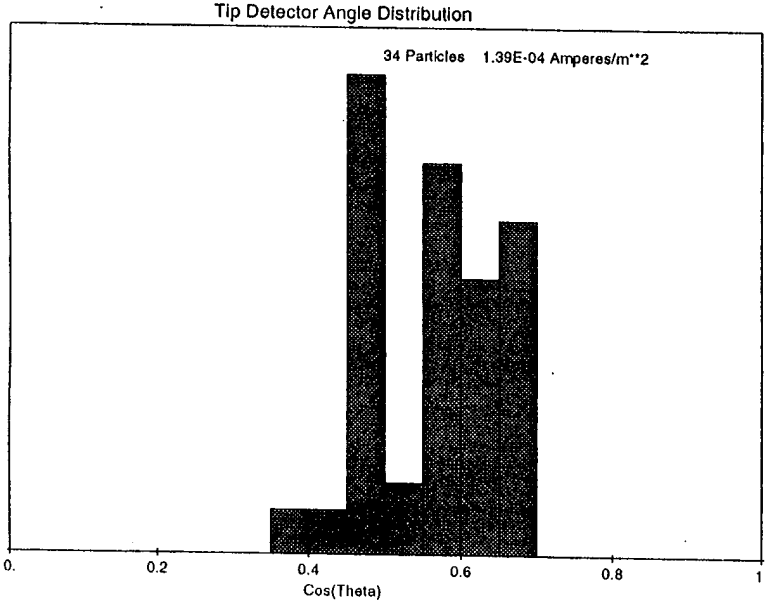

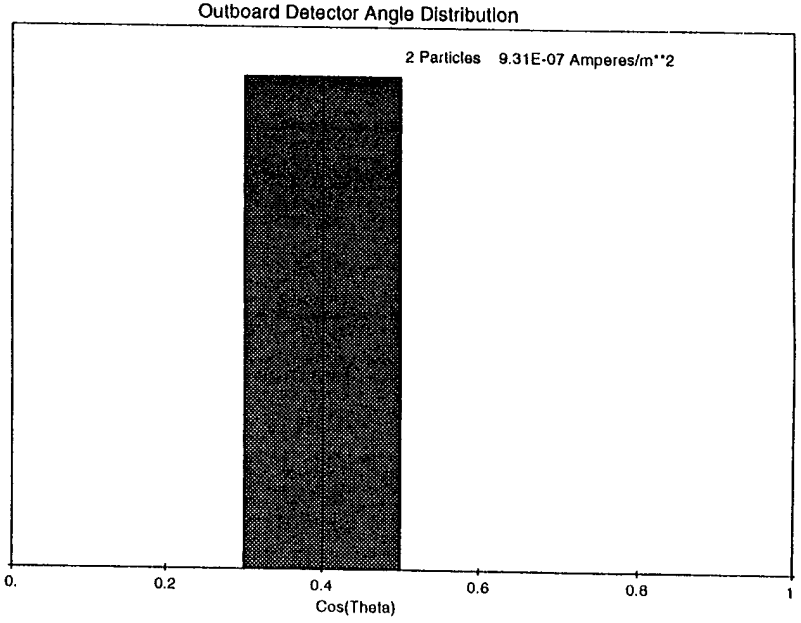

Run Code 29 −5 Volts on WSF

100 Volts Bias <J> = 2.1x10^{-5}

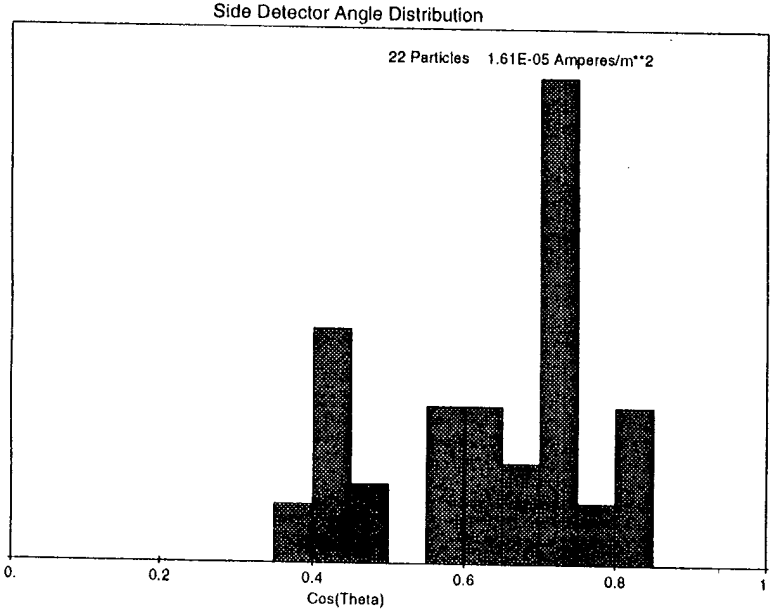

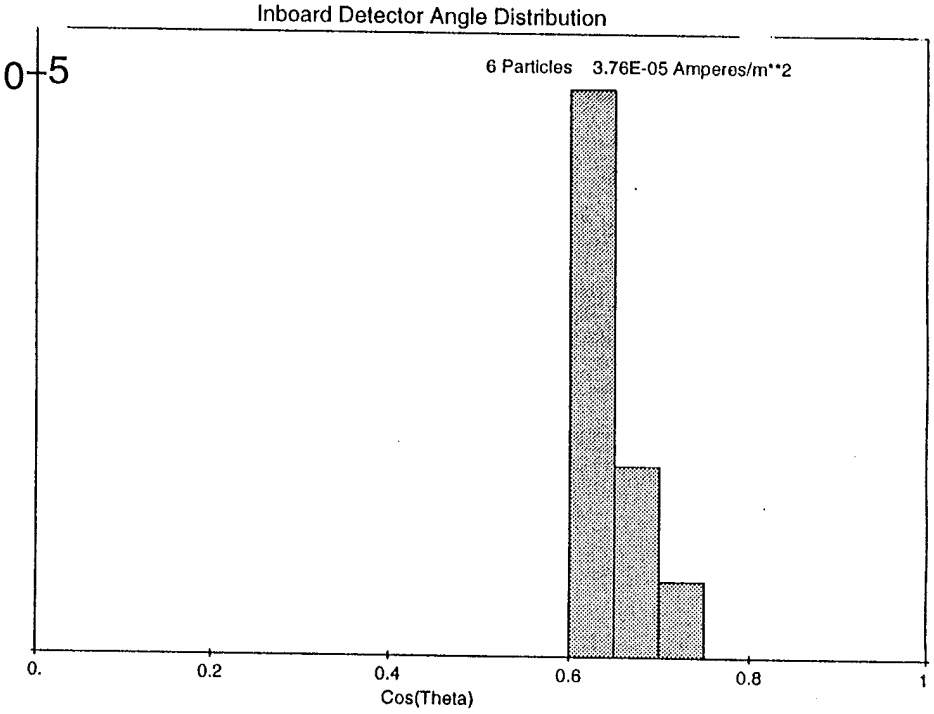

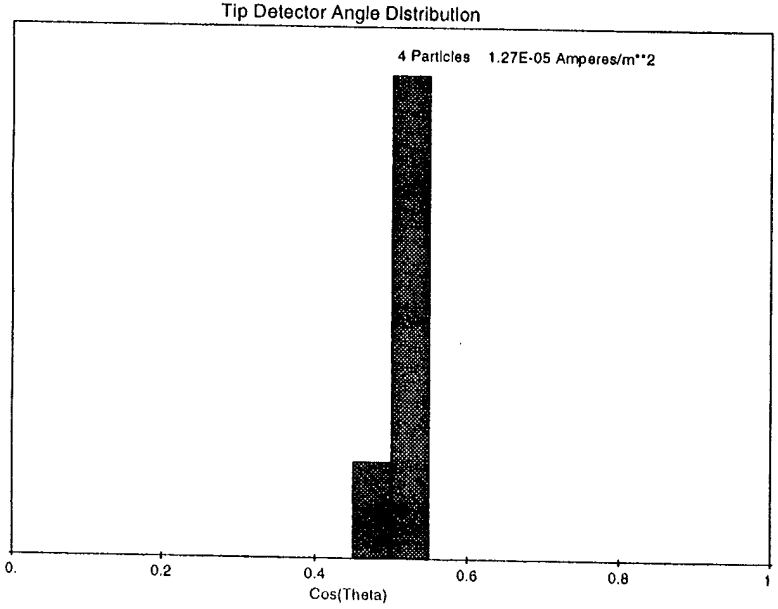

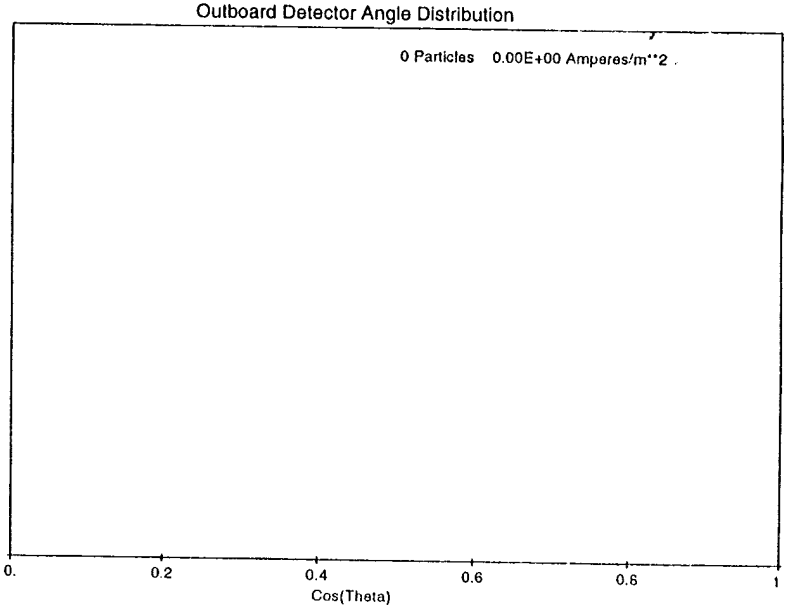

Run Co( ) 34 40 deg. Tilt <J> = 2.7x1_ -5

50 Volts Bias −5 Volts on WSF

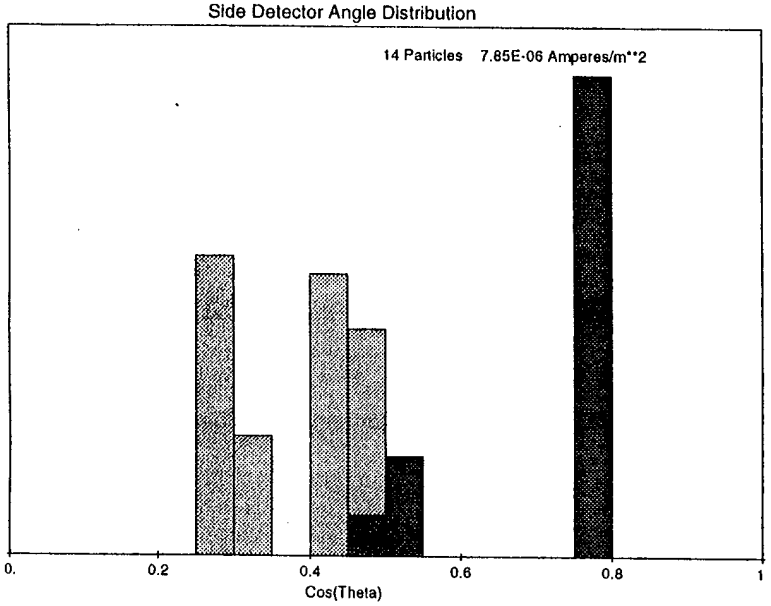

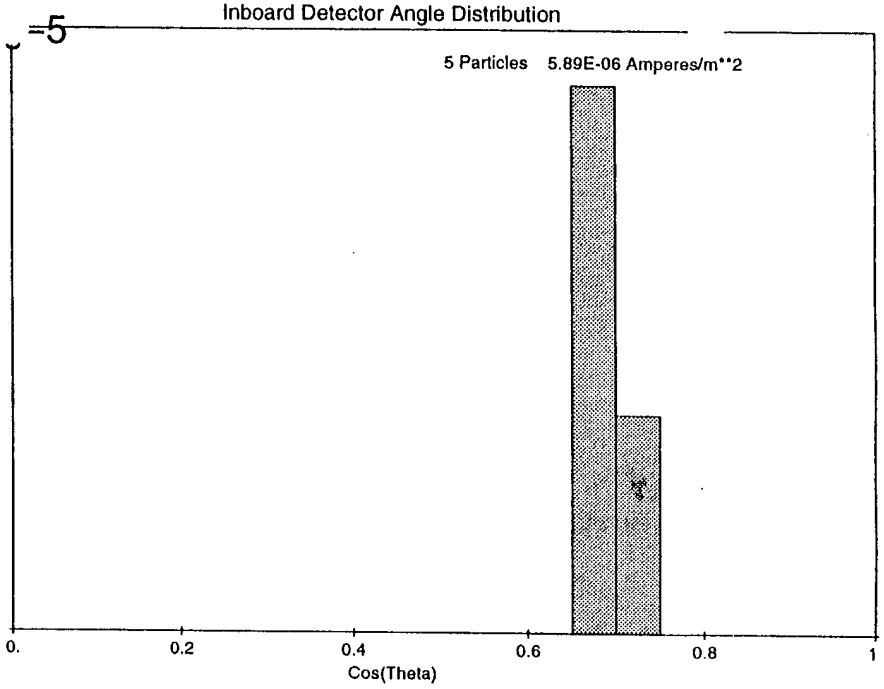

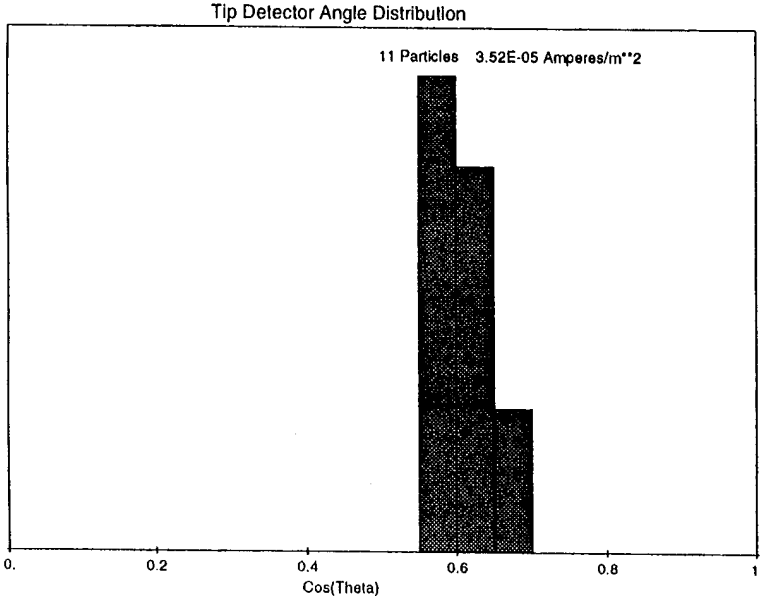

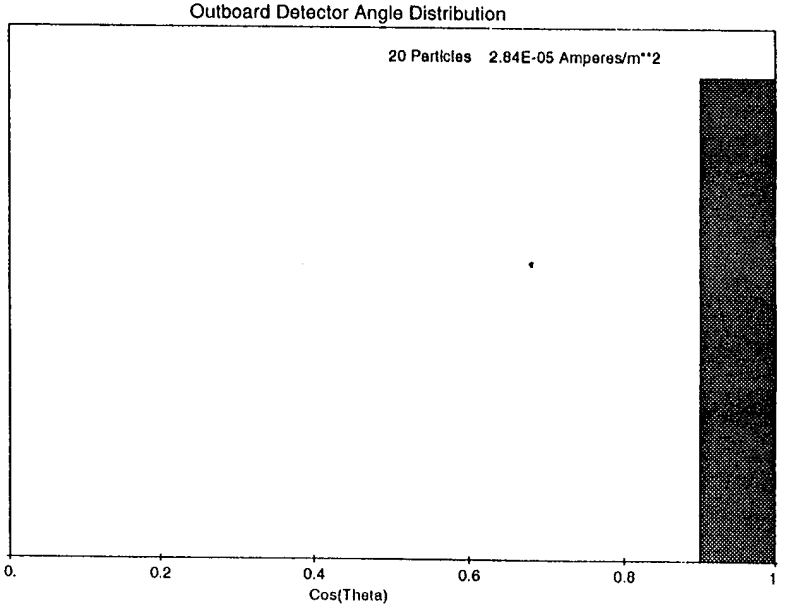

Current Measurements by CHAWS Detectors

The DynaPAC calculations yield the current density and angular distribution of ions at the CHAWS detector locations, as well as the total current to the probe. The concern is that, due to the construction of the detectors, the current measurements will be so constricted to near-normal incident angles as to be totally unrepresentative of the actual current density to the detector location. In the absence of adequate calibration data, the following provides a simple, quantitative estimate of this effect for use in interpreting the measurements.

The detectors are grounded, nearly planar surfaces, over 1 inch in diameter, located approximately 1/8 inch behind a mesh screen contiguous with the detector outer shell. In order to reach the detector, an ion that strikes the mesh screen must have sufficient normal velocity to overcome the retarding potential between the biased mesh and the grounded detector. This leads to the condition

$$\cos^2\theta > V/(E + V)$$

where θ is the incident angle relative to normal, V is the bias of the CHAWS detector shell, and E is the ion energy relative to WSF ground (i.e., ram energy + WSF negative potential).

Two figures display the results. Figure 27 shows the fraction of an isotropic incident flux the detector would see, while Figure 28 displays the cutoff angle directly.

At the current collection threshold of 100 volts bias, the cutoff angle for O^+ is about 12.5 degrees, and the detector would measure only about five percent of an isotropic incident flux. For H^+ the situation is far worse. At potentials of a kilovolt or more, the detectors are pretty well shut down. Negative potential on the WSF leads to only moderate improvement in this situation.

For the ESA's, which are hidden behind the current detectors, the situation is even bleaker. Ions approaching the probe at the limiting angle have glancing incidence on the current plate, so that the cutoff angle for detection by the ESA's is appreciably smaller than shown in the figures.

For most of the calculations the peak current density to each detector lies well outside the acceptance angle, and numerous cases show no ions at near-normal incidence. While there is more likely to be H^+ at near-normal incidence, the low ram energy of H^+ negates that factor. It is difficult to see how any conclusions can be drawn from the detector data concerning distribution of ion current over the probe. We strongly recommend that a new detector design be adopted for the next WSF flight.

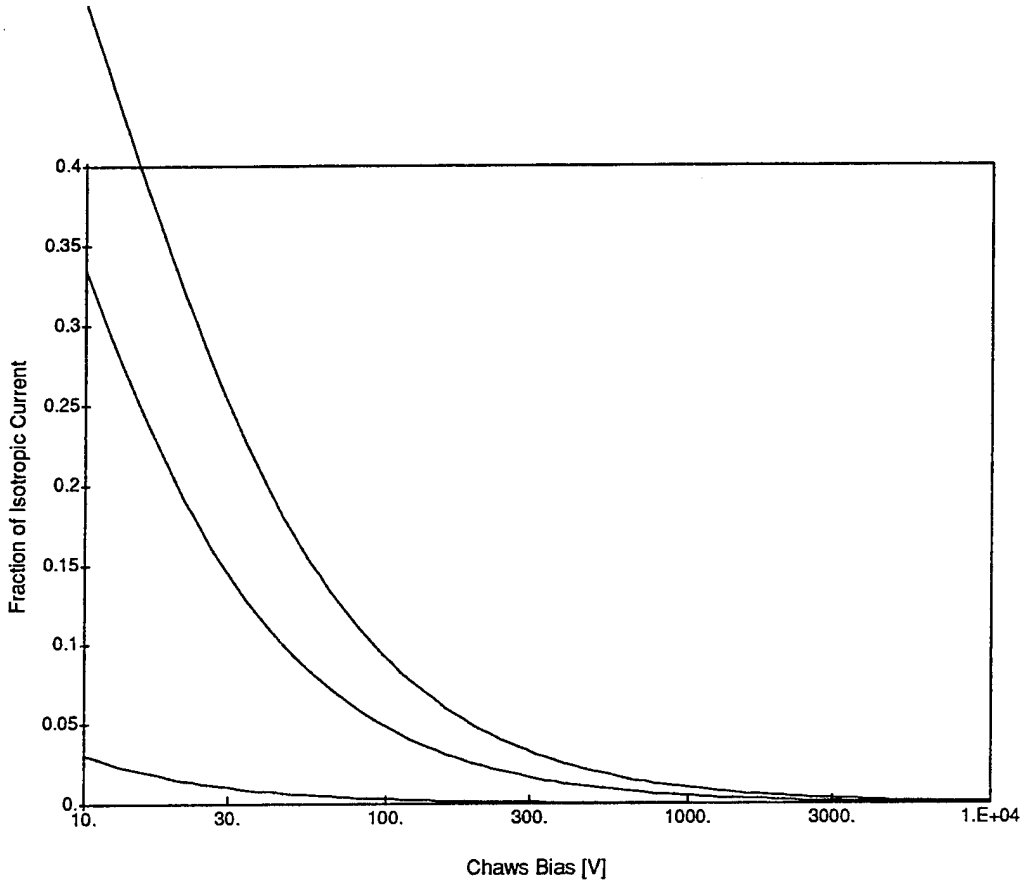

Figure 27. Fraction of isotropic incident flux detector would see for three cases. Upper curve: 0^+ with a disk potential of -5 V. Middle curve: 0^+ with a disk potential of 0 V or H^+ with a disk potential of -4.7 V. Lower curve: H^+ with a disk potential of 0 V.

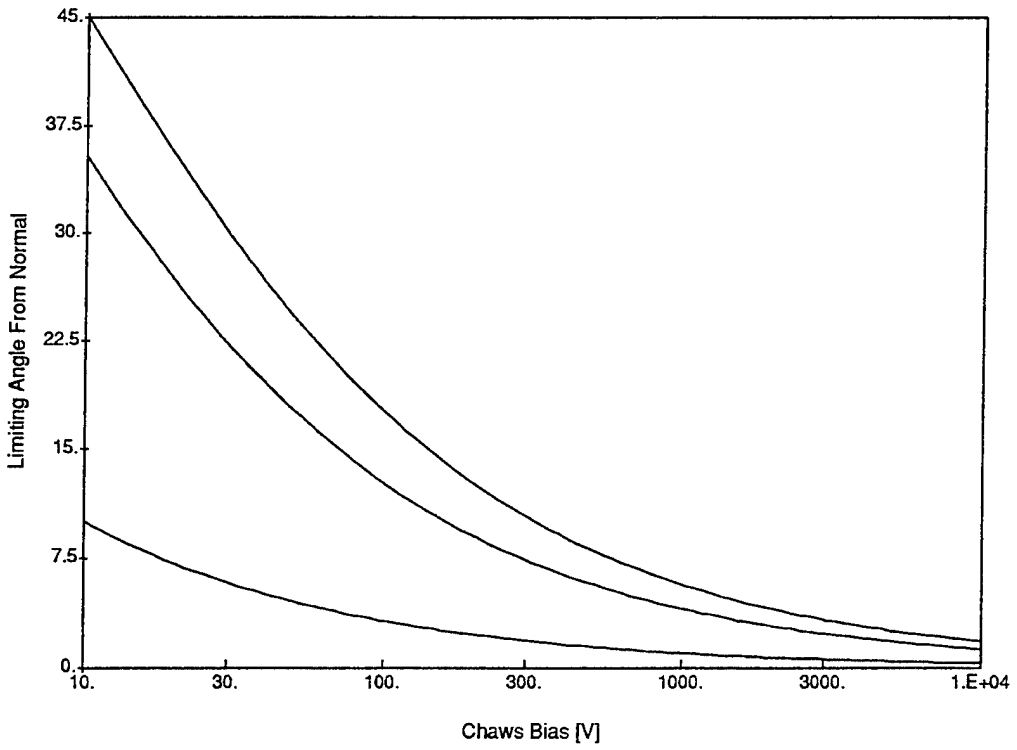

Figure 28. Cutoff angle of incident flux for three cases. Upper curve: 0^+ with a disk potential of -5 V. Middle curve: 0^+ with a disk potential of 0 V or H^+ with a disk potential of -4.7 V. Lower curve: H^+ with a disk potential of 0 V.

8. SIMPLE MODELS FOR WSF WAKE SIDE SENSOR COLLECTION AND THRESHOLD

We have performed current collection calculations for the WSF wake side sensor in three dimensions (using DynaPAC), and in two-dimensional XY and axisymmetric geometries (using Gilbert). At this point, it is highly instructive to develop some simple models which attempt to reproduce some of the qualitative features of the more detailed calculations.

1. Basic Physical and Geometrical Parameters

The basic problem is that a 5 eV O^+ ion enters the potential field of the CHAWS probe at the WSF edge. We wish to know, for a given CHAWS bias voltage, whether the ion will strike the probe, and, if so, at what location and angle.

The probe is a cylinder with diameter 4.25 inches and length 18 inches. From previous experience, we approximate the probe as a sphere with the same surface area, giving an equivalent spherical probe radius of 11.75 cm. The probe center is located 9 inches behind the WSF and 20 inches from the WSF edge.

Physical Parameter	Symbol	Value
Ion Energy	E_0	5 eV
Probe Potential	ϕ	(Varies)
Equivalent Spherical Probe Radius	R_p	11.75 cm
distance Behind WSF	d	22.86 cm
Distance From WSF Edge	b	50.80 cm

2. Monopole Model

The simplest model, which can be solved analytically, is to ignore the WSF and treat the ions as incident on a spherical potential. Equating energy and angular momentum gives

$$\frac{1}{2}\frac{m}{e}v_f^2 = E_0 - \phi$$

$$mv_f R_p = mv_0 b$$

$$\left(\frac{v_f}{v_0}\right)^2 = \left(\frac{b}{R_p}\right)^2 = (E_0 - \phi)/E_0$$

$$\phi = E_0\left(1 - \left(\frac{b}{R_p}\right)^2\right)$$

which gives a threshold potential of -88.5 volts.

3. Dipole Model

The WSF is well approximated as an equipotential plane at zero volts. We can incorporate this into our model by placing a positive potential sphere as the mirror image of the CHAWS sphere, a distance d ramward of the WSF surface. For the parameters above, very nearly spherical equipotentials at the locations of CHAWS and its image are produced by point charges located 22 cm from the equipotential plane.

To sample this model, we track trajectories of 5 eV O^+ ions from the point corresponding to the WSF edge. Figure 29 shows ion trajectories for CHAWS bias potentials from 25 volts to 50 kV. As expected, at low potentials ions are merely deflected and never approach the probe. An unexpected result was that for high potentials the ions have approximately semicircular orbits which also never approach the probe. Since this does not correspond to the DynaPAC result, we are forced to conclude that this is a poor representation of the actual WSF/CHAWS potential

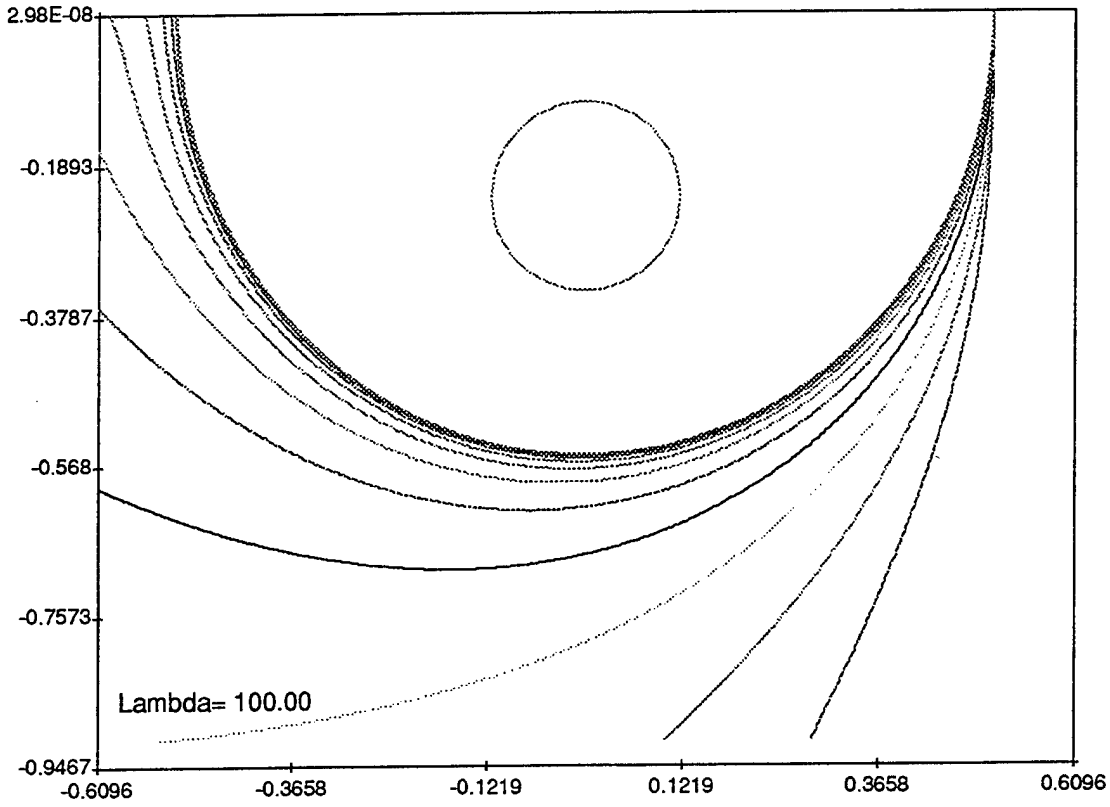

Figure 29. Trajectories of 5 eV O^+ ions in the unscreened dipole potential model for various potentials on the CHAWS equivalent sphere. The sphere potentials are -25 volts (outermost trajectory), -50, -100, -200, ... , -51,200 volts.

4. Screened Dipole Model

Comparing the DynaPAC calculated potential with the dipole model, we note that it is of considerably shorter range due to the presence of ion charge both in the wake region and in the ram flow region. A simple modification to the dipole model is linear (Debye) screening of each point charge. We present results corresponding to screening lengths of 25 cm and 50 cm (two and one screening lengths between CHAWS and the WSF edge). With point charges a distance $d(\lambda)$ from the zero potential plane, the potential at a field point, P, is given by

$$\phi(P) = VQ(\lambda)\left(\frac{\exp(-r_2/\lambda)}{r_2} - \frac{\exp(-r_1/\lambda)}{r_1}\right)$$

where r_1 and r_2 are the distances of P from the CHAWS point charge and its image, respectively, and -V is the CHAWS bias voltage. For the geometrical parameters in the table above, the screening-dependent parameters are

λ	d (λ)	Q (λ)
25 cm	22.41 cm	20.61 cm
50 cm	22.17 cm	17.54 cm
100 m	22.00 cm	16.23 cm

Figures 30 and 31 show particle trajectories (as for the unscreened dipole case) for this model. With λ = 50 cm, there is a collection threshold of nearly 400 volts. The trajectories of collected ions nearly strike the WSF and impact the probe moving away from the WSF. This behavior is qualitatively different from DynaPAC calculated trajectories, which strike the probe tip and side moving toward the WSF. For λ = 25 cm the threshold for collection is below 200 volts. The ion trajectories are qualitatively similar to those calculated by DynaPAC. This suggests that the screened dipole model, with λ = 25 cm, may be useful for making quick calculations of ion collection by the CHAWS probe.

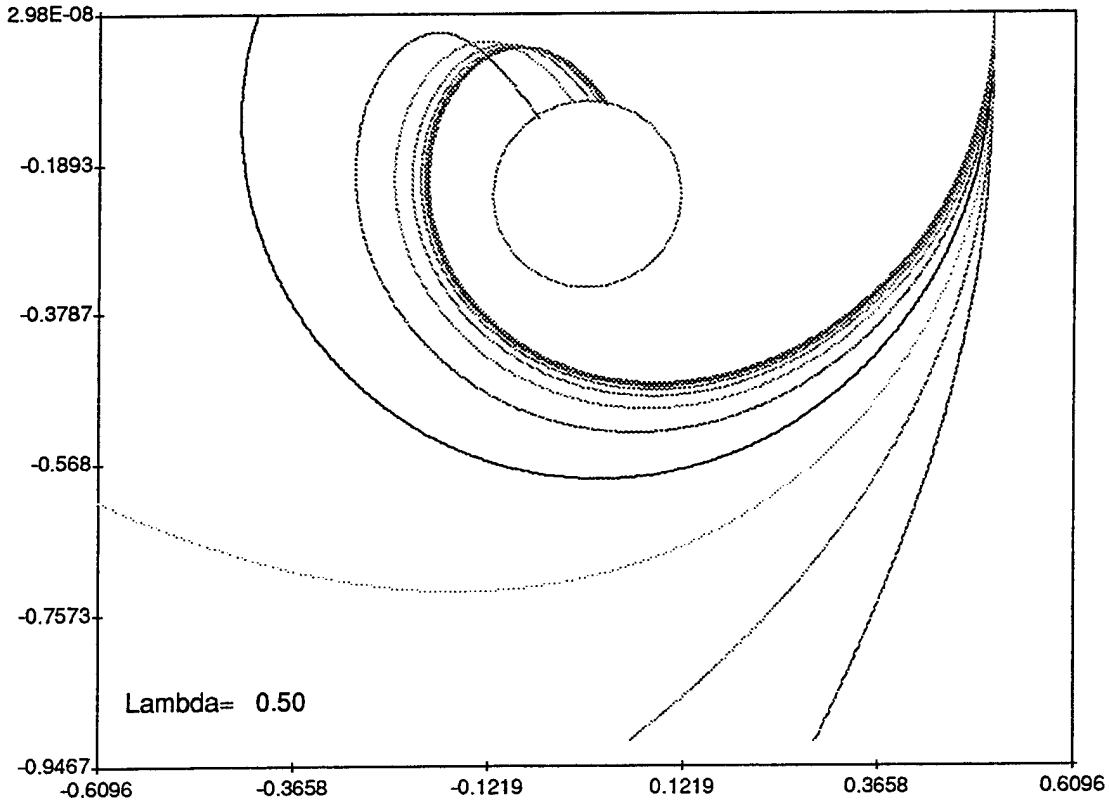

Figure 30. Trajectories of 5 eV O^+ ions in the screened dipole potential model for $\lambda = 50$ cm. Trajectories correspond to the same probe potentials as in Figure 29. The first trajectory striking the sphere corresponds to -400 volts.

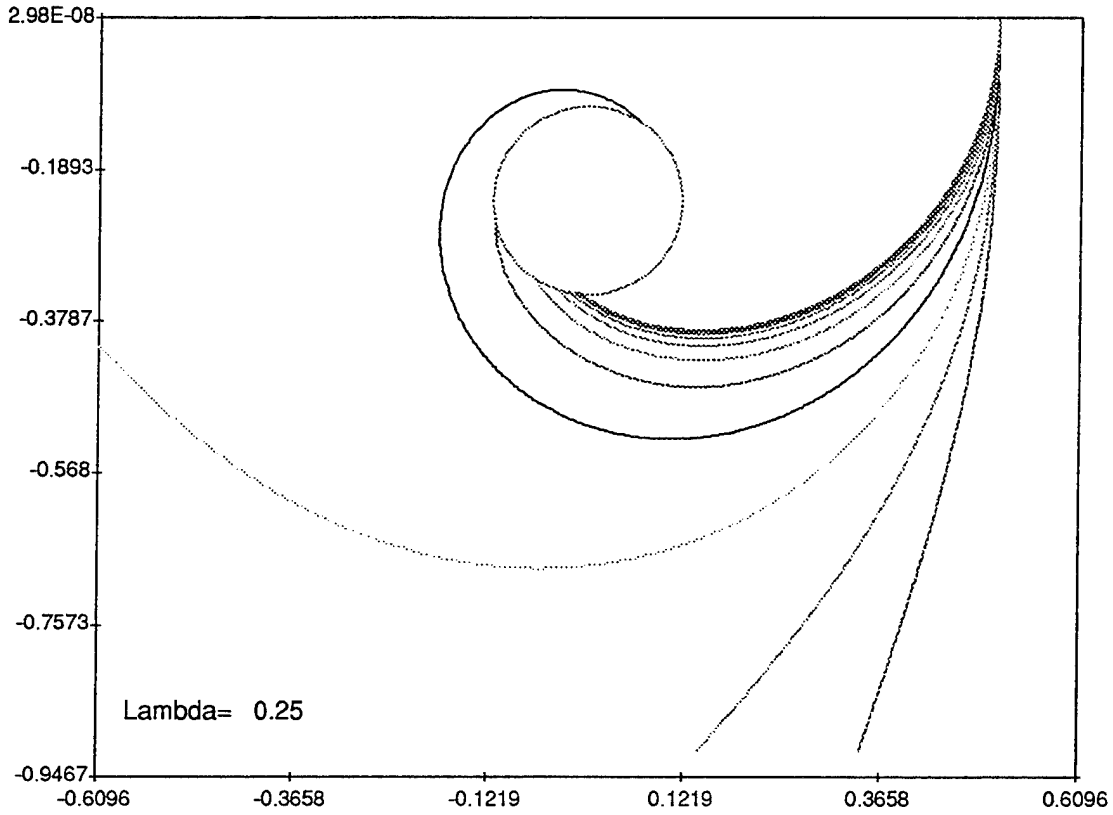

Figure 31. Trajectories of 5 eV O^+ ions in the screened dipole potential model for $\lambda = 25$ cm. Trajectories correspond to the same probe potentials as in Figure 29. The first trajectory striking the sphere corresponds to -200 volts.

9. EPSAT WAKE STUDIES SCREEN

The EPSAT Wake Studies screen uses the neutral approximation to compute the densities and current densities of the neutral and plasma species in front of or behind a disk. The input parameters are the disk parameters, the spacecraft velocity, the ambient neutral and plasma environment, the point of interest, the look direction, and the incident energy.

The disk is described by its normal, its radius, and the location of its center. The normal of either the ram facing side or the wake facing side can be given.

By default the spacecraft velocity is given by the EPSAT orbit generator.

The ambient neutral and plasma environments are shown on the Neutral Density at a Point and Plasma Density at a Point screens. The density of each neutral and ion species and the neutral and ion temperatures are used.

The point of interest can be specified either by specifying an origin and a distance from that origin in spherical coordinates or directly in Cartesian coordinates.

The look direction can be specified either in terms of the spherical coordinate angles or in Cartesian coordinates. This parameter is only used for the current density computation.

The incident energy is given in electron volts. This parameter is only used for the current density computation. If the energy is negative, the current density is zero.

Densities

On the ram facing side of the disk, the densities are the ambient densities. The point of interest is on the ram facing side if the dot product of the normal of the wake facing side of the disk with the vector from the center of the disk to the point of interest is negative.

On the wake facing side of the disk, the density for each species is the integral

$$\rho(\mathbf{r}) = \rho_a(\pi T)^{-3/2} \int d\Omega \, dE\sqrt{E} \, g(\mathbf{r},\theta,\phi) \exp\left(-\left(\frac{E + E_{ram} + 2\sqrt{E E_{ram}}\cos\theta}{T}\right)\right)$$

The ambient density of the species is ρ_a. The ion temperature is T. The vector $\mathbf{r}$ is the vector from the center of the disk to the point of interest. The energy E is the incident particle energy. The energy E_{ram} is given by

$$E_{ram} = \frac{1}{2} m_s v_{ram}^2$$

where m_s is the mass of the species and v_{ram} is the spacecraft velocity. The integral is done over the polar coordinates θ and ϕ, representing the negative of the incoming particle's velocity direction, where the origin for the integral is at the point of interest and θ is measured from the negative spacecraft velocity direction. The function g is zero if the direction given by θ and ϕ is blocked by the disk and unity otherwise.

The integral is solved differently for the case where the disk is normal to the spacecraft velocity and where it is not. A different technique is also used for the case in which the point of interest is directly behind the disk and where it is to the side.

Solution Technique for Normal Orientation and Point Directly Behind Disk

The outermost integral over the azimuthal angle, ϕ, is performed taking zero as the direction to the nearest disk edge point. To get a concentration of points near the nearest edge point, we define $\psi = \phi^{1/2}$. The minimum value of $\cos\theta$ can be shown to be

$$u_{min}(\phi) = -\left[1 + (x/z)^2\right]^{1/2}$$

$$x/r = -\cos\phi + \left[\cos^2\phi + (R/r)^2 - 1\right]^{1/2}$$

(The maximum value of $\cos\theta$ is 1, for particles overtaking the spacecraft from behind.) The energy variable is transformed by $t = e^{-E/E_0}$, where E_0 is an enerutational convenience. It is taken to be

$$E_0 = \left(\frac{m}{2e}\right)\frac{\left(V + 5\sqrt{\frac{2eT}{m}}\right)^2}{ln\left(n_t\right)}$$

where n_t is the number of integration points used for the t-variable (i.e., energy). (Note: E_0 should be set to at least the ion temperature, T.)

After appropriate manipulation, the density at a point in the wake of the disk is given by

$$\frac{\rho}{\rho_a} = \pi^{-3/2}\frac{E_0}{\sqrt{T\,E_{ram}}}e^{-E_{ram}/T}\int_0^{\sqrt{\pi}}\psi\,d\psi\int_0^1 dt\,K(\psi,t)$$

$$K(\psi,t) = t^{\left(\frac{E_0}{T}-1\right)}\left\{e^{-\gamma(t)u_{min}(\psi)} - e^{-\gamma(t)u_{max}(\psi)}\right\}$$

$$\gamma(t) = \sqrt{\frac{-4\,E_0\,E_{ram}\,ln\,t}{T^2}}$$

Note that, to avoid overflows, all the exponents (including the one in the prefactor) should be grouped together, so that the only exponentiations are the two in the inner loop.

EPSAT performs the integrals numerically.

Solution Technique for Normal Orientation and Point Not Directly Behind Disk

The integral is over those trajectories blocked by the disk, and the result subtracted from unity. The outer integral is over the angle between the look direction and the vector toward the ram, which takes the range

$$\frac{1}{\sqrt{1+\left(\frac{R+r}{z}\right)^2}} < u = \cos\theta < \frac{1}{\sqrt{1+\left(\frac{r-R}{z}\right)^2}}$$

To concentrate points toward the ram direction, the integration variable is changed to $w = \sqrt{1-u}$. The integral over azimuthal angles contributes a factor

$$\Delta\phi(u) = 2\arccos\left\{\frac{\left[\left(r^2 - R^2 - z^2\right)u^2 + z^2\right]}{\left[2\,r\,z\,u\left(1-u^2\right)^{1/2}\right]}\right\}$$

The final result is

$$1 - \frac{\rho}{\rho_0} = \left[\frac{E_0}{\pi T}\right]^{3/2} e^{\frac{-E_{ram}}{T}} \int_{\sqrt{1-u_{max}}}^{\sqrt{1-u_{min}}} w\,dw\,\Delta\phi\left(1-w^2\right) \int_0^1 dt\,K'\left(1-w^2,t\right)$$

$$K'(u,t) = t^{\left(\frac{E_0}{T}-1\right)} e^{\gamma(t)u} \left(-lnt\right)^{1/2}$$

$$\gamma(t) = \sqrt{\frac{-4\,E_0\,E_{ram}\,lnt}{T^2}}$$

Solution Technique for Other Orientations

If the normal to the disk is not parallel to the velocity, the problem is solved similarly, although the geometry is more complex.

First, the disk and the field point are projected onto a plane normal to the velocity (Z), so that the disk edge is an ellipse with its major axis in the X direction.

$$x^2 + \alpha y^2 = R^2$$

The point (x, y) on the ellipse nearest the field point projection (x_0, y_0) (for the first quadrant) satisfies

$$x(\alpha - 1) - \alpha x_0 + x y_0 \sqrt{\frac{\alpha}{R^2 - x^2}} = 0$$

When (x_0, y_0) lies inside the ellipse, the outer angular integral is over the angle, ϕ, from the field point to the wake edge, given by

$$\phi = \arctan\left[\frac{y-y_0}{x-x_0}\right] \pm \psi^2$$

where the integration variable, ψ, concentrates near the presumed integrand peak at (x, y). There are two values of u_{min} (the cosine of the angle between the direction from the field point to the disk edge and the negative velocity direction) for each ψ, obtained by calculating the disk edge point $(x_0 + d\cos\phi, y_0 + d\sin\phi, z_1)$. The values are determined by first solving the ellipse equation d, then the circle equation for z_1. Then

$$u_{min} = \frac{z_0 - z_1}{\sqrt{d^2 + (z_0 - z_1)^2}}$$

where the sign of z_1 is opposite the sign of $y_0 + d\sin\phi$. The energy integral then proceeds as for the velocity-aligned case, except that the normalization must take account of the asymmetry in the ϕ integral.

When (x_0, y_0) lies outside the ellipse, the integral is over the region from which ions are excluded and the normalized result subtracted from unity. The outer angular integral is over the variable u (the cosine of the angle between the ram direction and the direction from the field point to a point on the disk), which goes from the angle corresponding to the near point of the disk to the diametrically opposite point. For each u, there are two values of ϕ that satisfy both the disk edge equation and the defining equation for u:

$$(x_0 + d\cos\phi)^2 + \alpha(y_0 + d\sin\phi)^2 = R^2$$

$$(x_0 + d\cos\phi)^2 + (y_0 + d\sin\phi)^2 + z^2 = R^2$$

$$z(y_0 + d\sin\phi) \le 0$$

$$u = \frac{z - z_0}{\sqrt{d^2 + (z - z_0)^2}}$$

The difference between the two ϕ values corresponds to the $\Delta\phi(u)$ that appears in the velocity-aligned case.

Current Densities

The current density model is undergoing modification.

10. EPSAT CHAWS CURRENT SCREEN

The CHAWS Currents screen is used to compute the DynaPAC and POLAR predicted current to the wake side probe under the given conditions.

The year and time are used with the orbit generator to compute the present position, sunspot number, and velocity. The plasma environment is computed from the position and sunspot number in the usual manner.

The user inputs the appropriate probe parameters. The tilt angle is the angle between the normal of the Wake Shield and the velocity direction. All tilt is assumed to be about the pitch axis, the line in the plane of the shield, passing through the center, and normal to the line passing through CHAWS and the center of the shield. Positive angles are those in which the probe is further into the wake.

The potential at the edge of the Wake Shield can influence the current collected. The POLAR calculations ignored this effect. The DynaPAC calculations used a uniformly charged disk. In actuality, the potential varies across the disk. The potential at the edge nearest the probe is assumed to be the most important. Since only a negative voltage on the disk is anticipated, only the magnitude of this number is used. The disk is taken to be at a negative potential with the magnitude displayed in volts.

The active field SWEEP VOLTAGES can be used to display, but not change, the voltage as a function of sweep and step number.

The probe bias is determined from the sweep voltage table, the sweep number, and the sweep time. The sweep time, given in seconds, is converted to a step number from the knowledge that it takes 60 seconds for the probe to go through the 32 voltage steps. The step number is then used with the sweep number to determine the present probe bias in volts. The probe bias may also be entered

directly, as is usual with EPSAT. If the probe bias shown is a positive number, the code uses the negative of the displayed number for the calculations.

The user may also enter values for the secondary yield parameters. The secondary yield is determined from these parameters using the formulation given in Chapter 13.

The quantity labeled DynaPAC Fit—Total, is the current to the wake side probe as predicted by the fit to the DynaPAC calculations given in Chapter 7. The quantity labeled DynaPAC Fit—With Secondaries, is the same quantity including secondary emission effects.

The quantify labeled Polar Fit—Total, is the current to the wake side probe as predicted by a piece wise linear fit to the POLAR results provided by D. Cooke of Phillips Laboratory. The POLAR calculations were done for probe biases from –10 to –5000 V, plasma densities of 10^{10}, 10^{11}, and 10^{12} m^{-3}, and tilt angles of –30, 0, and +30 degrees. The POLAR calculations were done for pure atomic oxygen with thermal energy 0.1 eV and moving at mach 7. EPSAT uses the electron density (total plasma density) for the atomic oxygen density. The quantity labeled Polar Fit—With Secondaries is the same quantity including secondary emission effects. The secondary emission is calculated assuming that all the incident current is atomic oxygen ions.

This screen was set up to allow the user to directly compare the calculated and experimental currents on the same curve. To enter the experimental points, the user chooses the EXPERIMENTAL POINTS field. The number of points and the min and max voltages can be used to set the voltage column. The user can also directly enter voltage values. The user should take care to enter negative values for the voltage so that the interpolation works correctly. The experimental current values are entered by the user.

The quantity labeled Experimental Fit is a linear interpolation (in applied potential) between the values on the EXPERIMENTAL DATA screen.
The DynaPAC and POLAR fits are most likely to agree in a pure oxygen 0.1 eV plasma with no tilt or shield potential, i.e. when the assumptions are the same.

11. GEOMAGNETIC COORDINATES IN EPSAT

Geomagnetic Coordinates in EPSAT

The Geomagnetic Position was added to the Geomagnetic Field at a Point screen.

The relationship between the geomagnetic coordinates (Φ, Λ) and the geographic coordinates (ϕ, λ) of a point is given by

$$\sin\Phi = \sin\phi \sin\phi_o + \cos\phi \cos\phi_o \cos(\lambda - \lambda_o)$$

$$\sin\Lambda = \frac{\cos\phi \sin(\lambda - \lambda_o)}{\cos\Phi}$$

where ϕ_o is 78.3°N and λ_o is 291.0°E.

Testing

No object is needed.

For the default mission and time the geomagnetic field at a point screen looks as shown in Figure 32.

```
                          |   Geomagnetic Field    |
                          |      at a Point        |
                          +---------HELP!----------+
------------------ Mission Dates -------------------+----- Present Position -----
            YYYY+DDD HH:MM:SS                       |     Altitude:     324.10
  Start Date: 1990+100  0: 0: 0                     |    Longitude:     165.26
  Event Date: 1990+100  0: 0: 0  Time Since Event   |     Latitude:       1.85
                                      60.000        |--> Geomagnetic Position
        MET:    0+ 0  0: 1: 0                       |    Longitude:     235.29
        GMT: 1990+100  0: 1: 0                      |     Latitude:      -4.68
-------------------------------------------------------------------------------
        Geomagnetic Field          X      Velocity     --->   Induced Field

Space Coordinates  Body Coordinates    Body Coordinates      Body Coordinates
North:  2.978E-01   X:  1.809E-01   |   X:  7.726E+03   |    X:  2.832E-05
 East:  4.666E-02   Y: -2.412E-01   |   Y:  0.000E+00   |    Y:  3.286E-02
 Down: -4.251E-02   Z: -4.251E-02   |   Z:  1.174E+00   |    Z: -1.863E-01
                                    |                   |
      Magnitude:  3.045E-01         |     Magnitude     |      Magnitude
      Dip Angle:     -8.03          |     7.726E+03     |      1.892E-01
    Declination:      8.90
```

Figure 32. Geomagnetic Field at a Point screen.

User contours can be used to plot the geomagnetic latitude and longitude as a function of geographic latitude and longitude. A 100 by 100 grid was used to create the following figures.

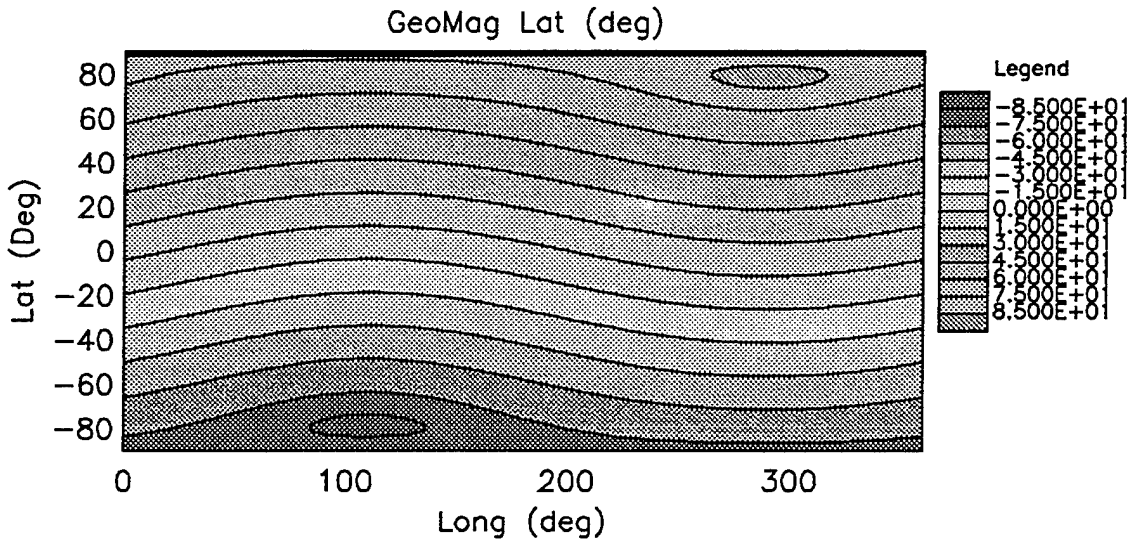

Figure 33. Geomagnetic Latitude as a Function of Geographic Latitude and Longitude.

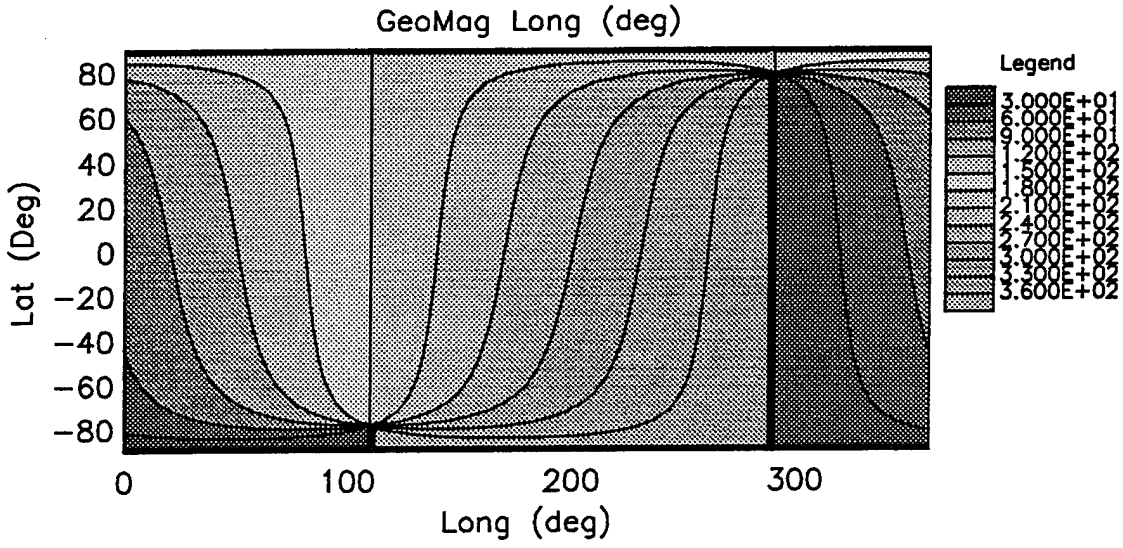

Figure 34. Geomagnetic Longitude as a Function of Geographic Latitude and Longitude.

12. EPSAT FLOATING POTENTIAL MODEL MODIFICATION

The Floating Potential Module was modified as follows:

The current collected by an object with property PLATE is now given by

$$I_p^i(\phi) = \sum_s A_s\left(j_{th}^a\left(\theta_p^s,\phi\right) + \gamma_s(T)\, j_{th}^r\left(\theta_p^s,\phi\right) g(\phi/T)\right)$$

The factor g accounts for the exponential decrease in electron current.

$$g(z) = \begin{cases} e^z & \text{for } z < 0 \\ 1 & \text{for } z \geq 0 \end{cases}$$

The factor γ is a correction to the current of repelled electrons due to $\mathbf{v} \times \mathbf{B}$ potential variation over a conducting surface. It is given by an integral over the surface.

$$\gamma_s(T) = \frac{\int_s d^2\mathbf{r}\, e^{f(\mathbf{v}\times\mathbf{B}\bullet(\mathbf{r}-\mathbf{R}_i),\phi(\mathbf{R}_i))/T}}{\int_s d^2\mathbf{r}}$$

where the function f is given by

$$f(a,b) = \begin{cases} a & \text{for } a+b \leq 0 \text{ and } b \leq 0 \\ a+b & \text{for } a+b \leq 0 \text{ and } b \geq 0 \\ -b & \text{for } a+b \geq 0 \text{ and } b \leq 0 \\ 0 & \text{for } a+b \geq 0 \text{ and } b \geq 0 \end{cases}$$

The integral is computed by dividing the surfaces into triangles. The triangles are constructed such that the three corners of each triangle are within the same regime of the function f. Then we have that

$$\gamma_s(T) = \sum_t \frac{A_s^t}{A_s} \gamma_s^t(T)$$

A_s^t = Area of triangle t of object side s

$$\gamma_s^t(T) = 2e^{c_o} \frac{c_2 e^{c_1} + (c_1 - c_2) - c_1 e^{c_2}}{c_1 c_2 (c_1 - c_2)}$$

where (for the case where the second argument of f is non-positive and the sum of the arguments of f is non-positive) the c_is are given by

$$c_o = f\left(\mathbf{v} \times \mathbf{B} \bullet (\mathbf{r}_o - \mathbf{R}_i), \phi\right)/T$$
$$c_1 = f\left(\mathbf{v} \times \mathbf{B} \bullet (\mathbf{r}_1 - \mathbf{r}_o), \phi\right)/T$$
$$c_2 = f\left(\mathbf{v} \times \mathbf{B} \bullet (\mathbf{r}_2 - \mathbf{r}_o), \phi\right)/T$$

for a triangle with vertices (r_0, r_1, r_2).

Testing

Test Object

A twelve-sided, 3.66 m radius, 0.01 m height, aluminum cylinder at the origin with object property PLATE.

A 10 m cubic, aluminum box at (0, 0, -10) with no object properties.

The orientation is set to have a pitch of 90.

Parameters

The parameters are set to 40 iterations, a potential limit of 1e-3 V, and a current limit of 1e-4 A.

Under the old scheme the floating potential screen for a disk bias of 0.1 V is shown in Figure 35.

```
     VIEW PARAMETERS     |          Floating          |
--------- Dates --------- |          Potentials        | VIEW SURFACE POTENTIALS
      YYYY+DDD HH:MM:SS ------------HELP!-------------
Start: 1990+100  0: 0: 0  Present Position ---- Plasma Environment Summary -----
Event: 1990+100  0: 0: 0   Alt:     324.10 Species Density    Min         Max
    Time Since Event       Lon:     165.26 o+     6.34E+11   1.11E+11   2.37E+12
        60.000             Lat:       1.85 h+     2.87E+10   1.53E+10   4.50E+11
 Magnetic Field (B)     Velocity           e-     6.66E+11   1.44E+11   2.54E+12
   X:       0.04    X:      -1.17        Temperatures      Thermal Currents
   Y:      -0.24    Y:       0.00        Ion:    8.1E-02       Ion:   3.36E-05
   Z:       0.18    Z:    7726.00   Electron:    8.2E-02  Electron:  -5.11E-03
 Mag:    3.0E-01   Mag:    7.7E+03
-------------------------------------------------------------------------------
  Total Current  9.752E-05
  Object     Object   Bias      V X B   Floating
   Name      Radius  Voltage   Voltage  Potential  Current    Resistance     a
----------                                        ---------- ---------- --------
disk           2.5      0.1      0.00      -0.15  1.31E-03       0.         0.
ground         6.9      0.0      0.00      -0.25 -1.21E-03       0.         0.
```

Figure 35. Floating Potential screen before change.

The surface potential figure is shown in Figure 36.

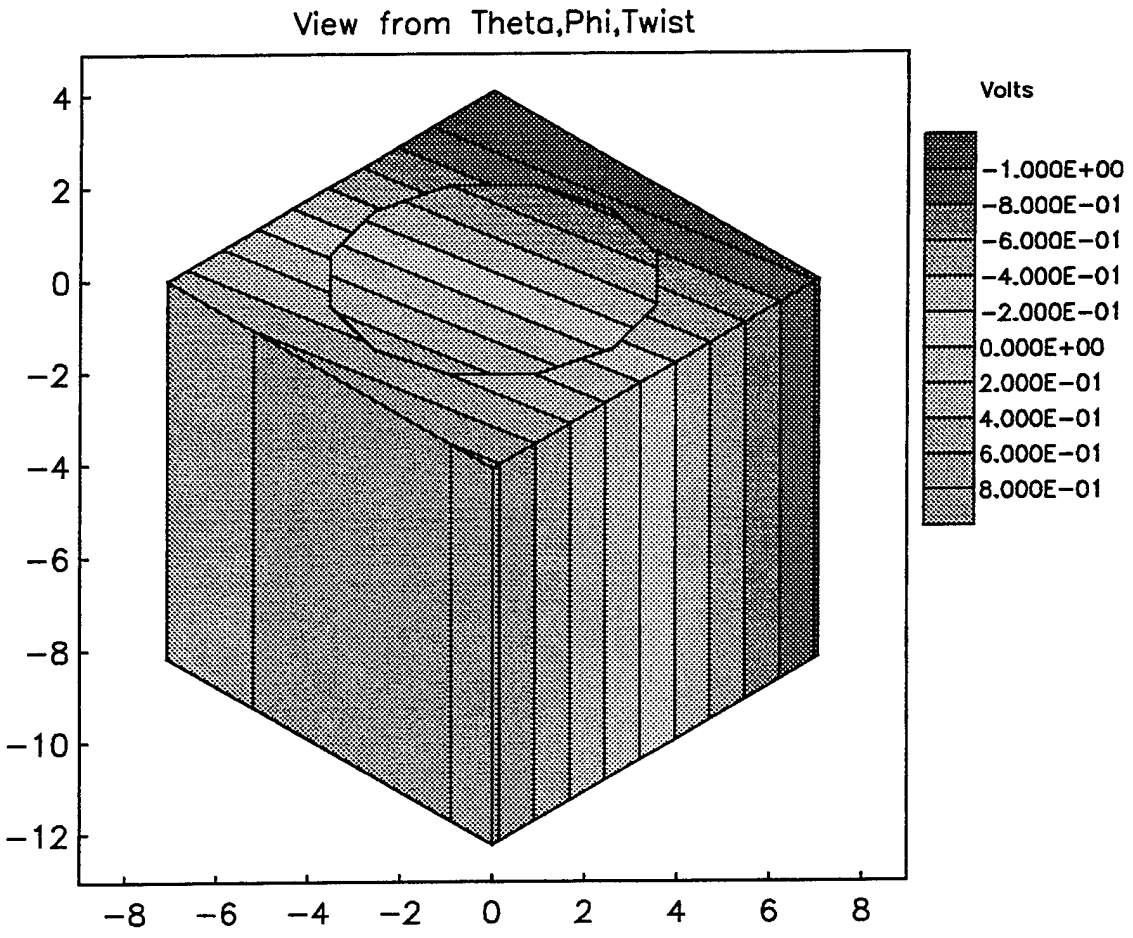

Figure 36. Surface potentials before change.

The current voltage curve is as shown in Table 7 and Figure 37. These were created from several do table commands in EPSAT.

Table 7. Disk potential and current as a function of bias before change.

Disk Bias	Disk Potential	Disk Current
-2.000	-2.237	0.033
-1.191	-1.428	0.033
-0.706	-0.943	0.033
-0.415	-0.652	0.033
-0.241	-0.478	0.032
-0.136	-0.374	0.031
-0.074	-0.313	0.028
-0.036	-0.277	0.026
-0.013	-0.255	0.024
0.000	-0.243	0.022
0.000	-0.243	0.022
0.020	-0.224	0.019
0.027	-0.218	0.018
0.038	-0.208	0.017
0.056	-0.191	0.013
0.087	-0.165	0.005
0.138	-0.125	-0.012
0.223	-0.072	-0.053
0.366	-0.028	-0.113
0.604	-0.016	-0.137
1.000	-0.015	-0.139
9.198	-0.015	-0.139
20.92	-0.015	-0.140
35.85	-0.014	-0.141
54.89	-0.014	-0.142
79.14	-0.013	-0.143
110.0	-0.013	-0.144
149.4	-0.012	-0.145
199.6	-0.011	-0.147
263.5	-0.010	-0.149
345.0	-0.009	-0.151
448.9	-0.008	-0.154
581.2	-0.007	-0.158
749.8	-0.005	-0.162
964.6	-0.003	-0.166
1238	-0.001	-0.172
1587	0.013	-0.178
2032	0.039	-0.186
2598	0.089	-0.196
3310	0.505	-0.207
3310	0.506	-0.207
3310	0.509	-0.207
3310	0.511	-0.207
3311	0.518	-0.207
3311	0.531	-0.207
3312	0.555	-0.207
3314	0.630	-0.207
3316	2.131	-0.207
3320	6.176	-0.207
3320	6.177	-0.207

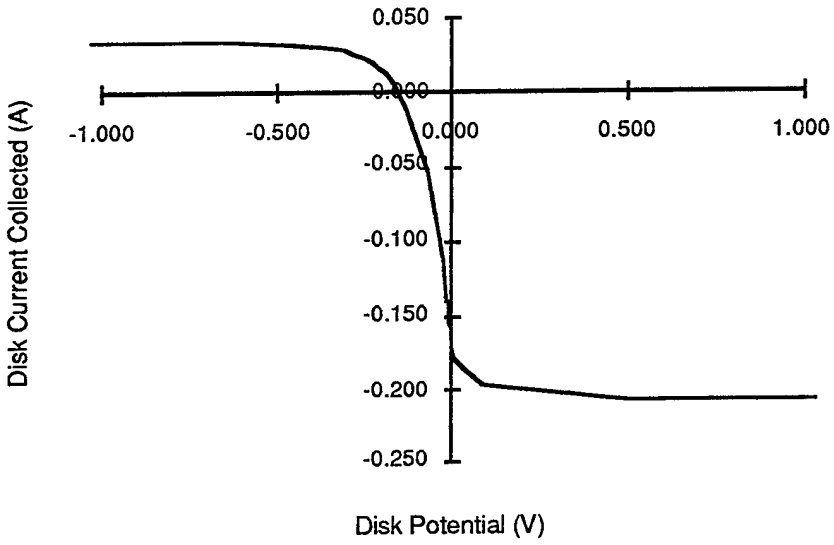

Figure 37. Disk current as a function of center potential before change.

The area of the disk is 42 m^2. The ram current to the disk is 35 mA. The electron thermal current to the disk is 215 mA. Note that the floating potential of the disk alone is about twice the temperature.

With the new scheme the floating potential screen for a disk bias of 0.1 V is shown in Figure 38.

```
     VIEW PARAMETERS     |              Floating          |   POTENTIAL EXTREMA
--------- Dates --------- |              Potentials        | VIEW SURFACE POTENTIALS
       YYYY+DDD HH:MM:SS ------------HELP!-------------
Start: 1990+100  0: 0: 0  Present Position ---- Plasma Environment Summary ----
Event: 1990+100  0: 0: 0   Alt:     324.10 Species Density    Min         Max
     Time Since Event      Lon:     165.26 o+      6.34E+11   1.11E+11    2.37E+12
         60.000            Lat:       1.85 h+      2.87E+10   1.53E+10    4.50E+11
 Magnetic Field (B)     Velocity           e-      6.66E+11   1.44E+11    2.54E+12
    X:       0.04     X:      -1.17        Temperatures      Thermal Currents
    Y:      -0.24     Y:       0.00        Ion:    8.1E-02      Ion:    3.36E-05
    Z:       0.18     Z:    7726.00   Electron:    8.2E-02  Electron:  -5.11E-03
  Mag:    3.0E-01   Mag:    7.7E+03
-------------------------------------------------------------------------------
  Total Current  5.907E-05
  Object     Object    Bias      V X B    Floating
   Name      Radius    Voltage   Voltage  Potential  Current    Resistance     a
----------
disk            2.5       0.1      0.00      -0.19  -4.94E-02   0.          0.
ground          6.9       0.0      0.00      -0.29   4.94E-02   0.          0.
```

Figure 38. Floating Potential screen after change.

The surface potential figure is shown in Figure 5.

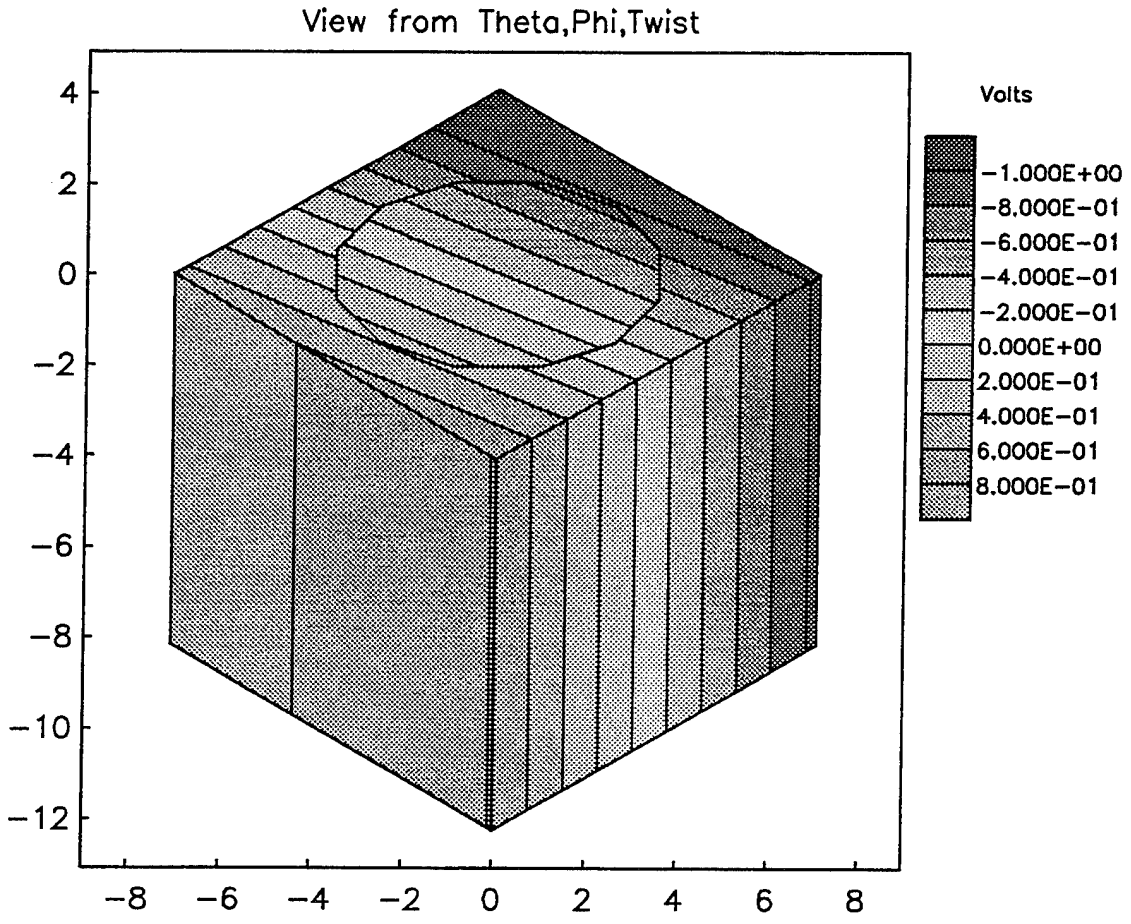

Figure 39. Surface potential after change.

The difference between the old and new calculational methods is more pronounced for a disk alone.

The current voltage curve is as shown in Table 8 and Figure 40. These were created from several do table commands in EPSAT.

Table 8. Disk potential and current as a function of bias after change.

Disk Bias	Disk Potential	Disk Current	
-2.000	-2.237	0.033	
-1.191	-1.428	0.033	
-0.706	-0.943	0.033	
-0.415	-0.656	0.024	
-0.241	-0.493	0.004	
-0.136	-0.398	-0.012	
-0.074	-0.342	-0.021	
-0.036	-0.309	-0.027	
-0.013	-0.289	-0.031	
0.000	-0.277	-0.033	
0.006	-0.272	-0.034	
0.016	-0.263	-0.036	
0.033	-0.248	-0.039	
0.054	-0.230	-0.042	
0.061	-0.224	-0.043	
0.108	-0.184	-0.051	
0.144	-0.154	-0.056	
0.187	-0.118	-0.063	
0.294	-0.031	-0.080	
0.318	-0.013	-0.083	
0.536	0.090	-0.125	
0.545	0.093	-0.126	
0.963	0.137	-0.138	
1.660	0.138	-0.139	
18.90	0.142	-0.140	
49.60	0.149	-0.142	
99.43	0.157	-0.144	
135.0	0.163	-0.145	
238.1	0.178	-0.148	
311.8	0.188	-0.151	
405.6	0.200	-0.153	
525.1	0.215	-0.156	
677.5	0.234	-0.160	
871.6	0.257	-0.164	
1119	0.287	-0.170	
1434	0.325	-0.176	
1836	0.373	-0.183	
2348	0.438	-0.192	
3000	0.543	-0.202	
3120	0.572	-0.204	
3208	0.598	-0.205	
3353	39.087	-0.207	

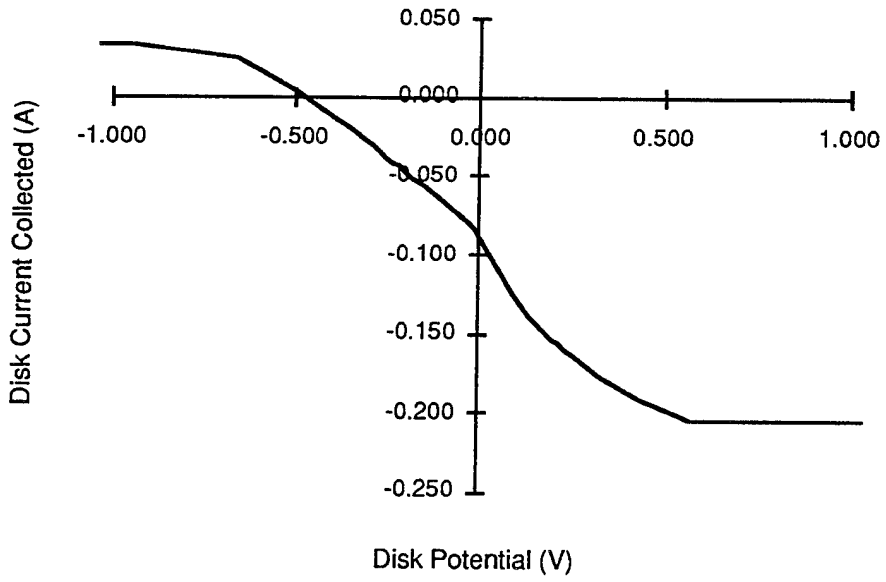

Figure 40. Disk current as a function of center potential after change.

13. SECONDARY ELECTRON YIELDS

We were presented with data for the secondary yield of Ar^+ on 304SS (the stainless steel material of which the CHAWS probe outer shell is constructed). This note describes the procedure by which this data was generalized for calculation of the secondary-enhanced total current to the CHAWS probe.

Conversion to Standard Form

The data provided was well-fit by

$$\gamma = 0.2\ E$$

where E is the Argon ion energy [keV]. However, it is customary to fit ion-generated secondary electron yield data in this regime by

$$\gamma = c_0 + c_1\ (v - v_0)$$

where v is the ion velocity and $c_0 + c_1$, and v_0 are constants to be determined. (For $v < v_0$, the yield is set to c_0, the "Auger yield." The velocity-dependent portion of γ is called the "kinetic yield.") The low-energy data points were read off the supplied plot. The data was reasonably fit using the constants

$$c_0 = 0.18$$
$$c_1 = 1.0 \times 10_{-5}\ s\ m^{-1}$$
$$v_0 = 7.2 \times 10^4\ m\ s^{-1}$$

Figure 41 shows the low energy data points, the linear-in-energy fit, and the linear-in-velocity fit.

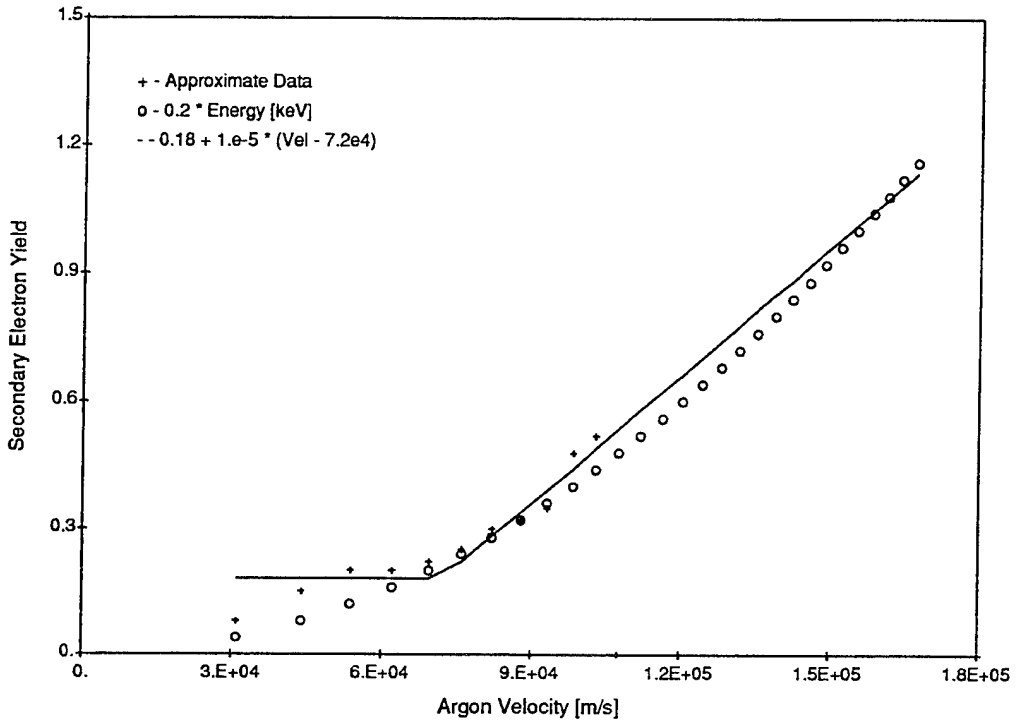

Figure 41. Secondary yield measurements compared with linear in energy and linear in velocity fits.

Generalization to Different Species

For lack of better information, the constants c_0 and v_0 are assumed to be species independent. However, c_1 was taken to follow the atomic number dependence suggested by Yarlagadda et al. [Phys. Rev. B17, 3473 (1978)] as cited in Alonso *et al.*, [Phys. Rev B22, 80 (1980)]:

$$c_1 \propto Z^2 \left[1 - \exp\left(-0.95 Z^{-2/3}\right)\right]^2$$

where Z is the ion projectile atomic number. For the primary species of interest, the constants in the secondary yield formula are given by Table 9.

Table 9. Secondary yield formula constants.

Species	c_0	c_1	v_0
H^+	0.18	7.0×10^{-7}	7.2×10^4
O^+	0.18	5.3×10^{-6}	7.2×10^4
Ar^+	0,18	1.0×10^{-5}	7.2×10^4

The secondary yields for O^+ and H^+, as a function of energy, are shown in Figure 42.

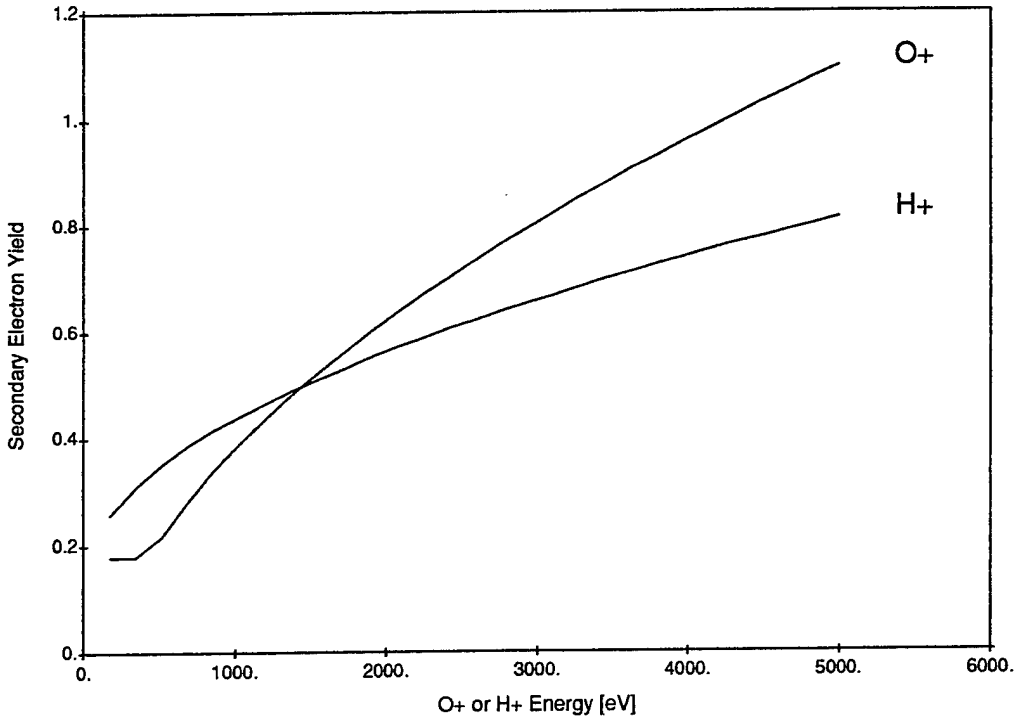

Figure 42. Secondary yield curves for H^+ and O^+.